

**Experimental and Modeling Studies of Two-Phase Flow in Porous
Media and Its Effects on the Performance of a PEM Fuel Cell**

Xuhai Wang

B.S. Chemical Engineering, Sichuan University, Chengdu, China, 2000

M.S. Chemical Technology, Institute of Process Engineering, Chinese Academy of
Sciences, Beijing, 2004

Submitted to the graduate degree program in Chemical & Petroleum Engineering and
the Graduate Faculty of the University of Kansas School of Engineering in partial
fulfillment of the requirements for the degree of Doctor of Philosophy.

Committee Members:

Chairman: Dr. Trung Van Nguyen

Dr. Jenn-Tai Liang

Dr. Aaron M. Scurto

Dr. Peter W. TenPas

Dr. Laurence Weatherley

Date of Defense: Jan. 26, 2010

The Dissertation Committee for Xuhai Wang certifies that this is the approval version
of the following dissertation:

**Experimental and Modeling Studies of Two-Phase Flow in Porous
Media and Its Effects on the Performance of a PEM Fuel Cell**

Committee Members:

Chairman: Dr. Trung V. Nguyen

Dr. Jenn-Tai Liang

Dr. Aaron M. Scurto

Dr. Peter W. TenPas

Dr. Laurence Weatherley

Date approved: Jan. 28, 2010

Abstract

An experimental investigation was conducted to study the two-phase flow properties of porous media used in proton exchange membrane (PEM) fuel cells. The liquid and gas phase relative permeability of porous media used in PEM fuel cells was measured at the University of Kansas and validated using the neutron imaging facility at the National Institute of Science and Technology (NIST). New correlations between the liquid saturation levels and relative permeability were identified. These correlations were further used to determine the liquid saturation levels in the electrodes of a PEM fuel cell during operation. The results showed that the 3rd-order power correlations between saturation levels and permeability developed for hydrophilic sands were unsuitable for the gas diffusion layers (GDLs) used in PEM fuel cells. The GDLs made of graphite fibers have different surface properties and structures than the well-sorted sands, causing a difference in the two-phase flow properties.

One-dimensional two-phase flow models were developed to study the effect of the porous media on the liquid saturation levels, liquid water management strategies, and fuel cell performance. To address the saturation level discontinuity created at the interface of two materials with different wetting properties, a saturation jump

condition was included in the models. This study showed that the hydrophobic part of the capillary curve was more important than the hydrophilic part because the zero capillary pressure ($p_c=0$) condition at the gas channel/GDL interface bound the liquid saturation levels in the hydrophobic region. The properties of the GDLs affected the fuel cell performances greatly when the reactant transport in the porous media was the limiting step. The model including a micro-porous layer (MPL) in the cathode side showed that the zero-net-water-transport-across-the-membrane was achievable, which would eliminate the anode humidification requirement and improve the fuel cell performance. Hydrophobic catalyst layers (CLs) in the cathode and anode were required to prevent the CLs from being flooded, when the hydrophobic MPL was presented in the cathode side. The complete model consisting of both the cathode and anode showed that the liquid water transport rate from the cathode to the anode was higher when there was no MPL in the anode side. The complete model also showed that when the anode was treated as an interface instead of a complete porous electrode, over-prediction of the fuel cell voltage resulted, mainly from the omission of the ohmic losses in the anode.

Acknowledgements

I would like to express my sincere gratitude to my advisor, Dr. Trung Van Nguyen, who introduced me to this fascinating and rewarding field of study. Dr. Nguyen continuously supported and directed my research and study. He was always available to give me guidance and assistance, even during his two-year service to the National Science Foundation (NSF) in Washington, DC. His mentorship and insight will continue to inspire me both personally and professionally.

I would also like to thank my committee members, Dr. Jenn-Tai Liang, Dr. Aaron M. Scurto, Dr. Peter W. TenPas, and Dr. Laurence Weatherley, for their valuable time, helpful advice and critical review of my dissertation. Thanks also go to Dr. Kyle V. Camarda and Dr. Javier Guzman for serving on my comprehensive exam committee.

My colleagues, Heebong Ohn, Roland Friedmann and Yan Gao, also deserve thanks for their frequent assistance with this experiment. Thanks go to Dr. Qiang Ye for his helpful discussion of fuel cell modeling. I also thank Will Musgrove and Andrea Senf for proofreading my manuscript.

I would like to acknowledge the staff of the Chemical & Petroleum Engineering Department for their services. I thank TVN Systems, Inc. for generously providing

me with an internship and also for supplying fuel cell electrodes, gaskets and other materials for my study. I thank the National Institute of Standards and Technology (NIST) for providing the neutron imaging facility.

And finally, none of this could have been accomplished without the unconditional support of my family over the past years. My special thanks go to my wife, Jing Fang, for her support and patience during my study at KU and to my daughter, Ashley T. Wang, who brings so much happiness to my life.

Table of Contents

| | |
|-------------------------------------------------|------------|
| Title Page..... | I |
| Acceptance Page..... | II |
| Abstract..... | III |
| Acknowledgements..... | V |
| Table of Contents..... | VII |
| List of Figures..... | XII |
| List of Tables..... | XIX |
| List of Symbols..... | XXI |
| | |
| Chapter 1 Introduction..... | 1 |
| 1.1 Fuel Cell Benefits..... | 1 |
| 1.2 Fuel Cell Types..... | 3 |
| 1.3 PEM Fuel Cell Components and Transport..... | 7 |
| 1.4 PEM Fuel Cell Thermodynamics..... | 13 |
| 1.5 PEM Fuel Cell Performance..... | 16 |
| 1.6 Motivation and Objectives..... | 18 |
| 1.7 References..... | 22 |

| | |
|--------------------------------------------------------------------------------------------------------------------------------|-----------|
| Chapter 2 Experimental Study of Relative Permeability of Porous Media Used in PEM Fuel Cells..... | 25 |
| 2.1 Introduction..... | 25 |
| 2.2 Experimental..... | 28 |
| 2.2.1 Materials..... | 28 |
| 2.2.2 Gas Permeability..... | 29 |
| 2.2.3 Liquid Permeability..... | 34 |
| 2.3 Results and Discussion..... | 36 |
| 2.3.1 Gas Relative Permeability..... | 36 |
| 2.3.2 Liquid Relative Permeability..... | 43 |
| 2.4 Conclusions..... | 49 |
| 2.5 References..... | 50 |
| Chapter 3 Experimental Evaluation of Saturation Levels in the Cathode side and Cell Performance of a PEM Fuel Cell..... | 54 |
| 3.1 Introduction..... | 54 |
| 3.2 Experimental..... | 57 |
| 3.2.1 Setup..... | 57 |
| 3.2.2 Procedure..... | 59 |
| 3.2.3 Materials..... | 61 |



| | |
|-------------------------------------------------------------------------------------------------------------------------------------------|-----------|
| 3.3 Results and Discussion..... | 62 |
| 3.3.1 Relative Permeability Correlations..... | 62 |
| 3.3.2 Base Case..... | 64 |
| 3.3.3 Stoichiometric Effect..... | 71 |
| 3.3.4 Temperature Effect..... | 74 |
| 3.4 Conclusions..... | 76 |
| 3.5 References..... | 77 |
| Chapter 4 Modeling the Effects of Capillary Property of Porous Media on the Performance of the Cathode of a PEM Fuel Cell..... | 82 |
| 4.1 Background..... | 82 |
| 4.2 Capillary Functions..... | 84 |
| 4.3 Model Development..... | 92 |
| 4.3.1 Assumptions..... | 93 |
| 4.3.2 Governing Equations..... | 94 |
| 4.3.3 Boundary Equations..... | 98 |
| 4.4 Results and Discussion..... | 104 |
| 4.5 Conclusions..... | 116 |
| 4.6 References..... | 117 |

| | |
|---------------------------------------------------------------------------------------------------------------------------------------------|------------|
| Chapter 5 Modeling the Effects of the Micro-Porous Layer on the Net Water Transport Rate Across the Membrane in a PEM Fuel Cell..... | 123 |
| 5.1 Introduction..... | 123 |
| 5.2 Model Development..... | 129 |
| 5.2.1 Modeled Domain..... | 129 |
| 5.2.2 Governing Equations..... | 130 |
| 5.2.3 Boundary Conditions..... | 133 |
| 5.2.4 Parameters and Correlations Used in the Simulation..... | 137 |
| 5.3 Results and Discussion..... | 138 |
| 5.3.1 With and Without MPL..... | 138 |
| 5.3.2 Capillary Effect of the MPL..... | 148 |
| 5.3.3 Preferred Combination of the GDL, MPL and CL..... | 154 |
| 5.4 Conclusions..... | 161 |
| 5.5 References..... | 162 |
| Chapter 6 A Modeling Study of the Effects of Anode Porous Layer on the Performance of a PEM Fuel Cell..... | 168 |
| 6.1 Introduction..... | 168 |
| 6.2 Model Development..... | 169 |
| 6.2.1 Modeled Domain..... | 169 |

| | |
|-------------------------------------------------------|------------|
| 6.2.2 Governing Equations..... | 169 |
| 6.2.3 Boundary Conditions..... | 171 |
| 6.2.4 Capillary Curves..... | 173 |
| 6.2.5 Parameters Used in the Simulation..... | 175 |
| 6.3 Results and Discussion..... | 176 |
| 6.4 Conclusions..... | 183 |
| 6.5 References..... | 184 |
| Chapter 7 Conclusions and Recommendations..... | 186 |
| 7.1 Conclusions..... | 186 |
| 7.1.1 Experimental..... | 186 |
| 7.1.2 Modeling..... | 188 |
| 7.2 Recommendations..... | 190 |
| 7.2.1 Experimental..... | 190 |
| 7.2.2 Modeling..... | 192 |
| 7.3 Contributions to This Area..... | 193 |
| 7.3.1 Direct Contributions..... | 193 |
| 7.3.2 Indirect Contributions..... | 194 |
| 7.4 References..... | 195 |
| Appendix Experimental Data..... | 198 |

List of Figures

| | |
|------------------------------------------------------------------------------------------------------|----|
| Figure 1.1 Schematic of electrodes and charge flow of fuel cells..... | 4 |
| Figure 1.2 Schematic of components in a PEM fuel cell..... | 9 |
| Figure 1.3 Structure of Nafion..... | 12 |
| Figure 1.4 Polarization curve of a PEM fuel cell..... | 18 |
| Figure 2.1 Schematic of the relative permeability experiment..... | 32 |
| Figure 2.2 Neutron image (top view) of the relative permeability setup..... | 34 |
| Figure 2.3 Pressure drop and permeability of the material A1..... | 38 |
| Figure 2.4 Gas relative permeability of the material A1..... | 40 |
| Figure 2.5 Water displacement in a sample..... | 40 |
| Figure 2.6 Pressure drop and permeability of the material A3..... | 42 |
| Figure 2.7 Gas relative permeability of the material A3..... | 43 |
| Figure 2.8 Pressure drop and permeability of the material SGL 10CA..... | 45 |
| Figure 2.9 Liquid relative permeability of the material SGL 10CA..... | 46 |
| Figure 2.10 Pressure drop and permeability of the material Toray TGP-H-060 (30 %wt PTFE)..... | 47 |
| Figure 2.11 Liquid relative permeability of the material Toray TGP-H-060 (30 %wt PTFE)..... | 48 |
| Figure 3.1 Schematic of (a) a serpentine flow field, (b) an interdigitated flow field, (c) | |

| | |
|-----------------------------------------------------------------------------------------------------------------------------------------------------------------------------------------------------------------------------------------------------------------------------------------------------------------------------------------------------------------------------------------|----|
| a cross-sectional view of the serpentine flow field, and (d) a cross-sectional view of the interdigitated flow field.  represents gas flowing out of the surface, and  represents gas flowing into the surface..... | 58 |
| Figure 3.2 Correlation between saturation level and permeability..... | 64 |
| Figure 3.3 Voltage, current density, and pressure drop in the test of sample B1. Stoichiometry of A/C=2/4, temperature of $T_{\text{cell}}/T_A/T_C=70/70/70$ °C. A and C represent anode and cathode, respectively..... | 66 |
| Figure 3.4 Fuel cell performance, pressure drop, and saturation level of material B1. Stoichiometry of A/C=2/4, temperature of $T_{\text{cell}}/T_A/T_C=70/70/70$ °C..... | 68 |
| Figure 3.5 Voltage, current density, and pressure drop in the test of sample B3. Stoichiometry of A/C=2/4, temperature of $T_{\text{cell}}/T_A/T_C=70/70/70$ °C..... | 69 |
| Figure 3.6 Fuel cell performance, pressure drop, and saturation level of material B3. Stoichiometry of A/C=2/4, temperature of $T_{\text{cell}}/T_A/T_C=70/70/70$ °C..... | 71 |
| Figure 3.7 Voltage, current density, and pressure drop in the test of sample B1. Stoichiometry of A/C=2/1.5, temperature of $T_{\text{cell}}/T_A/T_C=70/70/70$ °C... | 73 |
| Figure 3.8 Fuel cell performance, pressure drop, and saturation level of material B1. | |

| | |
|----------------------------------------------------------------------------------------------------------------------------------------------------------------------------------|-----|
| Stoichiometry of $A/C=2/1.5$, temperature of $T_{\text{cell}}/T_A/T_C=70/70/70$ °C..... | 74 |
| Figure 3.9 Voltage, current density, and pressure drop in the test of sample B1. | |
| Stoichiometry of $A/C=2/1.5$, temperature of $T_{\text{cell}}/T_A/T_C=70/50/50$ °C... | 75 |
| Figure 3.10 Fuel cell performance, pressure drop, and saturation level of material B1. | |
| Stoichiometry of $A/C=2/1.5$, temperature of $T_{\text{cell}}/T_A/T_C=70/50/50$ °C..... | 76 |
| Figure 4.1 Comparison of capillary pressure of materials with different capillary properties..... | 85 |
| Figure 4.2 Liquid saturation level jump condition at two materials with different wetting properties (by Clint D. Frye, an undergraduate student in our group)..... | 86 |
| Figure 4.3 Experimentally determined capillary pressure of a GDL (Toray 060) and a fitted capillary curve of a CL..... | 88 |
| Figure 4.4 Adjusted capillary functions of CL..... | 89 |
| Figure 4.5 Adjusted capillary functions of GDL..... | 91 |
| Figure 4.6 Schematic diagram of the modeled domain..... | 93 |
| Figure 4.7 Saturation level in GDL and CL for the base case with G1 and C1 at various cell voltages (refer to Fig. 4.3 and Table 4.1)..... | 105 |

| | |
|-------------------------------------------------------------------------------------------------------------------------------------------------------------------------------------------------------------------------------------------------------------------------------------------------------|-----|
| Figure 4.8 The effect of the CL capillary functions on the saturation levels in the GDL and CL at 0.6V (refer to Fig. 4.4 and Table 4.1)..... | 106 |
| Figure 4.9 Capillary diffusion coefficients for different CL capillary functions (refer to Fig. 4.4 and Table 4.1)..... | 109 |
| Figure 4.10 The effects of the CL capillary pressure functions on the fuel cell performance (refer to Fig. 4.4 and Table 4.1)..... | 110 |
| Figure 4.11 The effect of the GDL capillary functions on the saturation levels in the GDL and CL at 0.6V (refer to Fig. 4.5 and Table 4.1)..... | 111 |
| Figure 4.12 Capillary diffusion coefficients for different GDL capillary functions (refer to Fig. 4.5 and Table 4.1)..... | 112 |
| Figure 4.13 The effects of the GDL capillary pressure functions on the fuel cell performance (refer to Fig. 4.5 and Table 4.1)..... | 113 |
| Figure 5.1 SEM picture of an MPL..... | 126 |
| Figure 5.2 Schematic diagram of the modeled domain..... | 129 |
| Figure 5.3 Capillary curves used in the case with and without the MPL. The fitting parameters of a_1 , a_2 , b , c , and d are -22.7, -16.2, -644.9, 0.58, -7.6 for G1, -30.0, -7.0, -9878.4, 0.3, -4000.0 for M1, and -45.0, -8.0, 5000.0, 0.78, -1106.56 for C1, respectively..... | 139 |
| Figure 5.4 (a) Liquid water saturation level, and (b) liquid pressure at 0.6V. G1, M1, | |

| | |
|-----------------------------------------------------------------------------------------------------------------------------------------------------------------------------------------------------------------------------------------------------------------------------------------------------------------------------|-----|
| and C1 were used in the case with the MPL; G1 and C1 were used in the case without the MPL (Refer to Fig. 5.3)..... | 141 |
| Figure 5.5 (a) Net liquid water fluxes, (b) liquid water fluxes of each component for the case without MPL, and (c) liquid water fluxes of each component for the case with MPL at 0.6V. G1, M1, and C1 were used in the case with the MPL; G1 and C1 were used in the case without the MPL (Refer to Fig. 5.3)..... | 144 |
| Figure 5.6 Water fluxes in the simulated domain at 0.6V. G1, M1, and C1 were used in the case with the MPL; G1 and C1 were used in the case without the MPL (Refer to Fig. 5.3)..... | 145 |
| Figure 5.7 Fuel cell performance. G1, M1, and C1 were used in the case with the MPL; G1 and C1 were used in the case without the MPL (Refer to Fig. 5.3)..... | 147 |
| Figure 5.8 Capillary curves used in the study of MPL capillary effect. The fitting parameters of a_1 , a_2 , b , c , and d are -30.0, -16.0, -9878.4, 0.1, -4000.0 for M2, -13.0, -10.5, -2000.0, 0.4, -500.0 for M3, respectively. G1, M1, and C1 are the same as those in Fig. 5.3..... | 149 |
| Figure 5.9 MPL capillary effects on (a) the liquid water saturation level, (b) liquid pressure, and (c) liquid water flux at 0.6V (Refer to Fig. | |

| | |
|---------------------------------------------------------------------------------------------------------------------------------------------------------------------------------------------------------------------------------------|-----|
| 5.8)..... | 152 |
| Figure 5.10 MPL capillary effects on the water fluxes at 0.6V. Capillary curves of the GDL and CL were fixed to be G1 and C1, respectively (Refer to Fig. 5.8)..... | 153 |
| Figure 5.11 MPL capillary effects on the fuel cell performances (Refer to Fig. 5.8)..... | 154 |
| Figure 5.12 Capillary curves used in the preferred combinations. The fitting parameters of a1, a2, b, c, and d are -22.7, -10.0, -10000.0, 0.3, -2000.0, respectively, for G2. G1, M2, and C1 are the same as in Fig. 5.8..... | 156 |
| Figure 5.13 (a) Liquid water saturation levels, (b) liquid pressure, and (c) liquid water fluxes at 0.6V (Refer to Fig. 5.12)..... | 159 |
| Figure 5.14 GDL effects on the fuel cell performances (Refer to Fig. 5.12)..... | 160 |
| Figure 6.1 Schematic diagram of the modeled domain..... | 169 |
| Figure 6.2 Capillary curves used in the model..... | 174 |
| Figure 6.3 Water needed to saturate a dry anode at 60 °C..... | 177 |
| Figure 6.4 Distribution of (a) saturation levels, and (b) liquid water pressure in the modeled domain at 0.6 V..... | 179 |
| Figure 6.5 Liquid water flux in the modeled domain at 0.6 V..... | 180 |
| Figure 6.6 Effects of anode MPL on fuel cell performance..... | 182 |

| | |
|--------------------------------------------------------------|-----|
| Figure 6.7 Ionic potential in the modeled domain..... | 183 |
|--------------------------------------------------------------|-----|

List of Tables

| | |
|-----------------------------------------------------------------------------------------------------------------|-----|
| Table 1.1 Different types of fuel cells..... | 7 |
| Table 1.2 ΔG_f , open circuit potential, and thermodynamic efficiency for PEM fuel cells..... | 16 |
| Table 2.1 Properties of GDLs used in the experiment..... | 29 |
| Table 2.2 Experimental conditions..... | 36 |
| Table 3.1 Fuel cell operation conditions..... | 61 |
| Table 3.2 Properties of gas transport media used in the experiment..... | 62 |
| Table 4.1 Parameters of the capillary functions..... | 92 |
| Table 4.2 Governing equations..... | 94 |
| Table 4.3 Boundary conditions..... | 99 |
| Table 4.4 Correlations used in the model..... | 102 |
| Table 4.5 Parameters used in the model..... | 103 |
| Table 4.6 Simulation conditions..... | 104 |
| Table 4.7 Summary of the capillary effects..... | 115 |
| Table 5.1 Governing equations..... | 132 |
| Table 5.2 Boundary conditions..... | 136 |
| Table 5.3 Parameters..... | 137 |
| Table 5.4 Simulation conditions..... | 138 |

| | |
|--------------------------------------------------------|-----|
| Table 6.1 Governing equations of the anode..... | 170 |
| Table 6.2 Boundary conditions..... | 173 |
| Table 6.3 Capillary functions..... | 174 |
| Table 6.4 Parameters..... | 175 |
| Table 6.5 Operation conditions..... | 176 |
| Table A.1 Experimental data for Fig. 2.4..... | 198 |
| Table A.2 Experimental data for Fig. 2.7..... | 199 |
| Table A.3 Experimental data for Fig. 2.9..... | 201 |
| Table A.4 Experimental data for Fig. 2.11..... | 202 |
| Table A.5 Experimental data for Fig. 3.4..... | 203 |
| Table A.6 Experimental data for Fig. 3.6..... | 204 |
| Table A.7 Experimental data for Fig. 3.8..... | 205 |
| Table A.8 Experimental data for Fig. 3.10..... | 206 |

List of Symbols

| | |
|------|----------------------------------------------------|
| a | specific area (cm^2/cm^3) |
| AFC | alkaline fuel cell |
| BSL | base support layer |
| C | concentration (mole/cm^3) |
| CL | catalyst layer |
| D | diffusion coefficient (cm^2/s) |
| F | Faraday constant (coulomb/mole) |
| GDL | gas diffusion layer |
| H | Henry's constant ($\text{atm cm}^3/\text{mole}$) |
| HOR | hydrogen oxidation reaction |
| i | current density (A/cm^2) |
| k | conductivity ($1/(\Omega \cdot \text{cm})$) |
| K | permeability (cm^2) |
| m | Catalyst loading |
| M | molecular weight (g/mole) |
| MCFC | molten carbonate fuel cell |
| MEA | membrane electrode assembly |

| | |
|-----------|------------------------------------------------------------|
| MPL | micro-porous layer |
| n | electro-osmotic drag coefficient |
| N | flux (mole/(s · cm ²)) |
| OCV | open circuit voltage |
| ORR | oxygen reduction reaction |
| p | pressure (Pa) |
| PAFC | phosphoric acid fuel cell |
| PEM | proton exchange membrane |
| PEMFC | proton exchange membrane fuel cell |
| PTFE | polytetrafluoroethylene |
| R_{O_2} | reaction rate (mole/(s · cm ³)) |
| R_w^c | Phase change reaction rate (mole/(s · cm ³)) |
| s | saturation level |
| SOFC | solid oxide fuel cell |
| T | temperature (K) |

Greek and Roman letters

| | |
|---------------|----------------|
| δ | thickness (cm) |
| ε | porosity |

| | |
|-----------|------------------------------|
| η | fuel cell maximum efficiency |
| λ | water content in Nafion |
| μ | viscosity (Pa · s) |
| ξ | effectiveness factor |
| ρ | density (g/cm ³) |
| φ | modulus |
| ϕ | ionic potential (V) |

Subscripts and Superscripts

| | |
|----------------|-------------------|
| agg | agglomerate |
| c | capillary |
| eff | effective |
| f | fixed charge site |
| g | gas phase |
| l | liquid |
| max | maximum |
| MEM | membrane |
| N | Nafion phase |
| O ₂ | oxygen |

| | |
|----|--------------|
| Pt | platinum |
| v | water vapor |
| w | liquid water |

Chapter 1

Introduction

1.1 Fuel Cell Benefits

Fuel cells are devices that convert chemical energy stored in fuels directly into electricity, providing several benefits over other technologies. First is efficiency: fuel cells provide two to three times more efficient usage of the fuel than that of a heat engine. Because of the high efficiency, greenhouse gas emissions will be reduced by 50% when hydrocarbon materials, such as methanol, monoxide, and natural gas, are used as fuels. When fuels from renewable energy sources are used, nearly zero greenhouse gas emission is achievable. Fuel cells are scalable; single fuel cells can be stacked together to meet the desired power output requirement. They are also durable and able to withstand various operating conditions (various temperatures, pressures and stoichiometries). Fuel cells are silent, greatly reducing noise pollution as well as air pollution. For fuel cells operated at high temperatures, the waste heat can be used to heat water or living spaces. Other benefits include high reliability, multi-fuel capability and ease of maintenance.¹

The efficiencies of heat engines are limited by the Carnot cycle. The highest efficiency of a heat engine is determined by the high temperature of the heat source

and the low temperature of the environment.

$$\eta_{\max} = \frac{T_1 - T_2}{T_1} \quad [1.1]$$

Eq. 1.1 is the efficiency of the Carnot cycle, where T_1 is the temperature of the heat source (K), and T_2 is the temperature of the environment (K). A car's engine only converts about 16% of the energy in gasoline to power used to turn the wheels, which is much lower than the Carnot efficiency.¹ Fuel cell vehicles have already proven much more efficient than similar internal combustion vehicles. Toyota has published their efficiency results, showing their conventional gasoline vehicle having a tank-to-wheel efficiency of only 16%, while their FCVH-4 running with hydrogen shows a 48% tank-to-wheel efficiency.¹

Fuel cells will increase the US energy security by reducing the reliance of the US on imported fossil fuels. Fuel prices will become more stable and international tensions will reduce with lesser competition for limited fossil fuel resources. The US is dependent on imported oil for almost two-thirds of its energy consumption. The transportation sector consumes about two-thirds of the total oil consumed in the US and accounts for over one-third of the total energy use. In 2006, the US imported about 13 million barrels of oil per day, which cost about 300 billion dollars a year.² The greater efficiency realized by fuel cells means that there is enormous promise for their application to the transportation sector. However, fuel cell vehicles are still

extremely expensive to produce because the materials and labor costs remain high. With those issues properly addressed, adoption of fuel cells in transportation will be more realistic in the near future. Fuel cell vehicles have been in operation in a few major cities (such as Vancouver, Canada, and Chicago, Illinois) for several years for demonstration purposes.³

1.2 Fuel Cell Types

There are five major types of fuel cells, each with a different type of electrolyte.⁴ Each type of fuel cell will be examined in detail below. Fig. 1.1 shows a schematic of the electrodes and charge flow in a fuel cell.

(1) Alkaline fuel cell (AFC)

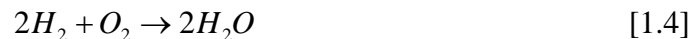
The reaction at the anode in an AFC is



The reaction at the cathode is



Combining Eqs. 1.2 and 1.3 gives the following net reaction



The electrons pass through an outer load from the anode to the cathode to generate the electricity. The hydroxide ions move in the electrolyte from the cathode to the anode, where they combine with hydrogen, releasing liquid water and electrons.

This reaction must be carried out in a base solution since the hydroxide ions in the electrolyte are required in the electrode reactions. Sodium hydroxide and potassium hydroxide solutions are often used in an AFC because of their low cost. An AFC was successfully used on the Apollo spacecrafts that took men to the moon. A similar AFC system is used to provide electrical power in the current space shuttle fleet.

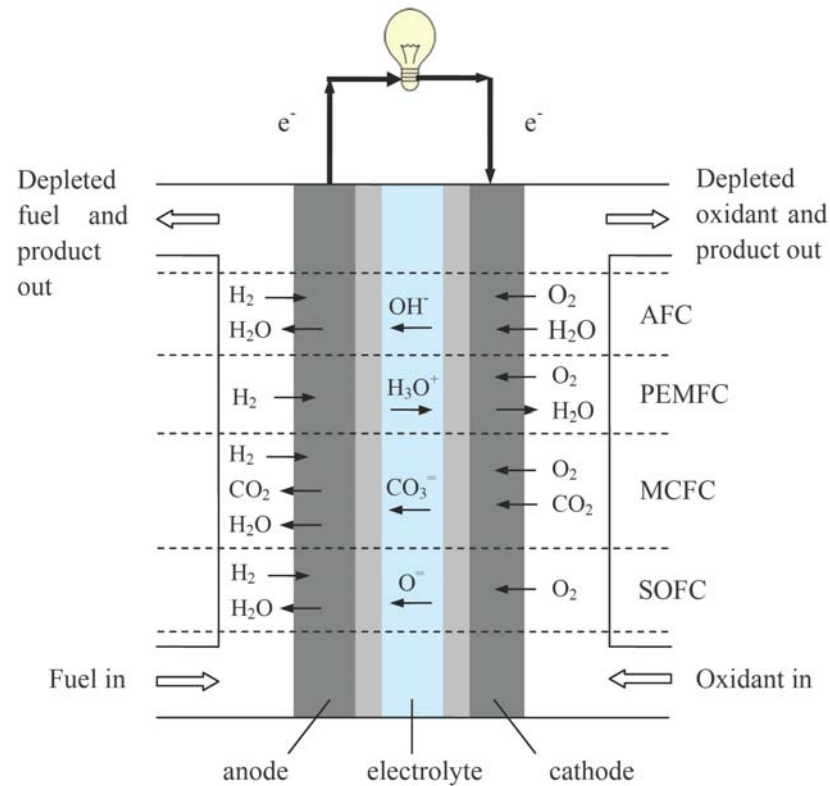
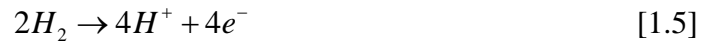


Figure 1.1 Schematic of electrodes and charge flow of fuel cells.

(2) Proton exchange membrane fuel cell (PEMFC)

Proton exchange membrane fuel cells are also known as polymer electrolyte fuel

cells. A solid ion conductive polymer is used as the electrolyte, which also acts as an electrical separator of the anode and cathode. A commonly used membrane material is Nafion from DuPont. The reaction at the anode is



The reaction at the cathode is



The net reaction is



The Nafion membrane allows only protons to transport through it, while the electrons must travel through the outer load to generate electricity. When Eqs. 1.4 and 1.7 are compared, one sees that the net reaction of the AFC and PEMFC is the same. Their main differences are the type of electrolytes used in the fuel cell and the electrochemical reactions at the anode and cathode.

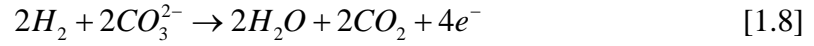
(3) Phosphoric acid fuel cell (PAFC)

Phosphoric acid (H_3PO_4) is used as the electrolyte for the transport medium of protons. The reactions in the anode and cathode are the same as those in Eqs. 1.5 and 1.6, respectively.

(4) Molten carbonate fuel cell (MCFC)

In an MCFC fuel cell, a molten mixture of alkaline metal carbonate is used as

the electrolyte. When hydrogen is supplied as a fuel, the reaction at the anode is



The reaction at the cathode is



The net reaction is



Eq. 1.10 shows that carbon dioxide is consumed at the cathode side and released at the anode side. The negatively charged ion, CO_3^{2-} , passes through the electrolyte from the cathode to the anode.

(5) Solid oxide fuel cell (SOFC)

Similar to the MCFCs, a negatively charged ion, O^- , passes through the electrolyte from the cathode to the anode in a SOFC. However, the two differ in the type of electrolyte used and the reactions occurring at the electrodes. Instead of a molten electrolyte as in the MCFC, the electrolyte in a SOFC is a solid. When hydrogen is supplied as a fuel, the reaction at the anode side is



The reaction at the cathode is



The net reaction is



Table 1.1 summarizes the different types of fuel cells. The differences between them include the form of the electrolyte, the range of the operating temperature, and the type of the catalyst. At high temperatures, a fast reaction rate can be achieved without the use of a noble catalyst. On the contrary, at low temperatures, as in a PEMFC and PAFC, a noble catalyst like platinum is required to achieve fast reaction rates.

Table 1.1 Different types of fuel cells.^{5,6}

| Fuel cell type | Electrolyte (mobile ion) | Operating temperature, °C | Catalyst Anode/Cathode |
|----------------------------------------|------------------------------------------------------------------------------|------------------------------|-------------------------------|
| Alkaline (AFC) | KOH (OH ⁻) | 50 - 200 | Pt/Pt or Ni/NiO |
| Proton exchange membrane (PEMFC) | Nafion (H ⁺) | < 100 | Pt/Pt or Pt-Ru/Pt |
| Phosphoric acid (PAFC) | Phosphoric acid (H ⁺) | ~ 200 | Pt/Pt |
| Molten carbonate (MCFC) | Li-K or Li-Na carbonate (CO ₃ ²⁻) | ~ 650 | Ni-Cr/Lithiated NiO |
| Solid oxide (SOFC) | YSZ (ZrO ₂ -Y ₂ O ₃) (O ²⁻) | 500 - 1000 | Ni-YSZ/LaMnO ₃ -Sr |

1.3 PEM Fuel Cell Components and Transport

The proton exchange membrane (PEM) fuel cell is considered one of the most promising energy conversion devices for applications such as portable electronic

devices and automobiles in the near future. Fig. 1.2 shows the components in a PEM fuel cell. The cathode side includes a gas diffusion layer (GDL) and a catalyst layer (CL). The anode side has the same components as the cathode. The membrane made of Nafion separates the anode and cathode.

Flow Plate: The flow plate, usually made of carbon or graphite, provides the flow path for the reactants and serves as an electrical current collector. Carbon is superior to other metals as a current collector since metals are prone to corrosion, which can introduce metallic ion contaminants to the catalyst layers and membrane. However, the carbon plate is brittle and difficult to machine, which poses a challenge in its application.

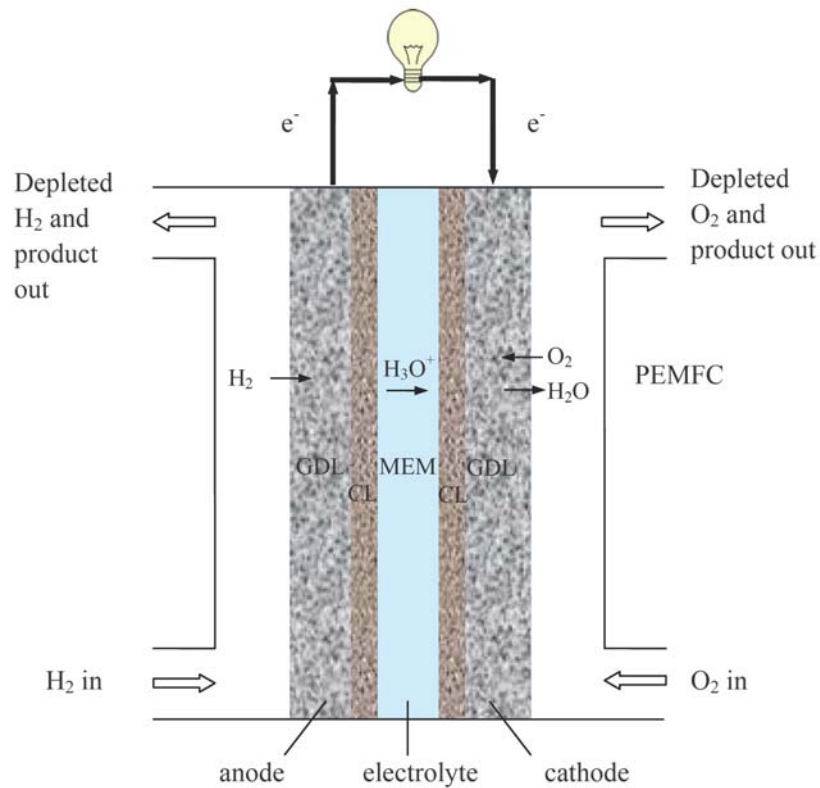


Figure 1.2 Schematic of components in a PEM fuel cell.

Gas Diffusion Layer: The GDL provides the transport path for the reactants and the electrons to and from the CL in the anode and cathode. There are two kinds of GDLs: carbon paper and carbon cloth. Carbon paper is commonly used in fuel cells because of its simple manufacturing process. Commercially available GDLs are primarily produced by SGL Group and Toray Industries, Inc. The GDLs from Toray have lower porosity and are denser than those from SGL Group.

At the cathode, oxygen diffuses from the flow channel through the GDL to the CL, where it reacts with protons and electrons from the anode to produce water. The

product of liquid water moves through the GDL to the channel to be carried away by the air flow stream in the flow channel. At the anode, hydrogen flows through the GDL to the CL, where it is oxidized to produce the electrons. The electrons produced in the anode flow through the anode GDL, outer load, and the cathode GDL to react in the cathode CL. Finally, in addition to providing transport paths to the reactants, products, and electrons, the GDL also provides mechanical support to the catalyst layer.

From the functions of the GDL, it is evident that the fuel cell performance can be improved by optimizing the properties of the GDL. The transport processes in the GDL must be considered systematically since they are inherently related. Although high porosity is preferred for reactant and product transport, its effects on electrical conductivity and mechanical strength should be taken into consideration.

In some cases, a bi-layer GDL is used to increase its hydrophobicity. To create a bi-layer GDL, a micro-porous layer (MPL) is applied onto one side of the macro porous gas diffusion layer using a paste consisting of carbon and a hydrophobic phase, such as polytetrafluoroethylene (PTFE), to increase its hydrophobicity. Details of how to make an MPL can be found in reference 7. The dense MPL works like a water barrier layer, preventing the liquid water generated at the cathode catalyst layer from flowing out of the cathode CL. As a result, the effect of flooding in the cathode is

alleviated. The functions of MPL will be discussed in further detail in Chapter 5.

Catalyst Layer: The catalyst layer is the power generating component of a PEM fuel cell. As seen in Eqs. 1.5, 1.6, and 1.7, protons and electrons are generated in the anode and consumed in the cathode. The electrons generated in the anode move through the anode CL, GDL, and outer load to the cathode GDL and CL. The protons generated in the anode move through the Nafion membrane to the cathode CL. Thus, the CL is a three-phase transport and reaction region, which includes the gas phase, liquid phase, and solid phase (for electrons and protons). The porous structure of the CL provides the transport path for the gas and liquid. In some cases, the void volume of a CL shows both hydrophobic and hydrophilic characteristics when a hydrophobic phase, such as PTFE, is added. The liquid phase will move through the hydrophilic path, and the gas phase will move through the hydrophobic path. The carbon and platinum provide the transport path for the electrons. A proton conductive phase, Nafion, is added to the CL to provide the transport path for the protons. Thus, it is essential to optimize the three phases (gas, liquid and solid) by adjusting the ratio of the carbon supported catalyst/Pt, Nafion and PTFE to achieve the optimal fuel cell performance.⁸

Membrane: The anode and the cathode are connected by a Nafion membrane, which has the following structure:

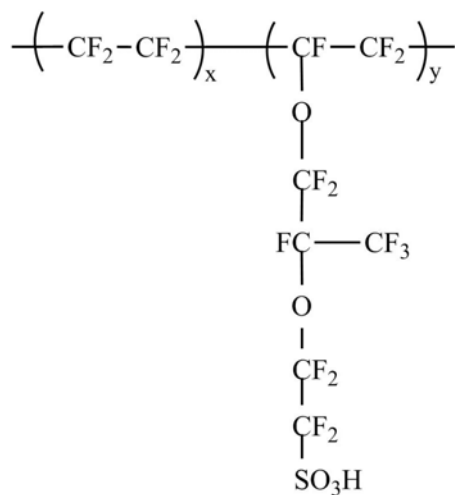


Figure 1.3 Structure of Nafion.

Protons are transferred along the $-\text{SO}_3\text{H}$ group, which is formed of SO_3^- ion and H^+ ion. Nafion membranes are denoted with a letter N followed by a several digit number based on the molecular weight of the polymer and the thickness of the membrane. The first 2 digits represent the molecular weight divided by 100. The last one or two digits indicate the membrane thickness in the unit of mills (1 mill=1/1000 inch=0.0254 mm).⁴ For example, Nafion N112 has the equivalent molecular weight of 1100 and thickness of 2 mills (0.0508 mm).

The backbone of Nafion ($-\text{CF}_2-\text{CF}_2-$) is hydrophobic. However, the ionic group, $-\text{SO}_3\text{H}$, is hydrophilic, which attracts liquid water. The weight of dry Nafion can increase by as much as 50%wt when fully hydrated.⁵ The conductivity of dry Nafion

is very low and increases with the amount of water absorbed.⁹ Thus, saturated gas reactants are often used in a PEM fuel cell to keep the membrane hydrated and to provide high ionic conductivity. This requirement raises another issue of water management strategies in the PEM fuel cells: the flooded cathode and dry anode.

1.4 PEM Fuel Cell Thermodynamics

For the reaction in a PEM fuel cell



the maximum energy available to do the external work is defined as the Gibbs free energy. The Gibbs free energy of the reaction is defined by the following equation

$$\Delta G_f^0 = G_{f,H_2O}^0 - \left(G_{f,H_2}^0 + \frac{1}{2} G_{f,O_2}^0 \right) \quad [1.15]$$

where ΔG_f^0 is the change of Gibbs free energy at the standard state (25°C, 1 atm partial pressure, 1 molal (1 mole/kg solvent)). Eq. 15 can be simplified further because G_{f,H_2}^0 and G_{f,O_2}^0 are zero.

$$\Delta G_f^0 = G_{f,H_2O}^0 \quad [1.16]$$

The charge involved in the reaction is

$$Charge = -2N \cdot e = -2F \text{ coulombs} \quad [1.17]$$

where N is the Avogadro number, $N = 6.022 \times 10^{23} / \text{mole}$; e is the charge on one electron, $e = 1.602 \times 10^{-19} \text{ coulombs}$; F is Faraday constant, $F = 96485 \text{ coulombs}$.

From Fig. 1.2, the electrical work consists of moving -2F charge from the anode

to the cathode, which can be calculated by

$$\text{Electrical work} = -2F \cdot E^0 \quad \text{joules} \quad [1.18]$$

where E^0 is the reversible open circuit voltage at standard state. The reversible open circuit voltage of the PEM fuel cell can be derived from Eqs. 1.16 and 1.18.

$$\Delta G_f^0 = -2F \cdot E^0 \quad [1.19]$$

Thus,

$$E^0 = -\frac{\Delta G_f^0}{2F} \quad [1.20]$$

ΔG_f^0 is a function of temperature and the state of the reactants and product. The activities of the reactant and the product affect the Gibbs free energy of the electrochemical reaction in the PEM fuel cell. From the thermodynamics arguments for a constant temperature, the Gibbs free energy of the Eq. 1.14 is expressed as

$$\Delta G_f = \Delta G_f^0 - RT \ln \left(\frac{a_{H_2} \cdot a_{O_2}^{\frac{1}{2}}}{a_{H_2O}} \right) \quad [1.21]$$

where ΔG_f^0 is the change of Gibbs free energy at the standard state; R is the ideal gas law constant (8.314 J/(mole·K)); T is the temperature (K); a_{H_2} , a_{O_2} , and a_{H_2O} are the activities of hydrogen, oxygen, and water, respectively.

Substitute Eq. 1.19 into Eq. 1.21, we have

$$-2F \cdot E = \Delta G_f^0 - RT \ln \left(\frac{a_{H_2} \cdot a_{O_2}^{\frac{1}{2}}}{a_{H_2O}} \right) \quad [1.22]$$

By rearranging Eq. 1.22, we obtain the following equation

$$\begin{aligned}
 E &= -\frac{\Delta G_f^0}{2F} + \frac{RT}{2F} \ln \left(\frac{a_{H_2} \cdot a_{O_2}^{\frac{1}{2}}}{a_{H_2O}} \right) \\
 &= E^0 + \frac{RT}{2F} \ln \left(\frac{a_{H_2} \cdot a_{O_2}^{\frac{1}{2}}}{a_{H_2O}} \right)
 \end{aligned} \tag{1.23}$$

where E^0 is the fuel cell potential at the standard state. Eq. 1.23 is called Nernst equation, which describes the effect of the activities of the reactants and product on the fuel cell potential. Note that this equation cannot be used to calculate the temperature dependence of the thermodynamic potential. Only the effect of the activities of the reactants and the products can be predicted by Eq. 1.23.

Fuel cell efficiency is defined as the ratio of electrical energy to the heat that would be produced by burning the fuel. The maximum electrical energy available is equal to the reversible energy that the fuel can supply, which is the Gibbs free energy, so

$$\eta_{\max} = \frac{\Delta G_f}{\Delta H_f} \times 100\% \tag{1.24}$$

η_{\max} in Eq. 1.24 is also called the thermodynamic efficiency. However, values of ΔH_f change with the state of the water in the electrochemical reaction. When water is in the form of gas and liquid state

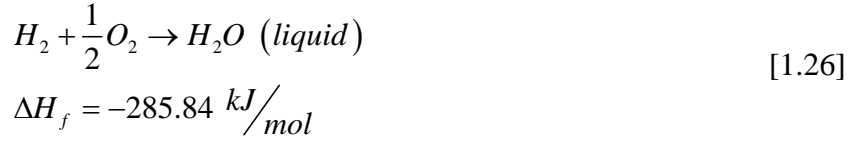
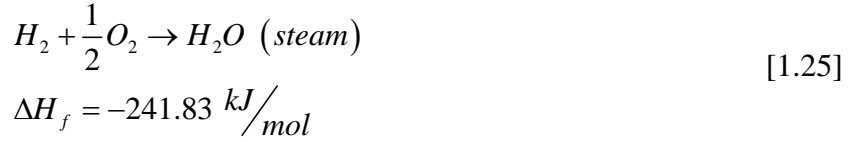


Table 1.2 summarizes the ΔG_f , open circuit voltage (OCV), and thermodynamic efficiency based on the liquid state of the water product.

Table 1.2 ΔG_f , open circuit potential, and thermodynamic efficiency for PEM fuel cells.⁵

| Form of water product | Temperature, °C | ΔG_f , kJ/mol | OCV, V | Thermodynamic efficiency, % |
|-----------------------|-----------------|-----------------------|--------|-----------------------------|
| Liquid | 25 | -237.2 | 1.23 | 83 |
| Liquid | 80 | -228.2 | 1.18 | 80 |
| Gas | 100 | -225.2 | 1.17 | 79 |

1.5 PEM Fuel Cell Performance

Fig. 1.4 shows a typical polarization curve of a PEM fuel cell. The Nafion membrane is designed to be nonconductive of electrons and impermeable to gases. However, a very small amount of hydrogen can penetrate the membrane from the anode to the cathode to react with oxygen directly. This amount of hydrogen reactant is wasted without doing external work, leading to OCV loss.

The activation loss is caused by the slow electrochemical reactions on the

surface of the electrodes. In a PEM fuel cell, the cathode oxygen reduction reaction (ORR) is the main source of activation loss. The kinetic loss can be reduced by raising the temperature, using more active catalysts, and increasing the active catalyst surface.

The ohmic loss is caused by the resistance of the transport of ions and electrons in the electrodes of the PEM fuel cell. The magnitude of ohmic drop is proportional to the current as expressed in the following equation

$$V = IR_{ohm} \quad [1.27]$$

where the V is the potential, I is the current, and R_{ohm} is the resistance.

The mass transport loss is caused by reactant depletion. In a PEM fuel cell, water flooding at the cathode side often causes the mass transport limitation by blocking the gas transport path of the reactants. If convective flow through the electrode could be created, it would reduce the mass transport loss by providing higher concentrations of the reactants and alleviating the flooding effect in the PEM fuel cell. Consequently, gas flow field design is also an important aspect in a PEM fuel cell.

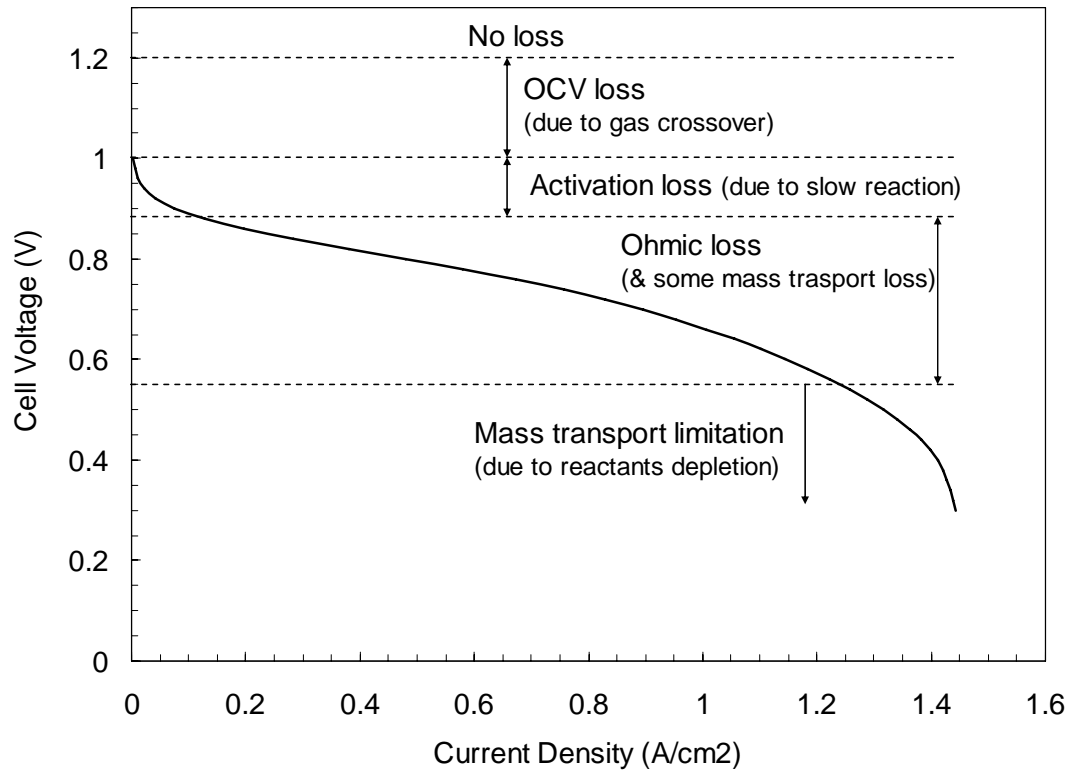


Figure 1.4 Polarization curve of a PEM fuel cell.

1.6 Motivation and Objectives

PEM fuel cells depend on proper water management to obtain high power density and energy efficiency. During operation, as a result of the electro-osmotic effect the membrane at the anode side tends to be dry. Consequently, to avoid anode dehydration, water is added to the anode gas stream in the form of water vapor to compensate for the amount lost to the cathode by electro-osmosis. Meanwhile, at the cathode the opposite problem occurs. Liquid water in the cathode of a PEM fuel cell is generated from three sources: 1) liquid water dragged by electro-osmosis from the

anode to the cathode, 2) oxygen reduction reaction, and 3) condensation when a temperature gradient exists. When the water generated at the cathode by these three processes is not properly removed, its accumulation leads to poor fuel cell performance by blocking the gas pores used for oxygen gas transport and forming an additional transport barrier over the reactive area.

When the operating temperature of a PEM fuel cell is below 100 °C, two-phase flow behavior of the gas phase and liquid phase has a significant impact on the PEM fuel cell performance since both liquid and gas phases exist simultaneously. First, in order to provide a transport path for the gaseous reactant, liquid water existing in the cathode side of a PEM fuel cell must be efficiently removed. Liquid water may form a thin liquid film on the catalyst layer acting as an additional barrier to the transport of the reactant gas to the catalyst active surface. Second, the membrane must be kept hydrated to decrease the ionic resistance. Water vapor saturated gases are often used to achieve this condition. Third, under certain circumstances the anode side could be flooded when excessive liquid water is transported from the cathode side to the anode side.

Two-phase flow properties of the porous media used in PEM fuel cells are important in fuel cell optimization and water management strategies. The permeability and capillary pressure curves reported in the literature vary greatly. The

absolute permeability varies between 10^{-11} m^2 to 10^{-13} m^2 .¹⁰⁻¹³ The 3rd-order power correlation of the relative permeability developed for well sorted sands was often used in modeling.¹⁴ The Leverett function developed for sands was used to simulate the capillary pressure of these porous media.¹⁵⁻¹⁹ However, the porous media used in PEM fuel cells have different surface properties and geometrical structures from sands, which leads to inaccurate predictions of the performance of PEM fuel cells.

Quantifying the liquid saturation level in the GDL will be helpful for validating two-phase flow models and determining the liquid water's role in affecting fuel cell performance. The conventional water management approach of adding water (gas/liquid phase) to the anode side and removing water from the cathode side is a self-defeating process. Water management can be made more efficient in a PEM fuel cell by engineering the material properties of the porous media used in the membrane electrode assembly (MEA) to force liquid water in the cathode back to the anode to achieve zero-net-water-transport-across-the-membrane.²⁰ If this could be achieved, it would minimize or eliminate the need for anode gas humidification. Modeling two-phase transport in the PEM fuel cells can provide the strategies to optimize fuel cell performance. Information extracted from the modeling will be useful in predicting and directing the experimental work.

Thus, the first objective of this research was to measure the two-phase transport

properties of the porous media used in PEM fuel cells. Experimental measurement of the permeability, developed at the University of Kansas lab and validated using neutron imaging facility at the National Institute of Science and Technology (NIST), is presented in Chapter 2. Chapter 3 describes the experimental measurement of the liquid water saturation levels in the cathode side. The pressure drop in the interdigitated flow field indicates the liquid water content in the GDL. This pressure drop was recorded in the experiment to calculate the relative permeability. The liquid water saturation level was calculated from a correlation between the permeability and the saturation levels. In Chapter 4 the capillary pressure effect of the GDL and CL on the fuel cell performance is simulated by a two-phase flow model. The effect of the position, shape, and slope of the capillary curves on the liquid water saturation level and the fuel cell performance was investigated. Chapter 5 focuses on the effect of the MPL on the water management strategies to achieve the goal of zero-net-water-transport-across-the-membrane. And finally, a model including both the anode and cathode is presented in Chapter 6. The operating conditions and properties of the anode side were investigated to elucidate the role of the anode side in a PEM fuel cell.

1.7 References

1. www.fuelcells.org. In 2009.
2. J. Yanes and R. Grosse, US Oil Import Dependence: Which Way out?, *Int. J. Energy Sect. Manage.*, 1 (2), 195, **2007**.
3. M. M. Mench, *Fuel cell engines*, John Wiley & Sons: Hoboken, N.J., p xi, 2008.
4. F. Barbir, *PEM Fuel Cells: Theory and Practice*, Elsevier Academic Press: Amsterdam ; Boston, p xv, 2005.
5. J. Larminie and A. Dicks, *Fuel Cell Systems Explained*, 2nd ed.; J. Wiley: Chichester, West Sussex, p xxii, 2003.
6. D. Natarajan, Experimental and Modeling Studies on the Spatiotemporal Current Density Distribution in a PEM Fuel Cell, Thesis (Ph.D.), University of Kansas, Chemical and Petroleum Engineering, 2004.
7. Z. Qi and A. Kaufman, Improvement of Water Management by a Microporous Sublayer for PEM Fuel Cells, *J. Power Sources*, 109 (1), 38, **2002**.
8. R. Friedmann and T. V. Nguyen, Optimization of the Cathode Catalyst Layer Composition Using a Novel 2-step Preparation Method, *ECS Trans.*, 16 (2), 2021, **2008**.
9. T. E. Springer, T. A. Zawodzinski and S. Gottesfeld, Polymer Electrolyte Fuel-Cell Model, *J. Electrochem. Soc.*, 138 (8), 2334, **1991**.

10. J. T. Gostick, M. W. Fowler, M. D. Pritzker, M. A. Ioannidis and L. M. Behra, In-Plane and Through-Plane Gas Permeability of Carbon Fiber Electrode Backing Layers, *J. Power Sources*, 162 (1), 228, **2006**.
11. V. Gurau, M. J. Bluemle, E. S. De Castro, Y.-M. Tsou, T. A. Zawodzinski Jr. and J. A. Mann Jr, Characterization of Transport Properties in Gas Diffusion Layers for Proton Exchange Membrane Fuel Cells 2. Absolute Permeability, *J. Power Sources*, 165 (2), 793, **2007**.
12. J. Ihonen, M. Mikkola and G. Lindbergh, Flooding of Gas Diffusion Backing in PEFCs - Physical and Electrochemical Characterization, *J. Electrochem. Soc.*, 151 (8), A1152, **2004**.
13. M. V. Williams, E. Begg, L. Bonville, H. R. Kunz and J. M. Fenton, Characterization of Gas Diffusion Layers for PEMFC, *J. Electrochem. Soc.*, 151 (8), A1173, **2004**.
14. M. Kaviany, *Principles of Heat Transfer in Porous Media*, 2nd ed.; Springer-Verlag: New York, p 708, 1995.
15. T. Berning and N. Djilali, A 3D, Multiphase, Multicomponent Model of the Cathode and Anode of a PEM Fuel Cell, *J. Electrochem. Soc.*, 150 (12), A1589, **2003**.
16. H. Meng and C. Y. Wang, Model of Two-Phase Flow and Flooding Dynamics in

- Polymer Electrolyte Fuel Cells, *J. Electrochem. Soc.*, 152 (9), A1733, **2005**.
17. U. Pasaogullari and C. Y. Wang, Liquid Water Transport in Gas Diffusion Layer of Polymer Electrolyte Fuel Cells, *J. Electrochem. Soc.*, 151 (3), A399, **2004**.
18. U. Pasaogullari and C. Y. Wang, Two-Phase Modeling and Flooding Prediction of Polymer Electrolyte Fuel Cells, *J. Electrochem. Soc.*, 152 (2), A380, **2005**.
19. Y. Wang, Porous-Media Flow Fields for Polymer Electrolyte Fuel Cells II. Analysis of Channel Two-Phase Flow, *J. Electrochem. Soc.*, 156 (10), B1134, **2009**.
20. T. V. Nguyen, Water Management by Material Design and Engineering for PEM Fuel Cells, *ECS Trans.*, 3 (1) (1), 1171, **2006**.

Chapter 2

Experimental Study of Relative Permeability of Porous Media Used in PEM Fuel Cells

2.1 Introduction

Both the liquid and gas phases exist in the porous media of PEM fuel cells because these devices usually operate at low temperatures. Water management strategies need to be well balanced to achieve optimal fuel cell performance. Two-phase flow properties of porous media used in PEM fuel cells are important in fuel cell optimization and water management strategies. On the one hand, to improve the transport of gaseous reactant and liquid water to and from the CL, the liquid water in the cathode side of a PEM fuel cell must be efficiently removed. Liquid water may also form a thin film on the active catalyst layer, blocking the active sites from accessing the electrochemical reaction. On the other hand, a water vapor saturated cathode and anode are preferred to provide high ionic membrane conductivity. Last, when a cathode with correct level hydrophobicity is used, sufficient water could be forced from the cathode back to the anode by permeation and diffusion to overcome the effect of electro-osmosis.¹ Hydrophobicity in the cathode can be created by adding a hydrophobic material, such as PTFE, to the GDL, MPL and CL to help

remove the liquid water from the cathode.^{2, 3} Better understanding of the transport properties of these porous media used in PEM fuel cells will lead to new strategies for water management. Of these transport properties, the gas and liquid permeability of the porous media used in PEM fuel cells are two of these important transport parameters.

In numerical simulations, the permeability in the form of linear correlation,⁴⁻⁶ polynomial correlation,^{7, 8} and function of multiple variables⁹ was used to describe the two-phase flow in porous media. These correlations of relative permeability of gas and liquid phases were functions of saturation levels that have not been validated by experimental data.

Experimentally measured gas absolute permeability of macro-porous media used in PEM fuel cells ranges from $4.4 \times 10^{-13} \text{ m}^2$ to $5.0 \times 10^{-11} \text{ m}^2$ depending on the porous media tested in the experiment.¹⁰⁻¹³ Since carbon fibers prefer to stay in a parallel direction, anisotropic properties are observed in the porous media used in PEM fuel cells. In-plane permeability is higher than through-plane permeability because of the geometrical layout of the carbon fibers. In a bi-layer GDL, a thin layer of dense MPL on the surface of the macro-porous substrate may cause a large decrease in the absolute permeability due to the small pores introduced by the MPL. PTFE content in the macro-porous substrate reduces the permeability by decreasing the pore sizes as

well as the surface morphology. However, Gurau *et al.*¹¹ showed that the permeability of the MPL increased with the PTFE content. Gurau *et al.* attributed this effect to the increased rigidity and intra-agglomerate pores of the MPL when the PTFE was added. Benziger *et al.*¹⁴ measured liquid permeability by flowing liquid water through a porous medium, using a liquid water column to control the liquid pressure. However, the saturation levels corresponding to the liquid permeability had to be determined separately, which introduced great uncertainties to the measurements. The ex-situ determined saturation levels might be different than the in-situ saturation levels in Benziger *et al.*'s experiment because liquid water might have drained from the tested sample when the liquid pressure applied to the GDL was removed.

In recent years, neutron imaging has been applied successfully to determine liquid water content in PEM fuel cells.¹⁵⁻¹⁹ With the improved resolution of neutron imaging, it is possible to map both in-plane and through-plane water distribution in an MEA and the flow fields of the cathode and anode. A better understanding of the liquid water distribution process inside the porous-media is valuable for better water management strategies in PEM fuel cells because the fuel cell performance is related to the liquid water saturation levels inside the electrodes of the fuel cell. Although neutron imaging has been used to measure the water content in a PEM fuel cell during operation, it had not been used for transport property measurement such as the

correlation between the gas and liquid phase permeability and liquid water saturation level.

This chapter focuses on the experimental study of the gas and liquid permeability of the porous media used in PEM fuel cells to determine the correlation between the gas and liquid permeability and liquid water saturation level. The gas permeability of two proprietary GDLs was measured by gravimetric analysis and neutron imaging. The liquid permeability of two commercially available GDLs was measured by neutron imaging. The obtained correlations were then used to determine the liquid water saturation levels in the cathode and anode GDLs during operation. This work will be discussed in Chapter 3. These correlations were also incorporated into fuel cell models to provide more accurate predictions of the water saturation levels in a PEM fuel cell.

2.2 Experimental

2.2.1 Materials

Four different kinds of GDLs were tested in this experiment. Two of them are proprietary GDLs that are not yet available on the market. The other two are commercially available GDLs from Toray Industries, Inc. and SGL Carbon Group. The properties of these four kinds of GDLs are summarized in Table 2.1. In this study, constant sample thickness was used by controlling the thickness of the metal washers

in the fixture. Homemade stainless steel washers were used to prevent the samples from being over-compressed. The uncompressed sample thickness was used in calculating the porosity and gas and liquid permeability.

Table 2.1 Properties of GDLs used in the experiment.

| Material Type | Thickness (μm) | Porosity | PTFE Content (%wt) |
|---------------------------------------|---------------------------------------------|-----------------|---------------------------|
| A1 (Proprietary GDL) | 216 | 0.81 | 0 |
| A3 (Proprietary GDL) | 325 | 0.85 | 5 |
| SGL-10CA (Carbon Group) | 380 | 0.85 | 10 |
| TGP-H-060 (Toray Industries, Inc.) | 190 | 0.78 | 30 |

2.2.2 Gas Permeability

A homemade fixture was used to measure the gas permeability of the GDLs listed in Table 2.1. A schematic view of the permeability measurement setup is shown in Fig. 2.1. To prevent water loss by evaporation, the gas used in the experiment was pre-saturated with water vapor by passing it through a bottle filled with de-ionized water. The temperature in the bubbler bottle was set 1~2 °C higher than the ambient temperature. Gas permeability measured by both the gravimetric analysis and neutron imaging was carried out in this experiment.

The pressure drop was measured by an electronic pressure transducer (26PC Series, Honeywell) and recorded by a data acquisition system (Personal Daq System

by Omega Engineering). The pressure transducer had an operating pressure range of ± 5 Psi.

Permeability by gravimetric analysis: The gravimetric analysis involved measuring the weight of the dry sample before the experiment and the weight of the wet sample after the experiment. The saturation level was calculated based on the difference between the wet and dry samples. The corresponding permeability was calculated from the pressure drop across the sample. In the gravimetric method, each experiment generated a datum point because the sample inside the fixture had to be removed from the fixture to be weighed in a balance. The gravimetric permeability measurement consisted of the following steps:

- 1) Weigh the dry GDL to be tested (the dry weight of the sample is denoted by m_1).
- 2) Pre-saturate a sample in de-ionized water at 80 °C for 1 hour followed by cooling down to ambient temperature. At 80 °C, the surface tension is sufficiently lowered to allow the sample, even when it is hydrophobic, to be saturated with liquid water. Once saturated, it was found that water would remain in the sample as it was cooled to ambient temperature.
- 3) Assemble the saturated sample in the fixture shown in Fig. 2.1.
- 4) Flow gas through the saturated sample and record the pressure drop, ΔP .

5) Disassemble the fixture at the end of the experiment and weigh the sample to obtain the wet weight, m_2 ;

6) Calculate the saturation level by

$$s = \frac{(m_2 - m_1) / \rho_{H_2O}}{\varepsilon V_{total}} \quad [2.1]$$

where ρ_{H_2O} is the liquid water density; ε is the porosity of the sample under compression; and V_{total} is the total volume of the sample under compression.

Gas permeability is calculated from Darcy's law.

$$\overline{k_g} = - \frac{v_g \mu_g}{\frac{\Delta P_g}{\Delta x_g}} \quad [2.2]$$

where v_g is the gas velocity; μ_g is the gas viscosity; $\overline{\Delta P_g}$ is the gas pressure drop; Δx_g is the gas traveling path length. The gas velocity is assumed to be constant because the pressure drop is low resulting from the small dimensions of the sample.

7) Repeat steps 1) to 6) with a different flow rate to obtain the permeability at a different saturation level.

Once the saturation level and permeability were calculated, a correlation between them was obtained. The gas flow rate was varied to obtain multiple data points. Higher gas flow rates led to lower saturation levels because of the higher shear

rates associated with the higher gas flow rates, and vice versa.

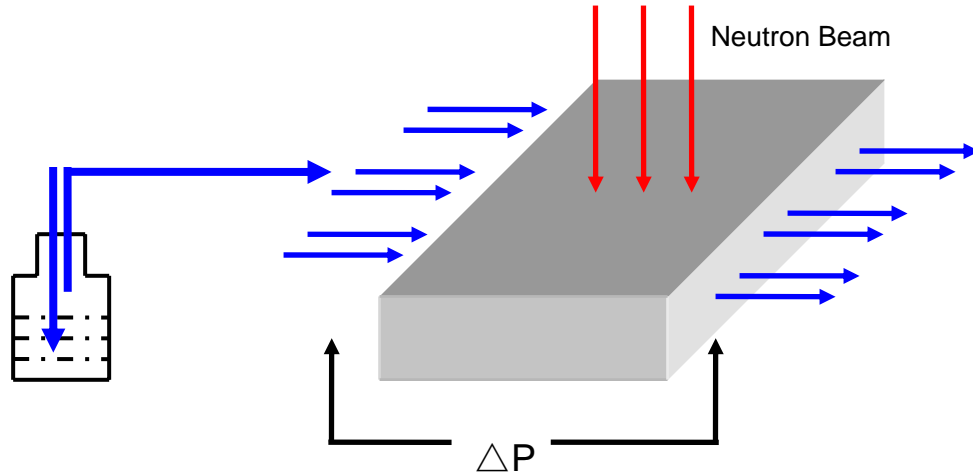


Figure 2.1 Schematic of the relative permeability experiment.

Permeability by neutron imaging: The permeability of the porous medium tested in this experiment was calculated by Darcy's law using Eq. 2.2. Saturation levels of the porous medium were derived from the changes of the intensity of a neutron beam between the incident beam and the transmitted beam. Details of the mechanism by which the neutron imaging works were presented in reference 19. The image collecting rate is one picture per second and the resolution of the picture is 125 microns per pixel.

Fig. 2.1 illustrates how the in-situ liquid saturation levels in the sample were measured by neutron imaging during the experiment. Fig. 2.2 shows a neutron image

of the relative permeability fixture, in which a wet sample can be clearly seen. The procedures of the neutron imaging test are similar to those of the gravimetric analysis test. The only difference between these two methods lies in the method of determining the saturation levels in the wet sample. The procedure of the neutron imaging method is described as follows.

- 1) Pre-saturate a sample in de-ionized water at 80 °C for 1 hour followed by cooling down to ambient temperature.
- 2) Assemble the saturated sample in the fixture shown in Fig. 2.1.
- 3) Flow gas through the saturated sample, record pressure drop (ΔP), and acquire neutron images of the wet sample.
- 4) Flow dry air after the experiment to dry the sample.
- 5) Acquire neutron images of the dry sample. Images of the dry sample serve as references (backgrounds) to be subtracted from the neutron images of the wet sample to calculate the saturation levels.
- 6) Turn off the neutron beam and stop the experiment.

The saturation levels were calculated from the neutron images obtained in steps 3 and 5. The corresponding permeability was derived from the pressure drop across the gas flow path using Darcy's law shown in Eq. 2.2.

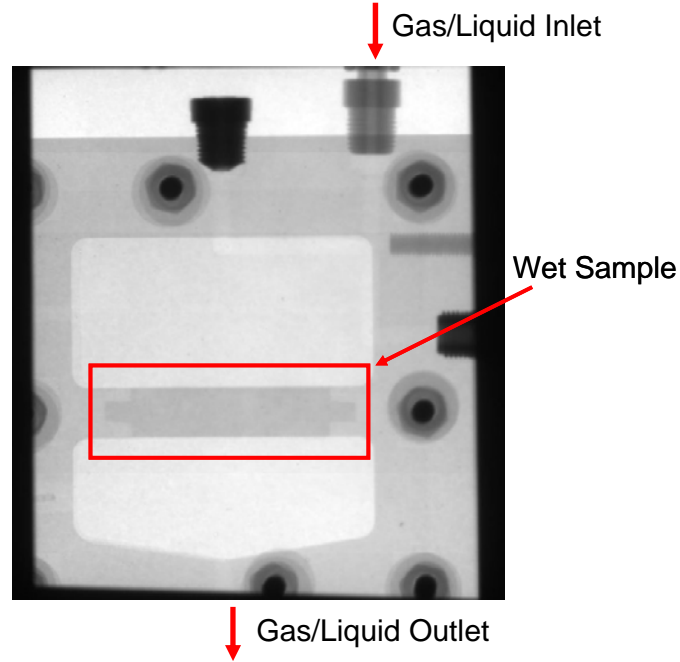


Figure 2.2 Neutron image (top view) of the relative permeability setup.

2.2.3 Liquid Permeability

Neutron imaging technology as shown in Fig. 2.1 was used to measure the liquid permeability. The ex-situ permeability measurement showed an inconsistency of saturation levels because once the liquid pressure was removed, part of the liquid water may be repelled out of the sample as a result of the sample hydrophobic pore surface. Similar to gas permeability shown in Eq. 2.2, liquid permeability is calculated by

$$\overline{k_l} = - \frac{v_l \mu_l}{\frac{\Delta P_l}{\Delta x_l}} \quad [2.3]$$

where v_l is the liquid velocity; μ_l is the liquid viscosity; $\overline{\Delta P_l}$ is the liquid

pressure drop; Δx_l is the liquid traveling path. The liquid velocity is assumed to be constant for the same reason as stated earlier.

Contrary to the gas permeability measurement which started with a pre-saturated sample, the liquid permeability measurement starts with a dry sample. As the liquid displaces the gas phase when it flows through the sample, in-situ saturation levels are calculated from the change of the neutron beam intensities. The liquid permeability test includes three steps as follows.

- 1) Assemble a dry sample into the setup and acquire neutron images of the dry sample as reference or background images.
- 2) Flow liquid water through the sample as shown in Fig. 2.1, record liquid pressure drop, and acquire neutron images.
- 3) Turn off the neutron beam and stop the experiment at the end of the experiment.

The saturation levels and liquid permeability were calculated from the obtained neutron images and the pressure drop obtained in step 2. In order to measure the permeability at different saturation levels, liquid flow rate was adjusted during the experiment. A high saturation level is expected with a high liquid flow rate because at high liquid pressure more liquid water is expected to displace more void space in the porous medium.

The experimental conditions are summarized in Table 2.2. The sample size for the gas and liquid permeability measurement is 4 cm \times 1 cm excluding the shoulders for sealing purposes. See Figs. 2.1 and 2.2. Gas and liquid traveling distance is equal to the width of the samples (1cm). The gas and liquid relative permeability experiment was conducted at ambient temperature. The outlet of the fixture is open to the air. Thus, the outlet pressure is assumed to be constant at 1 atm in this experiment.

Table 2.2 Experimental conditions.

| Material Type | Fluid Traveling Distance (cm) | Flow Rate |
|---------------------------------------|--------------------------------------|-------------------------------------------|
| A1 (Proprietary GDL) | 1 | 20 SCCM |
| A3 (Proprietary GDL) | 1 | 60 SCCM |
| SGL-10CA (Carbon Group) | 1 | From 1.01 to 1.30 cm ³ /min |
| TGP-H-060 (Toray Industries, Inc.) | 1 | From 1.01 to 1.30 cm ³ /min |

SCCM: standard cubic centimeter per minute

2.3 Results and Discussion

2.3.1 Gas Relative Permeability

Fig. 2.3 shows the gas phase pressure drop and the corresponding permeability of the material A1. At the beginning of the experiment, when the gas phase started to flow through the pre-saturated sample, sufficient pressure drop had to be created to displace the liquid phase. After the gas phase broke through the liquid phase, the gas

phase pressure drop decreased significantly. After 60 minutes, the saturation level in the sample was close to the residual saturation, which could not be displaced by the gas phase at this shear rate. At this stage, the gas phase pressure drop across the sample approached stability. The gas permeability changes corresponded to the change of the gas phase pressure drop as shown in Fig. 2.3. Since the experiment started with a pre-saturated sample, the gas permeability was very low at the beginning of the experiment. The measured permeability continuously increased as the liquid phase was displaced by the gas phase until the saturation level in the sample was close to the residual saturation at the end of 60 minutes. Pressure spikes observed after 60 minutes are likely due to the redistribution of the residual liquid water inside the porous GDL.

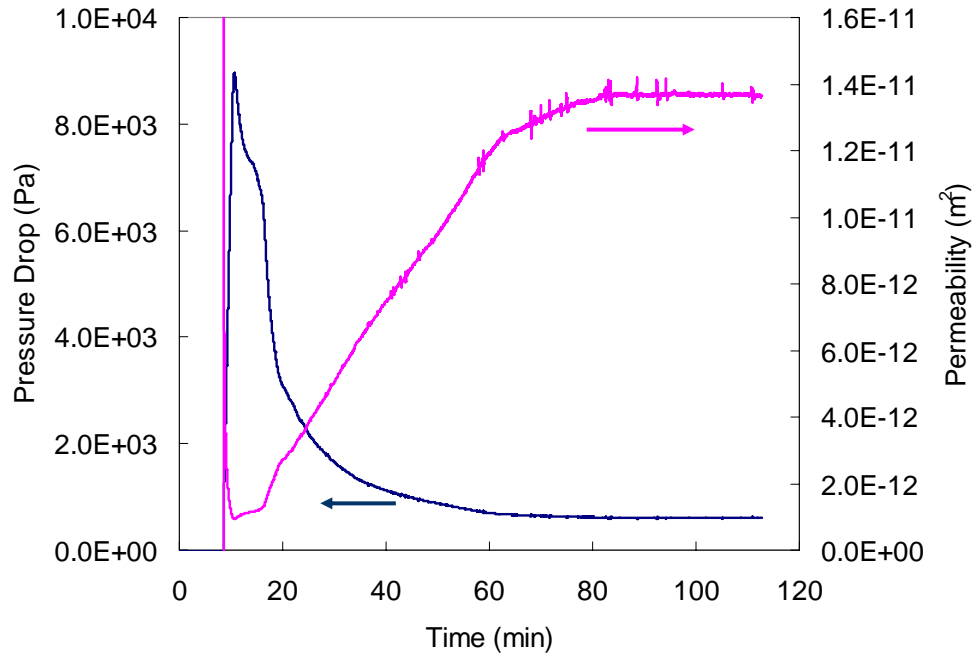


Figure 2.3 Pressure drop and permeability of the material A1.

In the first 20 minutes, gas pressure drops greatly as shown in Fig. 2.3. The neutron images were averaged every 50 images (50 seconds) in the first 20 minutes. When the gas pressure approached steady state, the saturation levels became stable represented by stable pressure drop across the sample. Thus, after 20 minutes the neutron images were averaged every 200 images (200 seconds). From the grayness of these averaged density pictures and dry background pictures, liquid water saturation levels were derived based on the calibrated neutron beam parameters.

The relative permeability by gravimetric analysis and neutron imaging of material A1 were compared in Fig. 2.4. It was seen that at the same permeability, the

saturation level by the gravimetric analysis was higher than that of the neutron imaging. This discrepancy could be attributed to the fact that liquid water may be imbibed into the sample when the gas phase pressure was removed at the end of the gravimetric experiment. Neutron image showed that the liquid water displaced by the gas phase remained on the edge of the sample, as shown in Fig. 2.5, and could be re-imbibed into the sample again once the gas pressure was removed. As discussed in the previous part of this chapter, the liquid saturation level decreased drastically at the beginning of the experiment (high saturation level range), after which the saturation level dropped more gradually. During the process that the saturation levels dropped continuously, liquid water droplets could redistribute in a sample before they detached from the sample. Fig. 2.4 also showed that a 3rd-order power correlation in the form of²⁰

$$k_g = k_0 (1 - s)^3 \quad [2.4]$$

where k_0 is the absolute permeability of a single phase, fitted the data of the gravimetric experiment a bit better than those of the neutron imaging. The 3rd-order power correlation was developed for nonconsolidated and well sorted sand. This shows that the 3rd-order power correlation cannot be used to predict the relative permeability of the sample A1 especially in the in-plan direction. Polynomial correlations of the gravimetric analysis and neutron imaging data was also shown in

Fig. 2.4.

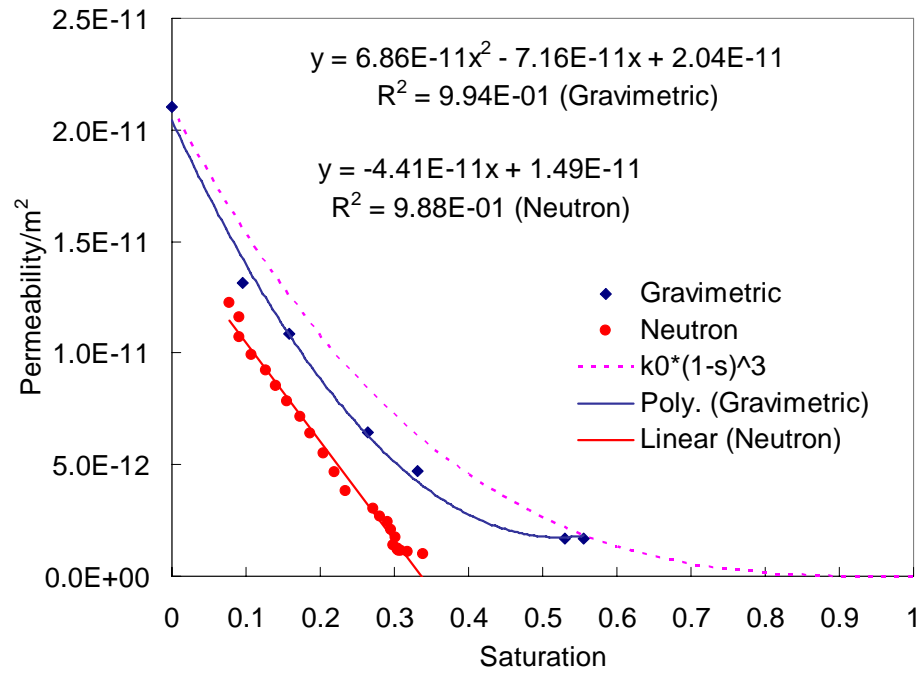


Figure 2.4 Gas relative permeability of the material A1.

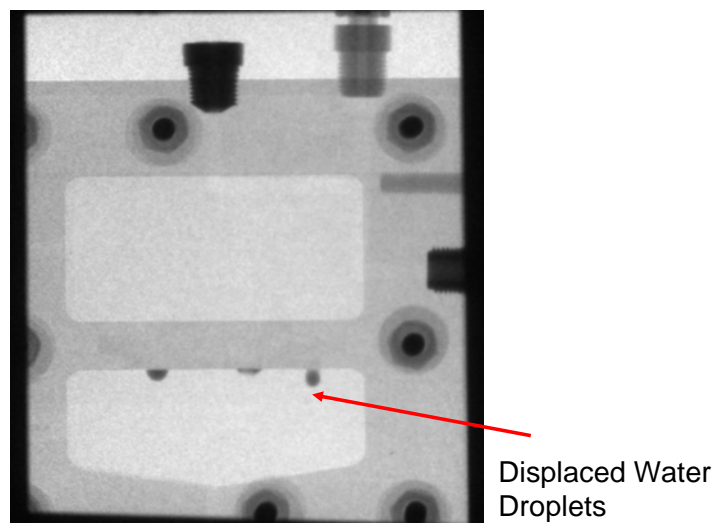


Figure 2.5 Water displacement in a sample.

The 3rd-order power correlation in Eq. 2.4 was developed for non-consolidated and well-sorted sand. The porous GDLs used in PEM fuel cells have different morphological and surface properties as a result of the carbon fibers which have a preferred in-plane layout. The special asymmetric property of the GDLs may explain the discrepancy between the 3rd-order power correlation and neutron imaging data.

The gas phase pressure drop and permeability of the material A3 were shown in Fig. 2.6. Similar to the phenomena observed in Fig. 2.3, sufficient gas pressure had to be created to break through the pre-saturated sample. A steep decrease of gas pressure drop and increase of gas permeability followed by a stable pressure and permeability were seen in Fig. 2.6. When gas started to flow through the sample, liquid water purged from the sample accumulated on the edge of the sample at the outlet as droplets. During this time, the pressure drop and permeability remained stable as seen in the 20-70 minute region in Fig. 2.6. Once the liquid droplets fell off the edge of the sample which allows more liquid water to be purged from the sample, the gas pressure drop began to decrease and continue until the saturation in the sample reached the residual level.

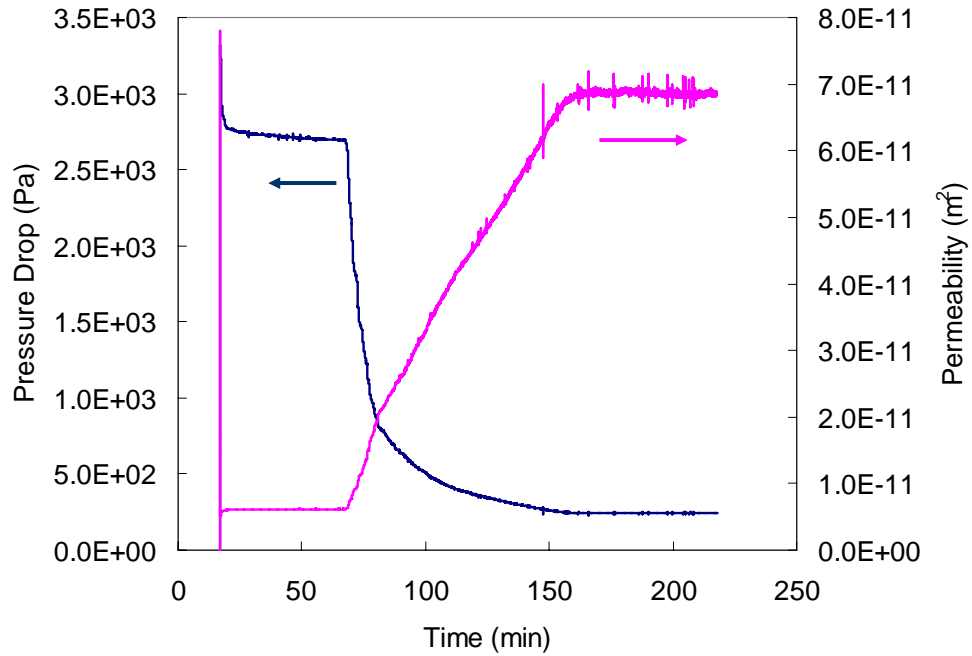


Figure 2.6 Pressure drop and permeability of the material A3.

The saturation levels in material A3 were derived from the grayness of the density pictures. The density pictures were summarized and averaged in a similar way to that of material A1. When the pressure slope was steep, fewer neutron images were averaged to catch the change of saturation levels because the saturation levels drops greatly. When the pressure slope was low, more neutron images were averaged because the saturation levels were stable. In the liquid relative permeability measurement that follows, saturation levels were determined similarly based on the change of the liquid pressure drop.

Gas relative permeability of the material A3 is shown in Fig. 2.7. Gas

permeability by gravimetric analysis, neutron imaging, and 3rd-order power correlation had similar saturation levels in the range of 0 to 0.3, which showed that the 3rd-order power correlation provided a good fit to the experimental data in the low saturation level range for the material A3. Beyond the saturation level of 0.3, the gravimetric method showed higher saturation levels which could be attributed to the liquid water being re-imbibed into the sample when the gas pressured was terminated.

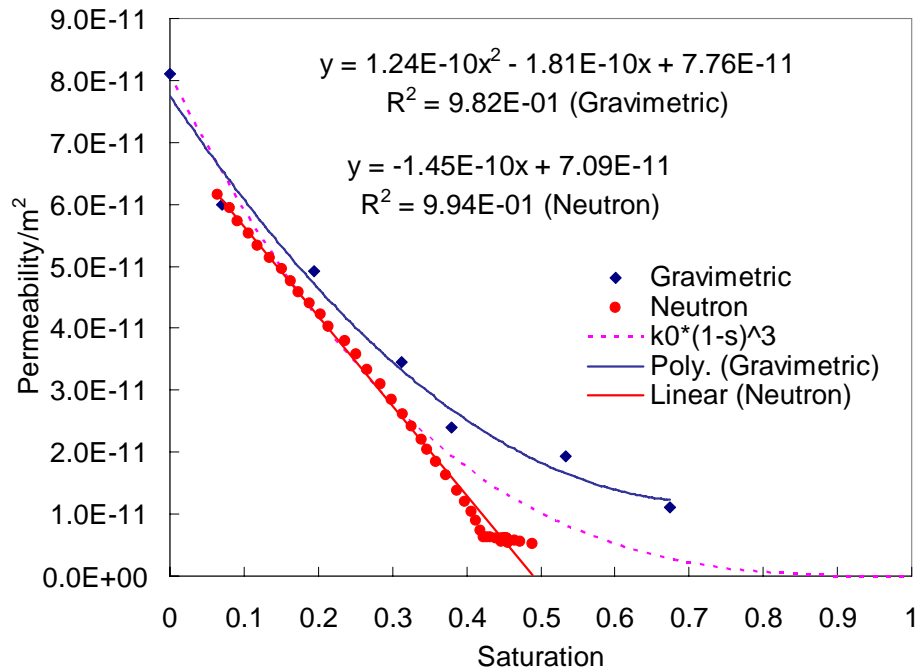


Figure 2.7 Gas relative permeability of the material A3.

2.3.2 Liquid Relative Permeability

Multiple liquid water flow rates were used in measuring the liquid permeability

of the material SGL 10CA as shown in Fig. 2.8. Liquid water flow rate of 1.01 ml/min was first set from 0 to 41 min followed by the flow rate of 1.11 ml/min from 42 min to 66 min, 1.20 ml/min from 67 min to 92 min, and 1.30 ml/min from 93 min to 117 min. It was seen that liquid permeability was stable during the time range of 0 to 66 min because liquid water could not displace more gas phase in the porous material even when the liquid flow rate was increased from 1.01 ml/min to 1.11 ml/min. However, further increase of the liquid water flow rate from 1.11 ml/min to 1.20 ml/min resulted in a lower liquid pressure drop and higher liquid permeability as more gas phase was displaced under high liquid flow rate. A further increase of the liquid flow rate to 1.30 ml/min led to a higher pressure drop and minor change of permeability.

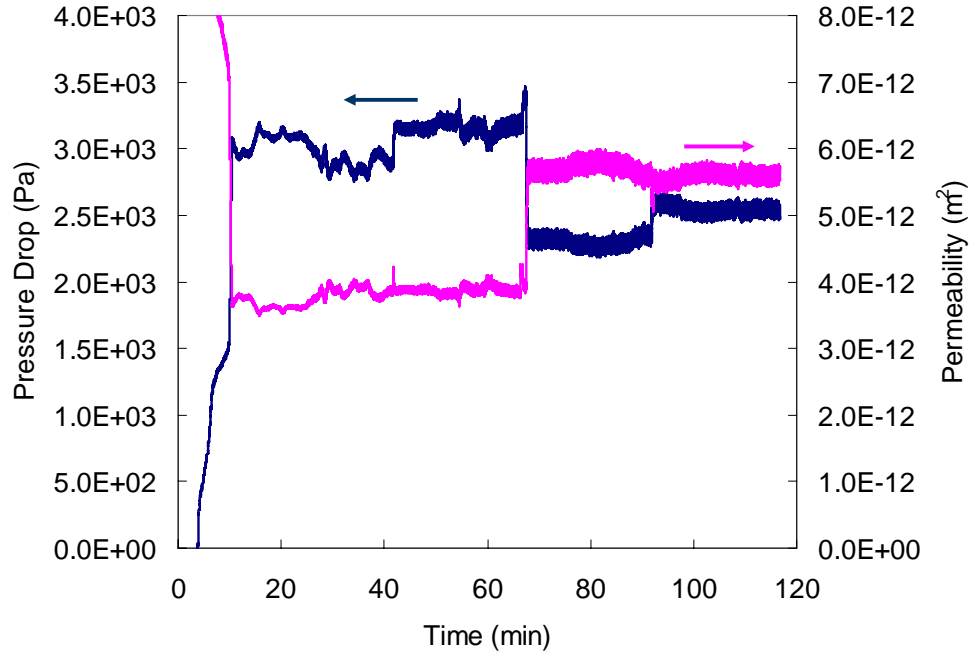


Figure 2.8 Pressure drop and permeability of the material SGL 10CA.

Fig. 2.9 showed the liquid relative permeability by neutron imaging of the material SGL 10CA and a 3rd-order power correlation in the form of²⁰

$$k_l = k_0 s^3 \quad [2.5]$$

The difficulty of obtaining the permeability at both high and low saturation levels was observed in this experiment. On one hand, gas phase may be trapped inside the material at high liquid water saturation levels as dead pockets, making it difficult to measure the permeability at a high saturation level. On the other hand, liquid saturation may have to reach a certain level before continuous liquid water flow across the sample could occur, making it difficult to measure the liquid permeability

at low liquid saturation level. Fig. 2.9 showed that there was a discrepancy between the permeability by neutron imaging and the 3rd-order power correlation, illustrating that the 3rd-order power correlation was inappropriate for SGL 10CA with its special porous geometry.

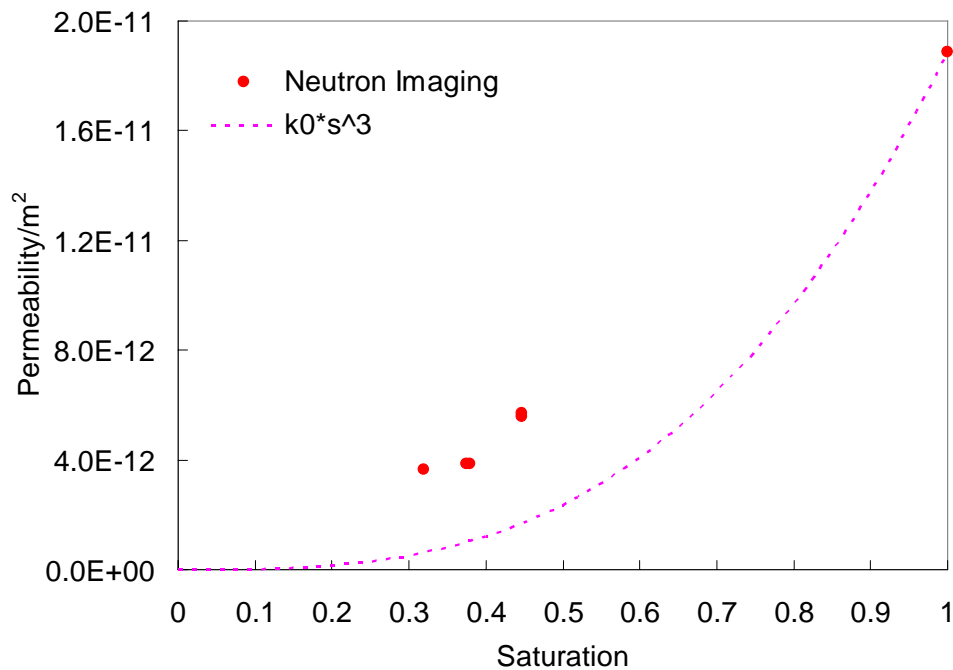


Figure 2.9 Liquid relative permeability of the material SGL 10CA.

The liquid pressure drop and relative permeability of another porous material, Toray TGP-H-060 with 30 %wt PTFE, is shown in Fig. 2.10. Similar to the experiment of the SGL 10CA, liquid flow rates were 1.01 ml/min from 0 to 42 min, 1.11 ml/min from 43 min to 78 min, 1.20 ml/min from 79 min to 100 min, and 1.30

ml/min from 101 min to 127 min. It was seen that the liquid pressure drop fluctuated greatly with the change of liquid flow rate due to the redistribution of liquid water inside the sample. The liquid relative permeability increased slightly with the increase of the liquid flow rate since more gas phase was displaced with higher shear force created by the higher liquid flow rate. The stable liquid pressure drop observed may be attributed to the fact that the increased liquid saturation level at higher liquid flow rate resulted in higher permeability, which compensated for the increased liquid flow rate.

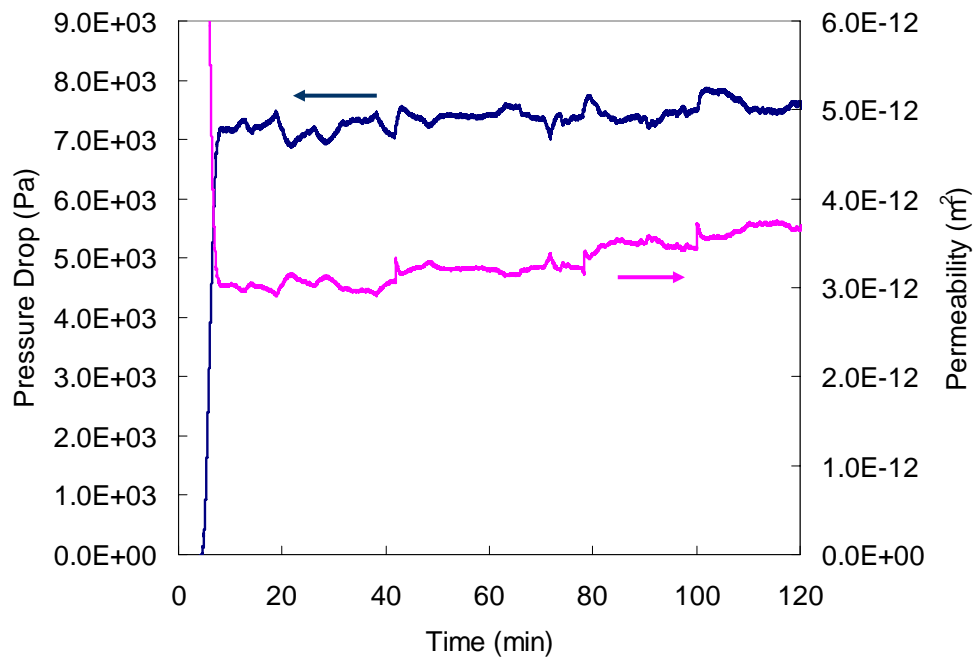


Figure 2.10 Pressure drop and permeability of the material Toray TGP-H-060 (30 %wt PTFE).

Fig. 2.11 shows that liquid relative permeability by the neutron imaging can be predicted reasonably well by the 3rd-order power correlation. Liquid permeability increased with saturation level as the liquid flow rate increased. In the liquid relative permeability measurement, only a few data points in the saturation range of 0.5 to 0.8 could be obtained due to the difficulty explained earlier.

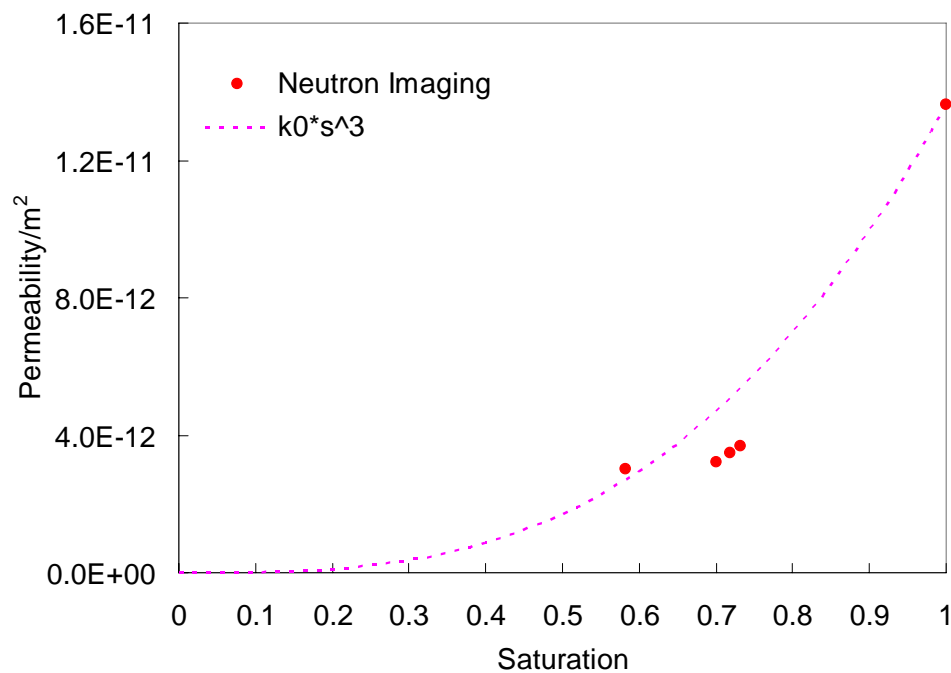


Figure 2.11 Liquid relative permeability of the material Toray TGP-H-060 (30 %wt PTFE).

2.4 Conclusions

This chapter investigated gas and liquid relative permeability of porous GDLs used in PEM fuel cells by gravimetric analysis and neutron imaging. Gas phase relative permeability of two proprietary GDLs showed that permeability obtained by the gravimetric analysis and neutron imaging showed good agreement at low saturation levels. Discrepancies between these two methods arose at high saturation levels and can be attributed to the re-imbibition of liquid water at the end of the experiment in the gravimetric method. Liquid relative permeability of two commercially available GDLs showed that permeability increased with the liquid flow rate, resulting from the increase of saturation levels in the porous materials at high liquid flow rate. The impact of the liquid flow rate on the liquid pressure drop and permeability was insignificant, which may be resulted from the small change of the liquid flow rate used in this experiment. Due to dead air pockets in the porous GDLs and a certain liquid saturation level needed for the liquid to penetrate through the GDLs, liquid relative permeability was difficult to obtain at both high and low saturation levels. This study also showed that the 3rd-order power correlation of gas and liquid permeability was inappropriate for the porous media used in PEM fuel cells because those materials have a different structure from well sorted hydrophilic sands. The only exception was the liquid relative permeability of Toray TGP-H-060

with 30 %wt PTFE.

2.5 References

1. X. Wang and T. V. Nguyen, Modeling the Effects of the Micro-Porous Layer on the Net Water Transport Rate Across the Membrane in a PEM Fuel Cell, *J. Electrochem. Soc.*, in press, **2010**.
2. R. Friedmann and T. V. Nguyen, Optimization of the Cathode Catalyst Layer Composition Using a Novel 2-Step Preparation Method, *ECS Trans.*, 16 (2), 2021, **2008**.
3. M. F. Mathias, J. Roth, J. Fleming and W. Lehnert, Diffusion Media Materials and Characterisation. In *Handbook of Fuel Cells - Fundamentals, Technology and Applications*, W. Vielstich, H. A. Gasteiger and A. Lamm, Eds. John Wiley & Sons, Ltd.: Vol. 3: Fuel Cell Technology and Applications, pp 517, 2003.
4. W. He, J. S. Yi and T. V. Nguyen, Two-Phase Flow Model of the Cathode of PEM Fuel Cells Using Interdigitated Flow Fields, *AIChE J.*, 46 (10), 2053, **2000**.
5. G. Lin, W. He and T. V. Nguyen, Modeling Liquid Water Effects in the Gas Diffusion and Catalyst Layers of the Cathode of a PEM Fuel Cell, *J. Electrochem. Soc.*, 151 (12), A1999, **2004**.
6. D. Natarajan and T. V. Nguyen, A Two-Dimensional, Two-Phase, Multicomponent,

- Transient Model for the Cathode of a Proton Exchange Membrane Fuel Cell Using Conventional Gas Distributors, *J. Electrochem. Soc.*, 148 (12), A1324, **2001**.
7. U. Pasaogullari, C.-Y. Wang and K. S. Chen, Two-Phase Transport in Polymer Electrolyte Fuel Cells with Bilayer Cathode Gas Diffusion Media, *J. Electrochem. Soc.*, 152 (8), A1574, **2005**.
 8. Q. Ye and T. V. Nguyen, Three-Dimensional Simulation of Liquid Water Distribution in a PEMFC with Experimentally Measured Capillary Functions, *J. Electrochem. Soc.*, 154 (12), B1242, **2007**.
 9. A. Z. Weber, R. M. Darling and J. Newman, Modeling Two-Phase Behavior in PEFCs, *J. Electrochem. Soc.*, 151 (10), A1715, **2004**.
 10. J. T. Gostick, M. W. Fowler, M. D. Pritzker, M. A. Ioannidis and L. M. Behra, In-Plane and Through-Plane Gas Permeability of Carbon Fiber Electrode Backing Layers, *J. Power Sources*, 162 (1), 228, **2006**.
 11. V. Gurau, M. J. Bluemle, E. S. De Castro, Y.-M. Tsou, T. A. Zawodzinski Jr. and J. A. Mann Jr, Characterization of Transport Properties in Gas Diffusion Layers for Proton Exchange Membrane Fuel Cells 2. Absolute Permeability, *J. Power Sources*, 165 (2), 793, **2007**.
 12. J. Ihonon, M. Mikkola and G. Lindbergh, Flooding of Gas Diffusion Backing in

- PEFCs - Physical and Electrochemical Characterization, *J. Electrochem. Soc.*, 151 (8), A1152, **2004**.
13. M. V. Williams, E. Begg, L. Bonville, H. R. Kunz and J. M. Fenton, Characterization of Gas Diffusion Layers for PEMFC, *J. Electrochem. Soc.*, 151 (8), A1173, **2004**.
14. J. Benziger, J. Nehlsen, D. Blackwell, T. Brennan and J. Itescu, Water Flow in the Gas Diffusion Layer of PEM Fuel Cells, *J. Membrane Sci.*, 261 (1-2), 98, **2005**.
15. A. B. Geiger, A. Tsukada, E. Lehmann, P. Vontobel, A. Wokaun and G. G. Scherer, In Situ Investigation of Two-Phase Flow Patterns in Flow Fields of PEFC's Using Neutron Radiography, *Fuel Cells*, 2 (2), 92, **2002**.
16. D. S. Hussey, D. L. Jacobson, M. Arif, J. P. Owejan, J. J. Gagliardo and T. A. Trabold, Neutron Images of the Through-Plane Water Distribution of an Operating PEM Fuel Cell, *J. Power Sources*, 172 (1), 225, **2007**.
17. T. Kim, J. Kim, C. Sim, S. Lee, M. Kaviany, S. Son and M. Kim, Experimental Approaches for Distribution and Behavior of Water in PEMFC under Flow Direction and Differential Pressure Using Neutron Imaging Technique, *Nucl. Instrum. Methods Phys. Res., Sect. A*, 600 (1), 325, **2009**.
18. T. Kim, J. Kim, C. Sim, S. Lee, Y. Son and M. Kim, Experimental Approaches for Water Discharge Characteristics in PEMFC Using Neutron Imaging Technique at

- Conrad, HMI, *Nucl. Eng. Technol.*, 41 (1), 135, **2009**.
19. R. Satija, D. L. Jacobson, M. Arif and S. A. Werner, In Situ Neutron Imaging Technique for Evaluation of Water Management Systems in Operating PEM Fuel Cells, *J. Power Sources*, 129 (2), 238, **2004**.
20. M. Kaviany, *Principles of Heat Transfer in Porous Media*, 2nd ed.; Springer-Verlag: New York, p 708, 1995.

Chapter 3

Experimental Evaluation of Saturation Levels in the Cathode side and Cell Performance of a PEM Fuel Cell

3.1 Introduction

Water management in a PEM fuel cell plays an important role in obtaining optimal fuel cell performances. As a part of the MEA, the GDL provides a transport path for electrons, gas, and liquid water.¹ Fast transport of liquid water in the GDL leads to low saturation levels in the GDL and fast gas transport to the active catalyst sites, which is important when the gas transport in the GDL is dominant. The two-phase flow properties of the porous media affect the liquid saturation level in the GDL greatly. Modeling results showed that a hydrophobic GDL could contribute to better fuel cell performance by lowering the liquid saturation levels in the GDL.² Quantification of the liquid saturation level in the GDL will be helpful in validating these two-phase flow models and determining the liquid water's role in affecting fuel cell performance.

Continual efforts have been made to determine the liquid saturation levels in the MEAs of PEM fuel cells. Optical visualization (transparent fuel cell),^{3, 4} nuclear magnetic resonance (NMR),⁵⁻⁷ X-CT (X-ray computed tomography),^{8, 9} and neutron

imaging¹⁰⁻¹⁴ were used to determine the liquid water content in PEM fuel cells. Apparently, only transparent materials are suitable for optical visualization, which limits its application to the PEM fuel cells. The presence of the magnetically inductive carbon fibers limits the NMR's application to GDLs. High resolution X-rays are limited by the dimensions of the sample. High resolution neutron imaging is capable of measuring the through-plane liquid water distribution in a MEA of a fuel cell. However, limited availability of neutron facility is a major drawback to most users.

He *et al.*¹⁵ developed a diagnostic tool to predict the flooding effect in a PEM fuel cell by taking advantage of the gas pressure drop signal from gas flowing through a GDL when an interdigitated flow field was used. The study showed that cathode flooding was the main cause of poor fuel cell performance when the current density approached the limiting current density region. It was also shown that this technique could be used to determine the change in the liquid water saturation level in the GDL when the gas flow rate was changed. However, the liquid water content in the GDL could only be inferred by the gas phase pressure drop across the GDL. So unless the water content in the GDL was measured directly by some imaging techniques, such as neutron imaging, the alternative way is to have a correlation between the gas relative permeability and the saturation level in the GDL. That is, if the gas flow rate is

known along with the pressure drop across a GDL due to gas flow through a GDL when an interdigitated flow field is used, the gas relative permeability can be calculated. Next, the saturation level in the GDL can be determined from the gas relative permeability and saturation level correlation. Empirical correlations similar to the ones discussed in Chapter 2 were used before the experimentally measured relative permeability was available.¹⁶⁻²¹ One of these empirical correlations is the 3rd-order power correlation between the liquid saturation level and the relative permeability developed for nonconsolidated and well-sorted sand.²² However, the porous GDLs used in PEM fuel cells are either non-woven papers or woven cloth made of carbon fibers. These granular carbon fibers lead to anisotropic two-phase flow properties in the GDL, resulting from the carbon fibers with a preferred in-plane layout. Thus, using the 3rd-order power relative permeability measured for sands often lead to inaccurate predictions. The other empirical relative permeability correlations described in Chapter 2 that have not been validated by the experiments have the same problem of predicting accurately the liquid water saturation levels in the porous media. Yamada *et al.*²³ was the first to apply the approach of using the pressure drop signal across a GDL used with an interdigitated flow field proposed by Trung V. Nguyen as a diagnostic tool to study the water flooding in the cathode GDL of a PEM fuel cell. The water flooding effect was also validated by Yamada *et al.*'s numerical

simulation based on the approach developed by Natarajan and Nguyen.¹⁸

In recent years, absolute gas permeability of the GDLs used in PEM fuel cells has become available.²⁴⁻²⁶ Our group studied the measurement of both gas and liquid relative permeability. Correlations between the relative permeability and the saturation levels that could be used directly in models to predict the liquid water movement were fitted based on the experimentally measured results. The gravimetric method and in-situ neutron imaging technique used to determine the liquid water amount in the GDLs were presented in Chapter 2. In this chapter, the measured correlations of relative permeability and saturation levels were applied to a PEM fuel cell with interdigitated flow field to predict the liquid water saturation levels in the GDLs.

3.2 Experimental

3.2.1 Setup

Fig. 3.1 shows the experimental setup used in this experiment. This allows for the determination of saturation levels in the cathode GDL under serpentine flow mode and interdigitated flow mode, respectively. The saturation level in the GDL was calculated from the correlation between the permeability and saturation level determined in Chapter 2. The pressure drop between the air inlet and outlet was monitored to calculate the permeability of the GDL used in the experiment. The

serpentine flow and interdigitated flow field are shown in Fig. 3.1 (a) and (b), respectively. A cross-sectional view of the interdigitated flow is shown in Fig. 3.1 (c).

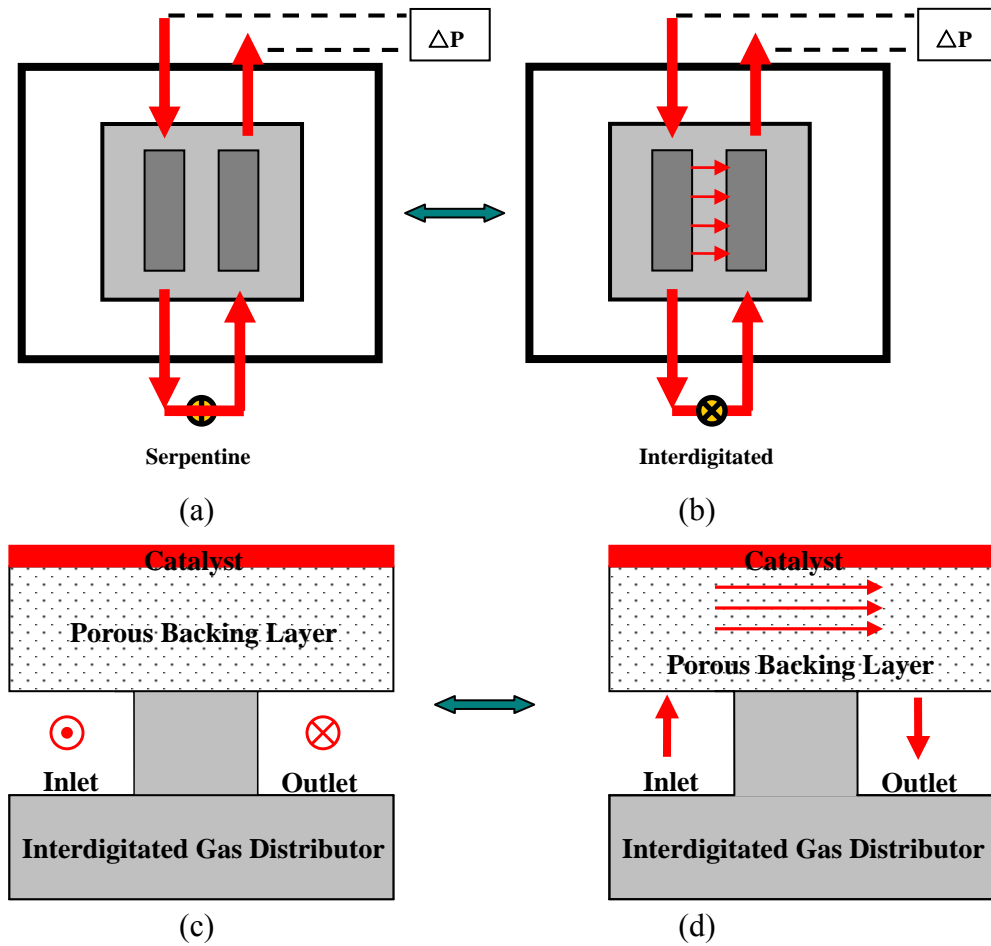


Figure 3.1 Schematic of (a) a serpentine flow field, (b) an interdigitated flow field, (c) a cross-sectional view of the serpentine flow field, and (d) a cross-sectional view of the interdigitated flow field. \odot represents gas flowing out of the surface, and \otimes represents gas flowing into the surface.

3.2.2 Procedure

The experimental procedure to measure the liquid saturation level in the GDL is as follows.

- (1) The fuel cell was operated in galvanostatic (constant-current) mode to precisely control the gas stoichiometric flow rate. This mode also allows the water generation rate in the cathode to be controlled. A new MEA was activated by scanning the polarization curve twice and staying at low voltage 0.4V for several hours to fully hydrate the membrane. The test began after the MEA was fully activated.
- (2) The fuel cell was first operated under serpentine flow mode. Once the fuel cell performance became steady, the fuel cell was switched to interdigitated flow mode at the same current density and maintained in this mode until its performance also became steady. Even though it was found during this study that steady state performance was achieved in less than 5 minutes, the fuel cell was operated for 15 mins under each mode. The pressure drop, fuel cell voltage, cell temperature, and humidifier temperatures were monitored continuously under both serpentine and interdigitated flow modes.
- (3) Step 2 was repeated at each different current density until the fuel cell reached the mass transport limiting region. In the mass transport limiting

region, unstable fuel cell voltage was observed, which ultimately led to fuel cell failure as the cell voltage dropped below 0.1V under the galvanostatic mode. To prevent fuel and oxidant starvation and fuel cell failure, the flow rates of air and hydrogen were adjusted before the current density was changed from a low current density to a higher current density. Similarly, when the current density was changed from a high level to a lower level, the air and hydrogen flow rates were adjusted after the current density was changed.

The pressure drop was measured by an OMEGA PX 139 (Omega Engineering, Inc.) pressure transducer (± 5 Psi) and recorded by a data acquisition system (Personal Daq System by Omega Engineering, Inc.). The fuel cell current was controlled and the voltage was monitored by a computer controlled potentiostat/galvanostat (Arbin System, Inc.). The temperatures of the fuel cell and humidifiers were kept constant at 70 °C. Nafion membrane 112 was used in the MEAs. Carbon supported platinum catalyst with 20 % wt Pt (Tanaka Kikinzoku Kogyo K. K., Japan) was used. The catalyst loading of each electrode was 0.48 mg Pt/cm². The MEA has an active area of 2.08 cm by 0.65 cm. The same electrode material was used for the cathode and anode. The MEA was made by hot compressing the electrodes and the Nafion membrane under 1.47×10^6 Pa at 135 °C for 5 mins.

The fuel cell was assembled under 3.78×10^6 Pa.

In this experiment, the anode and cathode gas flow stoichiometries were kept at 2 and 4, respectively. Co-flow configuration of the gases in the anode and cathode was used. During the fuel cell test, the anode was kept with interdigitated flow. The fuel cell operation conditions are summarized in Table 3.1.

| Table 3.1 Fuel cell operation conditions. | |
|----------------------------------------------------------|-----------|
| Flow Stoichiometry (Anode/Cathode) | 2/4 |
| Fuel cell pressure | 1 atm abs |
| T_{cell} | 70 °C |
| T_{humid} (Anode/Cathode) | 70/70 °C |
| Flow configuration | Co-flow |
| T_{cell} is the temperature of the fuel cell; | |
| T_{humid} is the temperature of the humidifier. | |

The GDLs were compressed when assembling an MEA into a fuel cell in order to seal the gases. However, the gas relative permeability was tested under a lower compressed condition. It is assumed that compression has the same effect on the absolute permeability and relative permeability. Thus, the relative permeability under one compression level can be calibrated to another compressed level using the absolute values at these compressed states.

3.2.3 Materials

Two types of proprietary GDLs, B1 and B3, were used as gas transport media in

this experiment. The properties of B1 and B3 are listed in Table 3.2. Catalyst layers were prepared by applying the Pt/Carbon and Nafion ink onto the porous gas diffusion media (B1 and B3). TVN System, Inc. prepared the electrodes used in this experiment. The cathode and anode electrodes were made of the same materials.

B1 is a bi-layer porous medium with the base support layer (BSL) of A1 and an MPL pasted on the base support. Similarly, B3 is a bi-layer porous medium with the base support layer of A3 and an MPL pasted on the base support. Thus, the permeability correlations of the GDLs (A1 and A3) measured in Chapter 2 can be used in this chapter to determine the liquid water saturation levels in the electrode.

Table 3.2 Properties of gas transport media used in the experiment.

| Material Type | Base Support Layer (BSL) | BSL Thickness (μm) | BSL Porosity | PTFE Content in BSL (%wt) |
|----------------------|---------------------------------|-----------------------------------------------------|---------------------|----------------------------------|
| B1 | A1 (Proprietary GDL) | 216 | 0.81 | 0 |
| B3 | A3 (Proprietary GDL) | 325 | 0.85 | 5 |

3.3 Results and Discussion

3.3.1 Relative Permeability Correlations

In the previous chapter, experimentally determined relative permeability of the porous media used in this study was investigated. The permeability measured by

gravimetric analysis and neutron imaging showed good agreement at low saturation levels. For the two proprietary GDLs used here, the measured correlations between the permeability and saturation level were given as

$$\text{A1: } k_g = 6.86 \times 10^{-11} s^2 - 7.16 \times 10^{-11} s + 2.04 \times 10^{-11}, m^2 \quad [3.1]$$

$$\text{A3: } k_g = 1.24 \times 10^{-10} s^2 - 1.81 \times 10^{-10} s + 7.76 \times 10^{-11}, m^2 \quad [3.2]$$

Eqs. 3.1 and 3.2 are explicit expressions of gas permeability as functions of the liquid water saturation level. In order to determine the liquid saturation level explicitly, the saturation levels versus permeability were plotted in Fig. 3.2. Correlations were fitted as

$$\text{A1: } s = 1.56 \times 10^{21} k_g^2 - 6.23 \times 10^{10} k_g + 0.628 \quad [3.3]$$

$$\text{A3: } s = 1.16 \times 10^{20} k_g^2 - 1.99 \times 10^{10} k_g + 0.858 \quad [3.4]$$

Once the permeability was obtained from the pressure drop measurement, the saturation level can be calculated using Eqs. 3.3 and 3.4.

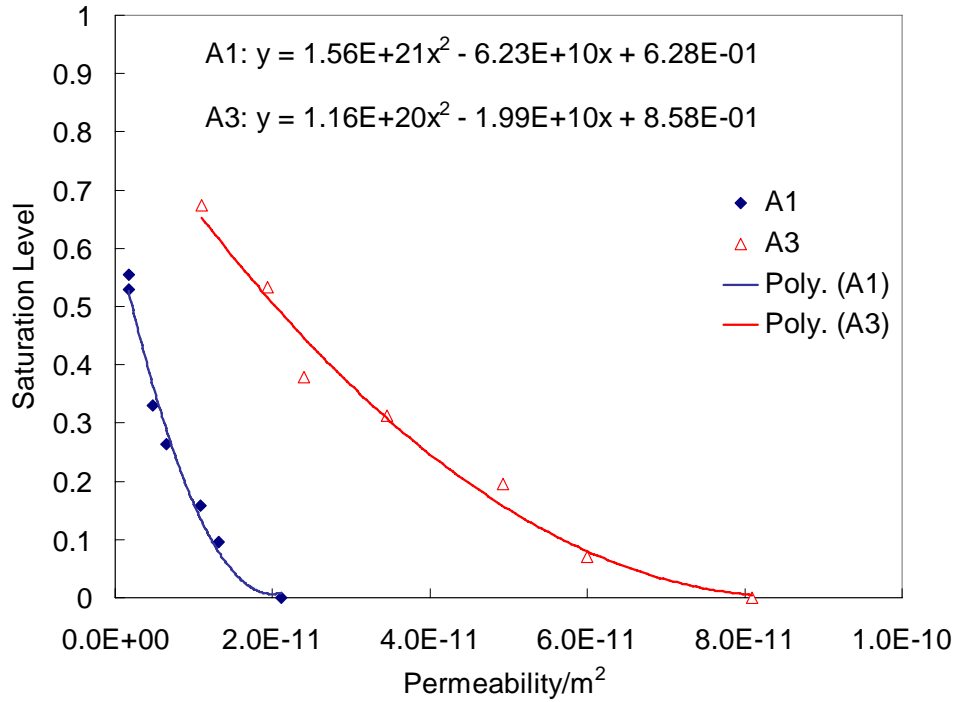


Figure 3.2 Correlation between saturation level and permeability.

3.3.2 Base Case

The voltage, current density and pressure drop versus time for sample B1 are shown in Fig. 3.3. First, the pressure drop in the serpentine mode was stable and negligible since the resistance in the flow channel was small due to the short pathway of the channel. Second, two different phenomena were observed in the interdigitated mode: a stable pressure drop at low current density and a decreasing pressure drop at high current density. At low current density, little water accumulated in the porous GDL since both the water generation rate and electro-osmosis rate were low. The water saturation levels under serpentine flow and interdigitated flow did not differ

much. Thus, the pressure drop under interdigitated flow came mainly from flow through the dense pore structure of the porous medium. At high current density, liquid water accumulated in the porous GDL during the serpentine flow mode, which resulted in reduced open pores. As the flow mode switched from serpentine to interdigitated, the pressure drop was initially high because of the high liquid water level in the GDL during the serpentine flow mode. As the air flowed through the GDL under interdigitated mode, the shear force purged part of the liquid water in the GDL leading to a lower saturation level and lower pressure drop. Third, it was seen that the cell voltage under the interdigitated mode was higher than that for the serpentine mode because of two advantageous aspects associated with the interdigitated flow mode: higher reactant pressure or concentration and fast convective transport of the oxygen reactant to the catalyst layer. Last, it was seen that the cell voltage under the serpentine mode became unstable at current density 0.89 A/cm^2 and higher because of excessive accumulated liquid water in the cathode GDL at high current densities. The voltage under the interdigitated flow mode was stable because the shear force due to air flow through the GDL effectively removed the liquid water accumulated in the GDL leading to better gas transport through the GDL.

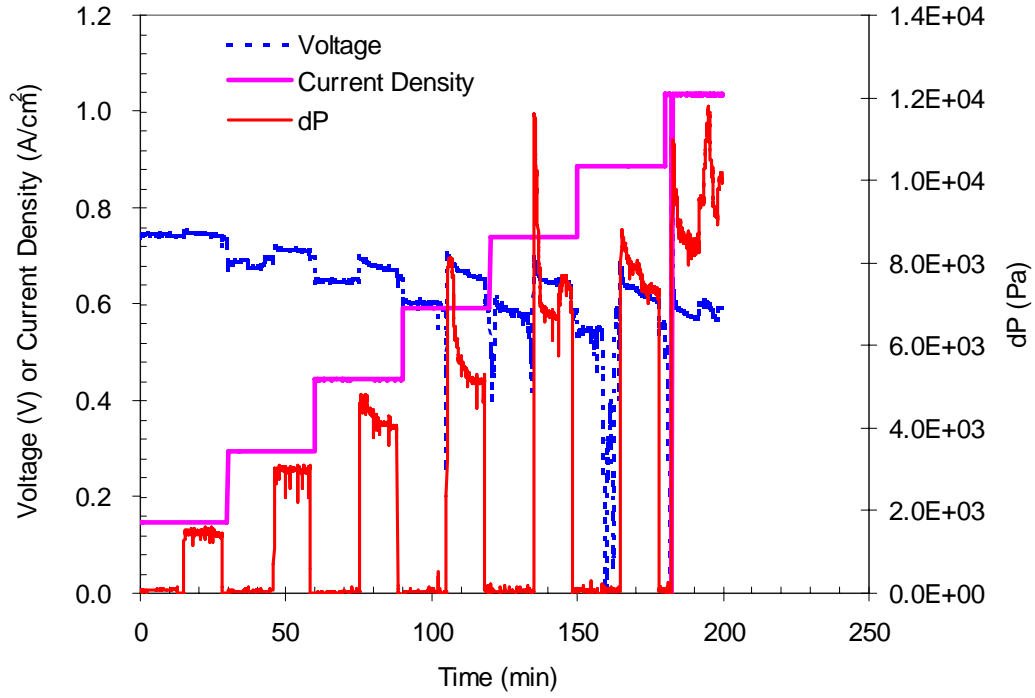


Figure 3.3 Voltage, current density, and pressure drop in the test of sample B1. Stoichiometry of A/C=2/4, temperature of $T_{\text{cell}}/T_A/T_C=70/70/70$ °C. A and C represent anode and cathode, respectively.

The fuel cell performance, pressure drop at the beginning and at the steady state of the interdigitated flow mode, and predicted saturation level corresponding to the pressure drop across sample B1 are shown in Fig. 3.4. First, the permeability was calculated based on the pressure drop between the air inlet and outlet. Second, the saturation level was calculated using Eqs. 3.3 and 3.4 after the permeability was calculated from the pressure drop.

The interdigitated flow mode showed better fuel cell performance because the

GDL under this mode had lower saturation level and higher transport rate of the reactant. The pressure drop increased with current density as expected because of higher gas flow rates. Saturation level displaced by the air flow under the interdigitated mode caused the difference in the pressure drop between the steady state and the beginning of the interdigitated mode. Saturation level at the beginning of the interdigitated mode represents the saturation level under the serpentine flow mode. Under the serpentine flow mode, the highest saturation level was reached in the current density range of 0.6 to 0.8 A/cm². Beyond 0.8 A/cm², the fuel cell became unstable, which resulted in failure of operation with the cell voltage dropping to 0.1V triggering the setup to immediately switch to the interdigitated flow. This explains why the predicted saturation level is lower under unstable conditions since the time under serpentine flow mode is much shorter. The scattered points in Fig. 3.4 represent the fuel cell voltage, saturation levels and pressure drops at unstable operation of the fuel cell.

The predicted saturation level under interdigitated flow mode was stable, because both the anode and cathode were saturated and the interdigitated flow was very effective in removing the liquid water from the GDL. At high current densities, the predicted saturation levels were even slightly lower than those at low current densities. This was caused by the increased air flow rate, which brought greater shear

force to displace the liquid water in the cathode.

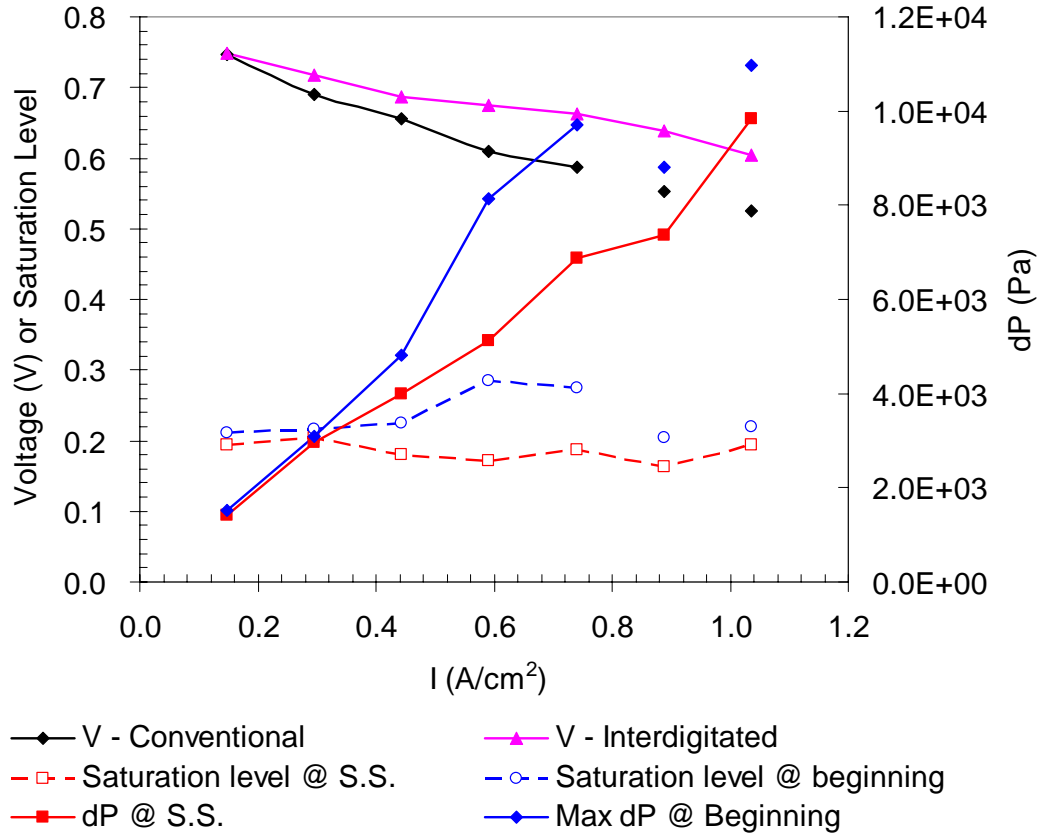


Figure 3.4 Fuel cell performance, pressure drop, and saturation level of material B1. Stoichiometry of $A/C=2/4$, temperature of $T_{\text{cell}}/T_A/T_C=70/70/70$ °C.

The voltage, current density, and pressure drop of sample B3 are presented in Fig. 3.5. Similar phenomena as those in the measurement of sample B1 were observed here. First, pressure drop under serpentine flow mode was stable and negligible. Under interdigitated flow mode, at low current density the pressure drop was stable because little liquid water was inside the GDL. The change in the pressure

drop between the beginning value and steady state value under interdigitated flow mode increased when the current density reached 0.60 A/cm^2 and higher. The pressure drop difference between the beginning and steady state represents the amount of liquid water displaced by the interdigitated flow air. Second, the fuel cell voltage under serpentine flow mode began to fluctuate at the current density of 1.04 A/cm^2 . At the current density of 1.18 A/cm^2 and higher, the fuel cell under serpentine flow mode failed because the high saturation level inside the GDL prevented the reactants from getting to the CL to support the electrochemical reaction.

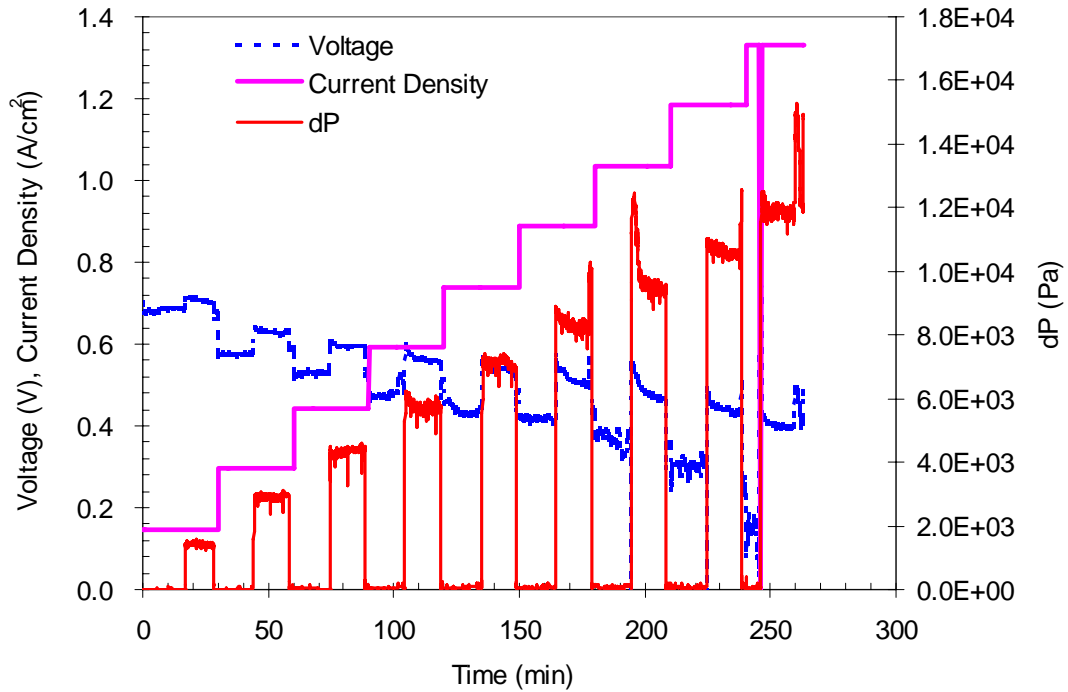


Figure 3.5 Voltage, current density, and pressure drop in the test of sample B3. Stoichiometry of $A/C=2/4$, temperature of $T_{\text{cell}}/T_A/T_C=70/70/70 \text{ } ^\circ\text{C}$.

Fig. 3.6 shows that better fuel cell performance was obtained with the interdigitated flow mode. As discussed in the previous part of this chapter, the higher reactant concentration under interdigitated flow mode led to better fuel cell performance. The fuel cell was unstable under serpentine flow mode, when the current density was 1.18 A/cm^2 and higher. The saturation level under serpentine flow mode was highest at current density of 1.04 A/cm^2 . The predicted saturation levels at higher current density were lower because the fuel cell failed before it reached steady state, which resulted in less liquid water accumulated inside the GDL. Under the interdigitated flow mode, the predicted saturation levels decreased slightly with the increase of the current density. This was caused by the increased flow rate at higher current density since the fuel cell was operated in galvanostatic and constant stoichiometric flow rate mode. The increased flow rate of the reactant removed more liquid water from the porous GDL. The difference of the pressure drop between the serpentine flow mode and the interdigitated flow mode was very small at low current densities since little liquid water existed inside the GDL. This difference became more apparent at higher current densities due to higher level of accumulated water in the cathode electrode.

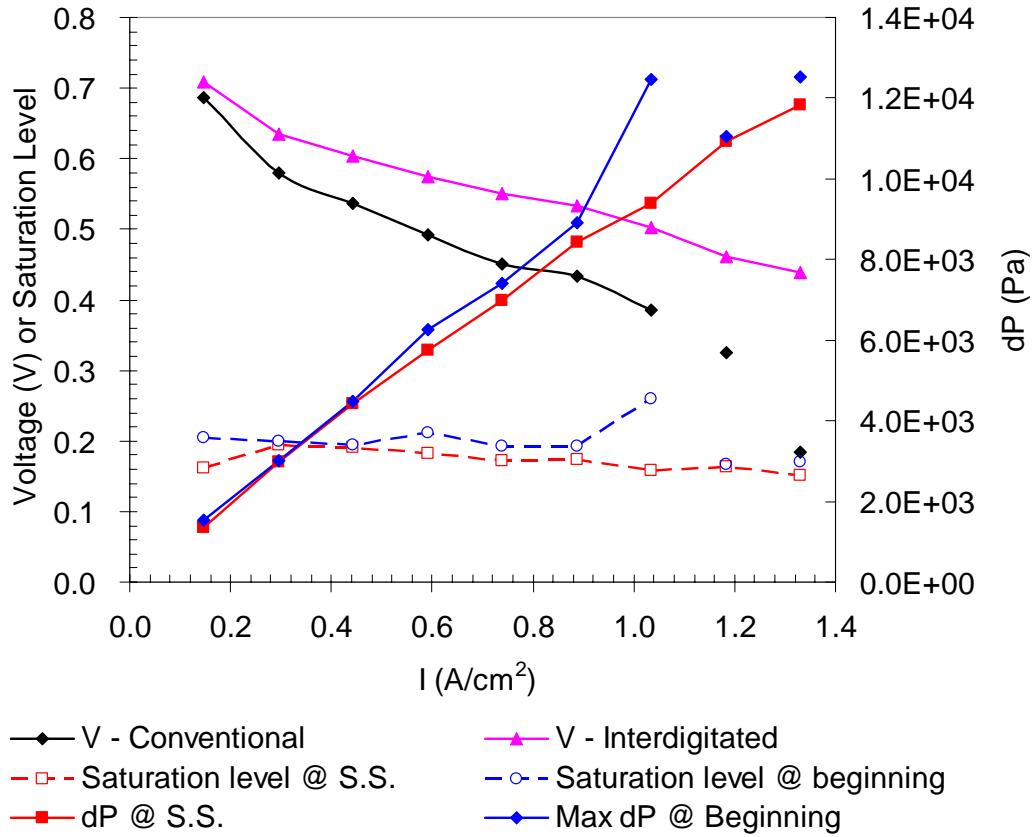


Figure 3.6 Fuel cell performance, pressure drop, and saturation level of material B3. Stoichiometry of A/C=2/4, temperature of $T_{\text{cell}}/T_A/T_C=70/70/70$ °C.

3.3.3 Stoichiometric Effect

The stoichiometric effect was investigated with a lower cathode flow rate while the other operating conditions were kept the same. Instead of a stoichiometry of 4 in the cathode side, a lower flow rate of stoichiometry 1.5 was used. Both MEAs consisted of B1 and B3 were tested under lower cathode air stoichiometry. Only the results of B1 were presented in this chapter for the purpose of brevity. The results of B3, although not shown here, showed similar characteristics to those of B1.

Fig. 3.7 shows that the cathode gas pressure drop under interdigitated flow decreased greatly when the cathode gas flow stoichiometry decreased from 4 to 1.5 (refer to Fig. 3.3). Voltage oscillation was observed when the current density was about 0.74 A/cm^2 because of excessive accumulated liquid water in the GDL. A large pressure drop was seen when the fuel cell switched from conventional flow to interdigitated flow at 0.74 A/cm^2 . As the liquid water was removed by the shear force of the gas phase, the associated pressure drop decreased gradually. More frequent oscillations were seen when the fuel cell was operating at higher current densities which resulted in more liquid water accumulated in the cathode porous media. This showed that the higher cathode gas flow stoichiometry was needed to achieve the stable fuel cell performance at higher current densities. However, higher cathode stoichiometry may result in higher parasitic energy loss. In practice, an optimal stoichiometry needs to be found.

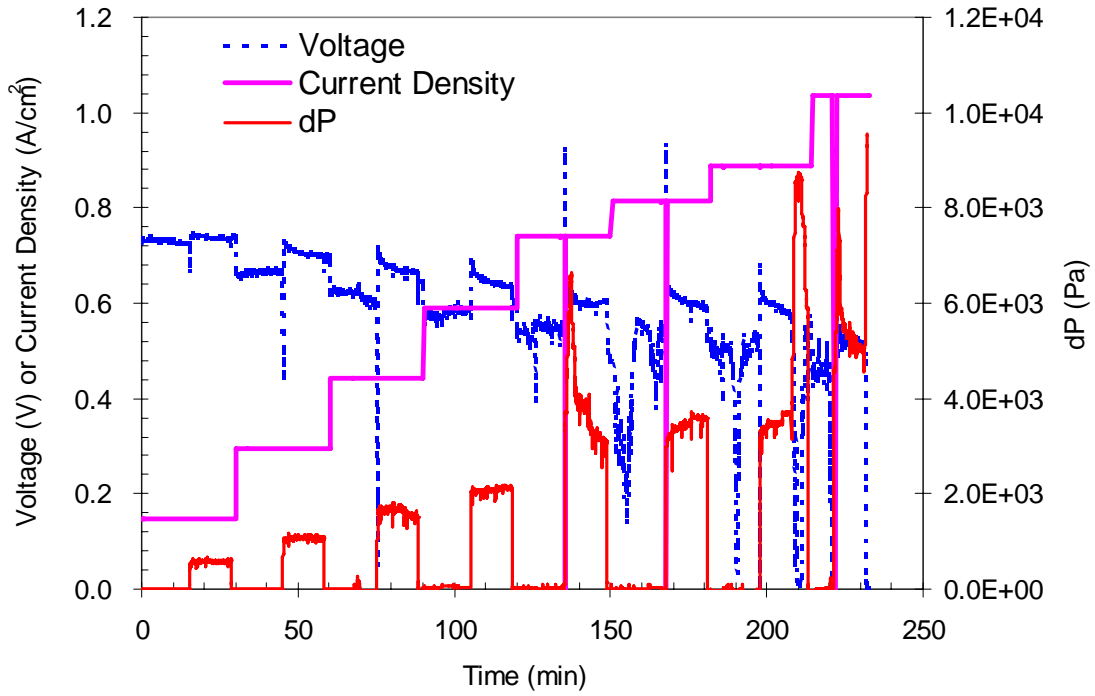


Figure 3.7 Voltage, current density, and pressure drop in the test of sample B1. Stoichiometry of A/C=2/1.5, temperature of $T_{\text{cell}}/T_A/T_C=70/70/70$ °C.

The fuel cell performances and pressure drops under conventional and interdigitated flow at low air stoichiometry are shown in Fig. 3.8. Under serpentine flow, the fuel cell performance was unstable at the current densities of 0.74 A/cm^2 and higher. This unstable point came earlier than when the fuel cell was operated with cathode stoichiometry of 4 (refer to Fig. 3.4).

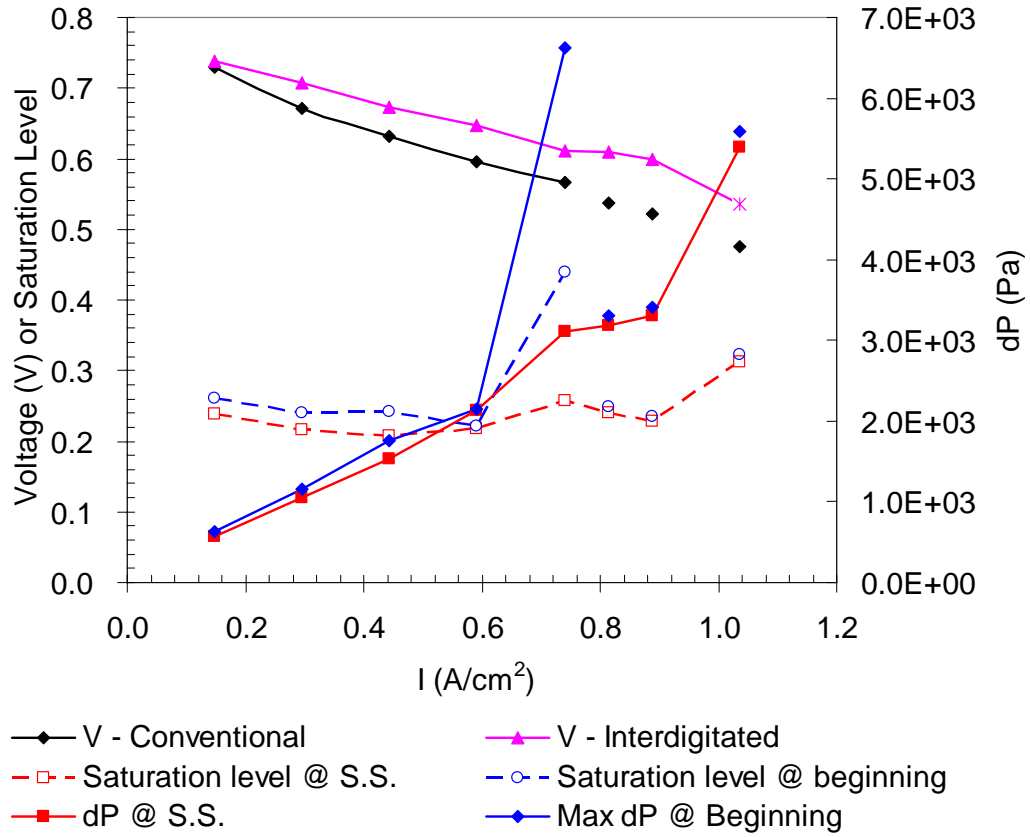


Figure 3.8 Fuel cell performance, pressure drop, and saturation level of material B1. Stoichiometry of A/C=2/1.5, temperature of $T_{\text{cell}}/T_A/T_C=70/70/70$ °C.

3.3.4 Temperature Effect

The temperature effects on the fuel cell performance and the cathode pressure drops are shown in Figs. 3.9 and 3.10. The temperature configuration was held at $T_{\text{cell}}/T_A/T_C=70/50/50$ °C. Since the cathode and anode humidifier temperature ($T_A/T_C=50/50$ °C) was lower than that of the fuel cell ($T_{\text{cell}}=70$ °C), evaporation in the cathode was expected, which alleviated the flooding effect in the cathode. The calculated liquid water saturation levels in Fig. 3.10 showed that lower saturation

levels existed in the GDL when the cathode was supplied with unsaturated gas. The pressure drop under interdigitated flow was more stable because of the reduced saturation levels. Better fuel cell performance was reflected by the stable operation at the current density of 0.74 A/cm^2 and higher as shown in Fig 3.10 (refer to Fig. 3.8). However, the anode side became subjected to dehydration, which could have led to poor fuel cell performance. Under this circumstance, the balance of a less flooded cathode and a dry anode determined the fuel cell performance.

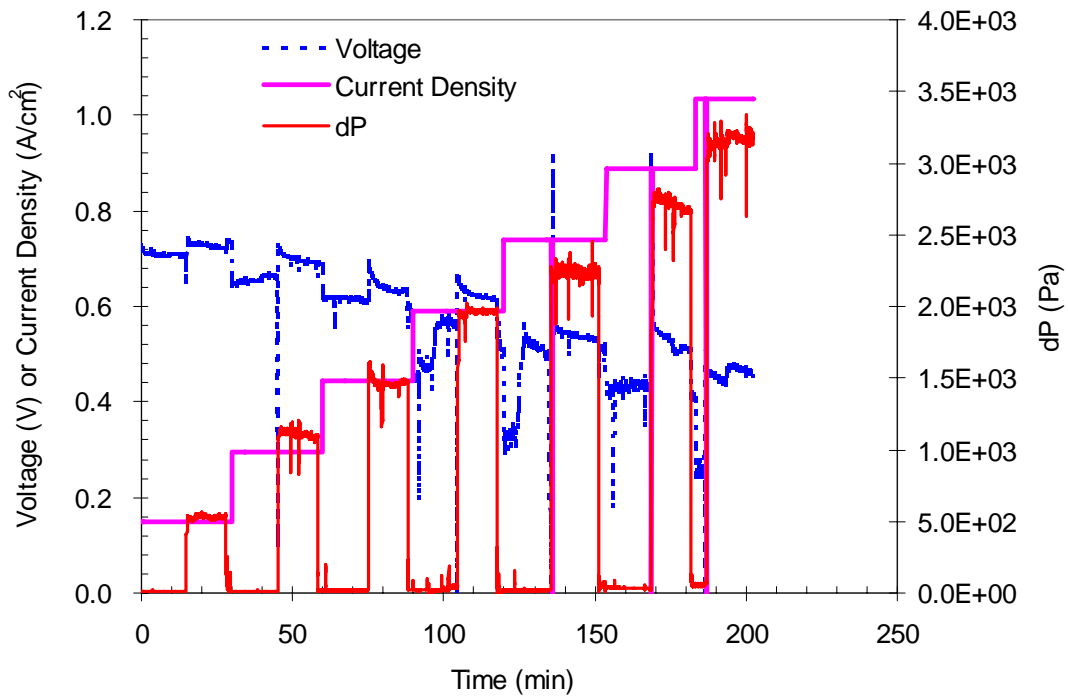


Figure 3.9 Voltage, current density, and pressure drop in the test of sample B1. Stoichiometry of A/C=2/1.5, temperature of $T_{\text{cell}}/T_A/T_C=70/50/50 \text{ }^\circ\text{C}$.

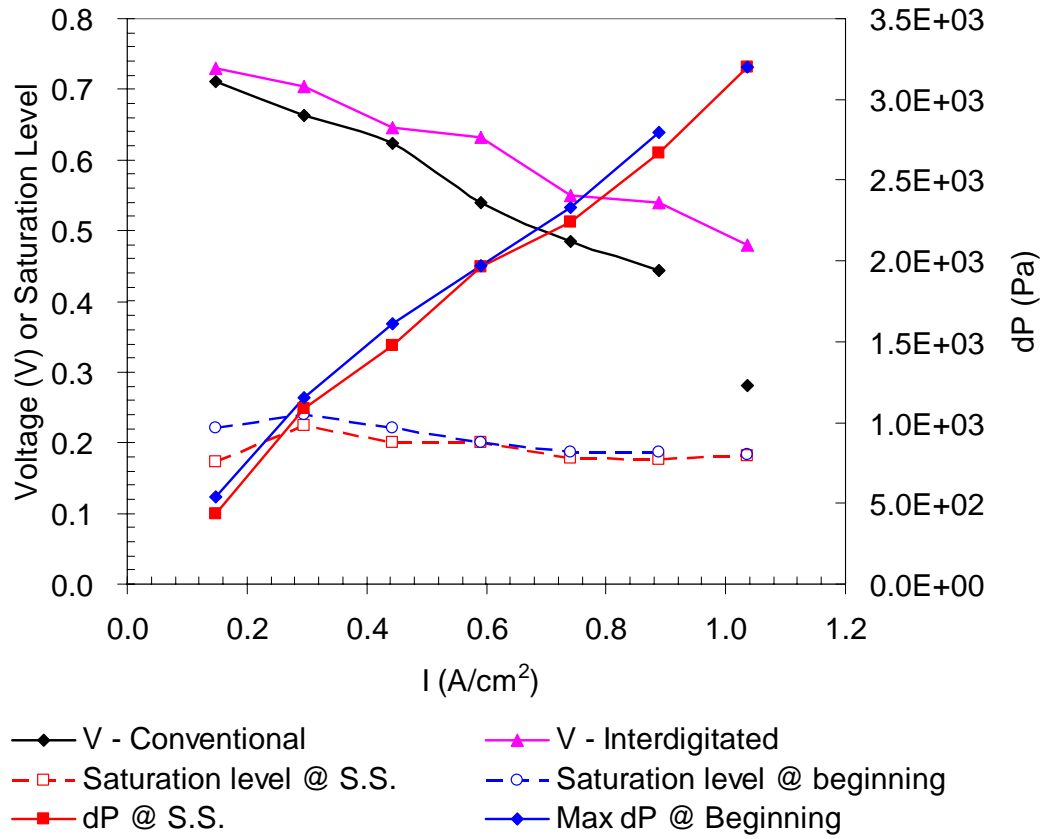


Figure 3.10 Fuel cell performance, pressure drop, and saturation level of material B1. Stoichiometry of A/C=2/1.5, temperature of $T_{\text{cell}}/T_A/T_C=70/50/50$ °C.

3.4 Conclusions

Liquid water saturation levels in the cathode side were quantitatively determined using the experimentally measured correlations of the relative permeability and saturation levels. By using a setup that can switch from the conventional serpentine flow to interdigitated flow, the liquid saturation levels in the cathode GDLs under the serpentine flow and interdigitated flow modes can be determined from the pressure

drop signals. The interdigitated flow led to better fuel cell performance than the conventional flow because it was more effective in removing liquid water in the porous media. Lower cathode stoichiometry led to unstable fuel cell performance at an earlier stage (lower current densities) because the gas phase is less capable of removing liquid water at lower gas flow rate. When the fuel cell was supplied with unsaturated gases, better fuel cell performance benefited from water removal by evaporation in the cathode side. However, when the anode side was unsaturated, membrane dehydration may limit the fuel cell performance.

3.5 References

1. M. F. Mathias, J. Roth, J. Fleming and W. Lehnert, Diffusion Media Materials and Characterisation. In *Handbook of Fuel Cells - Fundamentals, Technology and Applications*, W. Vielstich, H. A. Gasteiger and A. Lamm, Eds. John Wiley & Sons, Ltd.: Vol. 3: Fuel Cell Technology and Applications, pp 517, 2003.
2. X. Wang and T. V. Nguyen, Modeling the Effects of the Micro-Porous Layer on the Net Water Transport Rate Across the Membrane in a PEM Fuel Cell, *J. Electrochem. Soc.*, in press, **2010**.
3. K. Tuber, D. Pocza and C. Hebling, Visualization of Water Buildup in the Cathode of a Transparent PEM Fuel Cell, *J. Power Sources*, 124 (2), 403, **2003**.

4. F. Y. Zhang, X. G. Yang and C. Y. Wang, Liquid Water Removal from a Polymer Electrolyte Fuel Cell, *J. Electrochem. Soc.*, 153 (2), A225, **2006**.
5. K. W. Feindel, S. H. Bergens and R. E. Wasylshen, The Use of H-1 NMR Microscopy to Study Proton-Exchange Membrane Fuel Cells, *Chemphyschem*, 7 (1), 67, **2006**.
6. K. Teranishi, S. Tsushima and S. Hirai, Analysis of Water Transport in PEFCs by Magnetic Resonance Imaging Measurement, *J. Electrochem. Soc.*, 153 (4), A664, **2006**.
7. S. Tsushima, K. Teranishi and S. Hirai, Magnetic Resonance Imaging of the Water Distribution within a Polymer Electrolyte Membrane in Fuel Cells, *Electrochem. Solid-State Lett.*, 7 (9), A269, **2004**.
8. P. K. Sinha, P. Halleck and C.-Y. Wang, Quantification of Liquid Water Saturation in a PEM Fuel Cell Diffusion Medium Using X-ray Microtomography, *Electrochem. Solid-State Lett.*, 9 (7), A344, **2006**.
9. W. Zhu, Z. W. Dunbar and R. I. Masel, MicroCT X-ray Imaging of Water Movement in a PEM Fuel Cell, *ECS Trans.*, 16 (2), 995, **2008**.
10. A. B. Geiger, A. Tsukada, E. Lehmann, P. Vontobel, A. Wokaun and G. G. Scherer, In Situ Investigation of Two-Phase Flow Patterns in Flow Fields of PEFC's Using Neutron Radiography, *Fuel Cells*, 2 (2), 92, **2002**.

11. D. S. Hussey, D. L. Jacobson, M. Arif, J. P. Owejan, J. J. Gagliardo and T. A. Trabold, Neutron Images of the Through-Plane Water Distribution of an Operating PEM Fuel Cell, *J. Power Sources*, 172 (1), 225, **2007**.
12. T. Kim, J. Kim, C. Sim, S. Lee, M. Kaviany, S. Son and M. Kim, Experimental Approaches for Distribution and Behavior of Water in PEMFC under Flow Direction and Differential Pressure Using Neutron Imaging Technique, *Nucl Instrum Meth A*, 600 (1), 325, **2009**.
13. T. Kim, J. Kim, C. Sim, S. Lee, Y. Son and M. Kim, Experimental Approaches for Water Discharge Characteristics in PEMFC Using Neutron Imaging Technique at Conrad, HMI, *Nucl Eng Technol*, 41 (1), 135, **2009**.
14. R. Satija, D. L. Jacobson, M. Arif and S. A. Werner, In Situ Neutron Imaging Technique for Evaluation of Water Management Systems in Operating PEM Fuel Cells, *J. Power Sources*, 129 (2), 238, **2004**.
15. W. He, G. Lin and T. V. Nguyen, Diagnostic Tool to Detect Electrode Flooding in Proton-Exchange-Membrane Fuel Cells, *AIChE J.*, 49 (12), 3221, **2003**.
16. W. He, J. S. Yi and T. V. Nguyen, Two-Phase Flow Model of the Cathode of PEM Fuel Cells Using Interdigitated Flow Fields, *AIChE J.*, 46 (10), 2053, **2000**.
17. G. Lin, W. He and T. V. Nguyen, Modeling Liquid Water Effects in the Gas Diffusion and Catalyst Layers of the Cathode of a PEM Fuel Cell, *J. Electrochem.*

- Soc.*, 151 (12), A1999, **2004**.
18. D. Natarajan and T. V. Nguyen, A Two-Dimensional, Two-Phase, Multicomponent, Transient Model for the Cathode of a Proton Exchange Membrane Fuel Cell Using Conventional Gas Distributors, *J. Electrochem. Soc.*, 148 (12), A1324, **2001**.
 19. U. Pasaogullari, C.-Y. Wang and K. S. Chen, Two-Phase Transport in Polymer Electrolyte Fuel Cells with Bilayer Cathode Gas Diffusion Media, *J. Electrochem. Soc.*, 152 (8), A1574, **2005**.
 20. A. Z. Weber, R. M. Darling and J. Newman, Modeling Two-Phase Behavior in PEFCs, *J. Electrochem. Soc.*, 151 (10), A1715, **2004**.
 21. Q. Ye and T. V. Nguyen, Three-Dimensional Simulation of Liquid Water Distribution in a PEMFC with Experimentally Measured Capillary Functions, *J. Electrochem. Soc.*, 154 (12), B1242, **2007**.
 22. M. Kaviany, *Principles of Heat Transfer in Porous Media*, 2nd ed.; Springer-Verlag: New York, p 708, 1995.
 23. H. Yamada, T. Hatanaka, H. Murata and Y. Morimoto, Measurement of Flooding in Gas Diffusion Layers of Polymer Electrolyte Fuel Cells with Conventional Flow Field, *J. Electrochem. Soc.*, 153 (9), A1748, **2006**.
 24. V. Gurau, M. J. Bluemle, E. S. De Castro, Y.-M. Tsou, T. A. Zawodzinski Jr. and J.

- A. Mann Jr, Characterization of Transport Properties in Gas Diffusion Layers for Proton Exchange Membrane Fuel Cells 2. Absolute Permeability, *J. Power Sources*, 165 (2), 793, **2007**.
25. J. Itonen, M. Mikkola and G. Lindbergh, Flooding of Gas Diffusion Backing in PEFCs - Physical and Electrochemical Characterization, *J. Electrochem. Soc.*, 151 (8), A1152, **2004**.
26. M. V. Williams, E. Begg, L. Bonville, H. R. Kunz and J. M. Fenton, Characterization of Gas Diffusion Layers for PEMFC, *J. Electrochem. Soc.*, 151 (8), A1173, **2004**.

Chapter 4

Modeling the Effects of Capillary Property of Porous Media on the Performance of the Cathode of a PEM Fuel Cell

4.1 Background

As discussed in Chapter 2 and Chapter 3, the removal rate of water, which determines the liquid water saturation levels in the GDL and CL, depends on the two-phase transport properties of these porous materials. The CL is hydrophilic because of the presence of a highly hydrophilic ionic (Nafion) phase. The GDL is, however, partly hydrophilic and partly hydrophobic - in part because of the presence of a waterproof material such as PTFE. In order to model the two-phase transport phenomena in a PEM fuel cell accurately, transport properties of the GDL and CL used are needed. However, due to the lack of two-phase transport property data for these materials, many previous models had resorted to other techniques such as 1) assuming a constant slope capillary curve,^{1, 2} 2) extracting capillary data from fuel cell performance,³ and 3) using capillary data based on Udell's correlation for sand packs.⁴⁻⁸

The capillary force changes with the liquid saturation level in the porous material. A fixed slope capillary function only represents one point, instead of the

whole range of the curve. Extracting the capillary function from the fuel cell performance may attribute the influences of other parameters to the capillary function. Udell's correlation of Leverett function was developed for sand, while the porous materials used in PEM fuel cells exhibit different capillary pressure properties.

In some studies, the GDL and CL were treated as hydrophobic and hydrophilic materials, respectively, by using different $J(s)$ functions in the Leverett expression of the capillary pressure functions, without accounting for the force balance at the GDL/CL interface.⁵⁻⁷ This approach resulted in a smooth saturation level profile across the GDL and CL interface. This treatment did not include the interaction of the capillary effects of the CL and the GDL. Recent experimental data show that the carbon fiber GDL used in PEM fuel cells exhibit both hydrophobic and hydrophilic properties.⁹⁻¹² We will show here that in a fuel cell operation, the interaction of the capillary properties of the GDL and CL at the GDL/CL interface plays an important role in the liquid water transport in the porous media. The interaction of the CL and GDL capillary pressures will be discussed further in the following part of this chapter. Recently, Ye and Nguyen¹³ provided a 3-D model of a PEM fuel cell using the experimentally determined capillary functions of the GDL and CL materials. However, the effect of porous materials with dissimilar capillary pressure property in contact was not included.

In this chapter, we will discuss 1) the capillary interactions of the CL and GDL; 2) various aspects (shape, magnitude, range of saturation level and slope) of the capillary curves in the two-phase model; 3) the effects of capillary functions on the liquid accumulation level in the porous media and its effects on the fuel cell performance.

4.2 Capillary Functions

Capillary pressure is typically defined as

$$p_c = p_g - p_l \quad [4.1]$$

where p_c is capillary pressure, p_g is gas phase pressure, and p_l is liquid phase pressure. Fig. 4.1 shows typical capillary pressure curves of a carbon fiber GDL and a more hydrophilic CL. The capillary force balance at the GDL/CL interface requires

$$p_c|_{GDL} = p_c|_{CL} \quad [4.2]$$

The CL of a PEM fuel cell is more hydrophilic because of the existence of an ionic polymer (Nafion) phase. From Fig. 4.1, one can see that due to the constraint of capillary force balance, which is shown by Eq. 4.2, different saturation levels at the GDL/CL interface, or the saturation jump conditions, occur at that interface. This shows that introducing a GDL with different capillary property into the model without considering this saturation level jump condition is wrong. Furthermore, if a completely hydrophilic CL were used in a PEM fuel cell, this would lead to a flooded

CL.

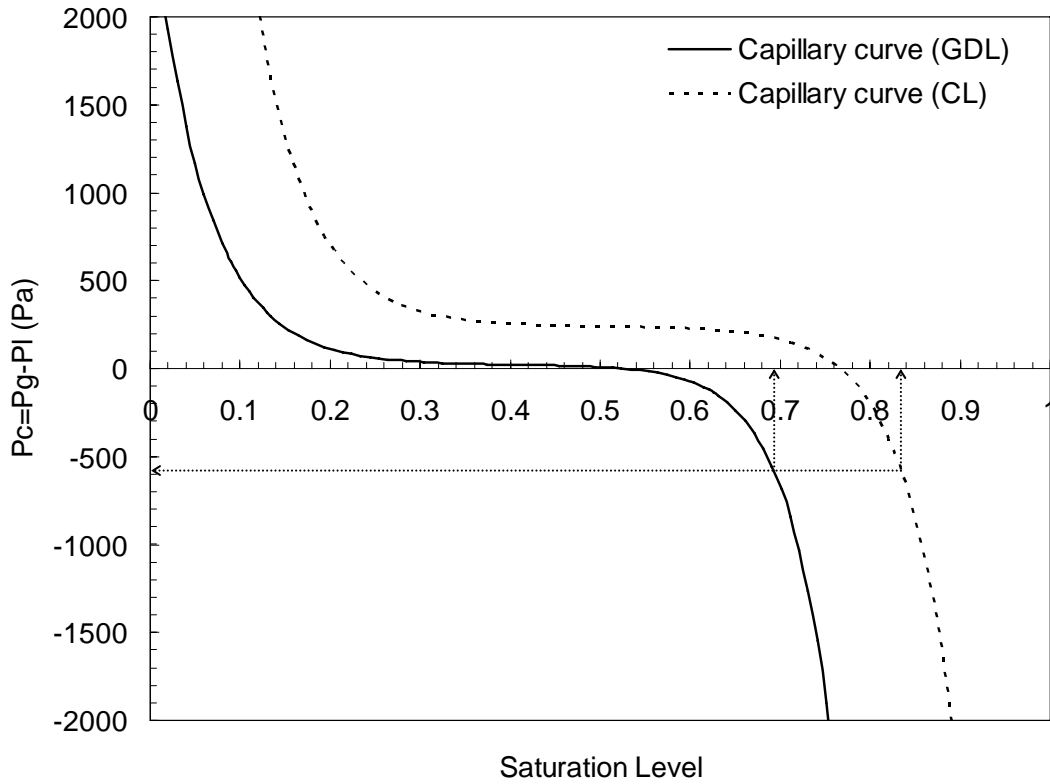


Figure 4.1 Comparison of capillary pressure of materials with different capillary properties.

To experimentally demonstrate the liquid saturation level jump, a bed filled with the hydrophilic glass beads and the hydrophobic acrylic beads was created. See Fig. 4.2. It clearly shows that the hydrophilic glass beads have higher liquid saturation level than the less hydrophilic acrylic beads. This liquid water saturation level jump condition is created when two media with different capillary pressure properties are

placed in contact. The saturation jump condition is not a step function in Fig. 4.2 because it is a diffused interface formed from two relative coarse porous media. As the surface roughness decreases the diffused interface approaches a sharp jump interface. Fig. 4.2 is used to illustrate the jump condition and is not supposed to be representative of the actual jump condition of porous media used in PEM fuel cells.

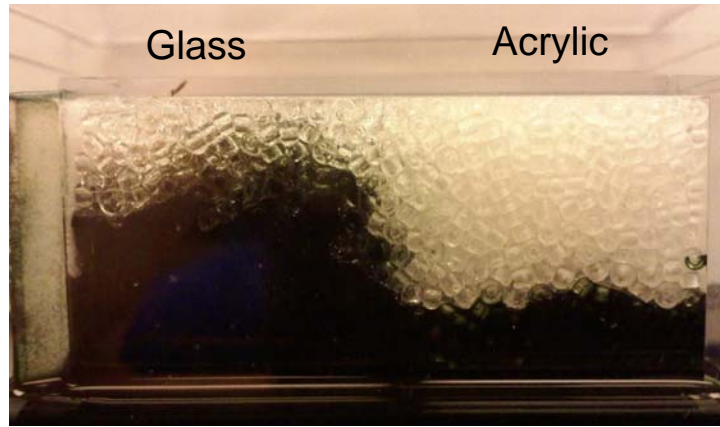


Figure 4.2 Liquid saturation level jump condition at two materials with different wetting properties (by Clint D. Frye, an undergraduate student in our group).

Fig. 4.3 shows an experimentally determined capillary curve of a commercially available GDL in literature.⁹ For the convenience of use in the modeling, the fitted correlation is of the form¹³

$$p_c = d \left[e^{-a_1(s-c)} - e^{a_2(s-c)} \right] + b \quad [4.3]$$

In Eq. 4.3, s is the saturation level, and a_1 , a_2 , b , c and d are fitting parameters.

Capillary properties of the gas diffusion materials used in a PEM fuel cell are

recently available in literature.^{9, 10, 14-19} However, the capillary curves vary significantly with different measurement methods used in the experiments. Experimental capillary curves of the MPL and CL are not available in the literature due to the difficulty of testing those thin materials. These curves in Fig. 4.3 are chosen according to the criteria that the CL is most hydrophilic and the GDL is more hydrophobic than the CL because of the existence of the hydrophilic Nafion phase in the CL and hydrophobic PTFE in the GDL. The experimentally measured capillary curve of a commercial GDL (Toray 090 at 10 %wt wet proof) was used in this model.⁹ The capillary pressure in Fig. 4.3 is expressed as $p_c = p_g - p_l$, which is opposite to the capillary pressure definition shown in reference 9. Our group's data are consistent with the imbibition curve in Fairweather *et al.*'s reports.¹⁰⁻¹² The capillary curve of the CL has a steep slope in the hydrophobic region because of the addition of a hydrophobic phase PTFE. It was recognized very early by our group that the presence of the hydrophobic GDL might result in higher liquid water saturation level in the CL. To avoid flooding the cathode CL, we have been investigating the addition of hydrophobic PTFE nano particles to the CL to create continuous gas transport channels or pathways in the CL. These continuous gas channels allow gas transport through the CL even at very high liquid saturation level. Recent results have shown that adding PTFE to the CL led to higher fuel cell performance and the PTFE content

can be as high as 27 %wt.²⁰ Note that with such high PTFE content in a CL it is hard to fully saturate the CL unless very high capillary pressure is used.

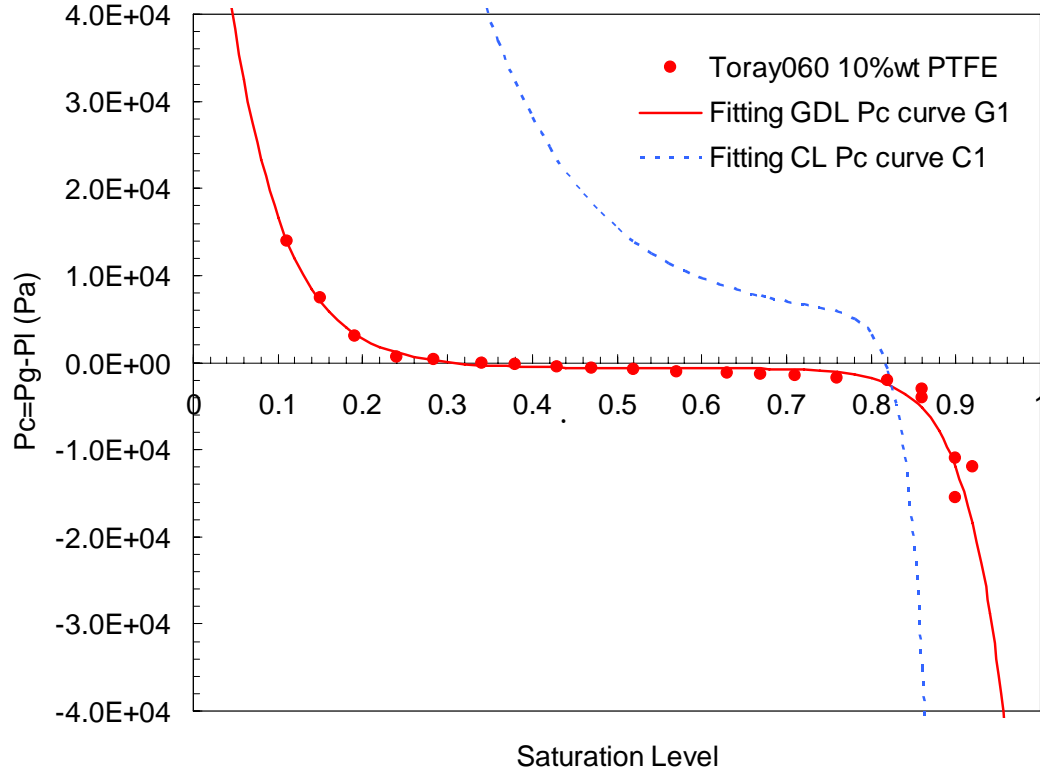


Figure 4.3 Experimentally determined capillary pressure of a GDL (Toray 060) and a fitted capillary curve of a CL.

The capillary pressure correlates to the properties of porous materials as follows²¹

$$p_c = \sigma \cos \theta \left(\frac{\varepsilon}{K} \right)^{1/2} J(s) \quad [4.4]$$

where σ is the gas-liquid surface tension, θ is the contact angle, ε is the porosity, K is the absolute permeability, and $J(s)$ is the Leverett function. Eq. 4.4

shows that capillary pressure may be modified by the change of one or more of those parameters. From this point of view, the curves plotted in Fig. 4.4 are reasonable as long as the material properties are modified appropriately. The modification of porous medium properties is usually carried out by changing the fraction of the hydrophobic phase Teflon in the material. The material structure may also play an important role in changing the capillary pressure properties.

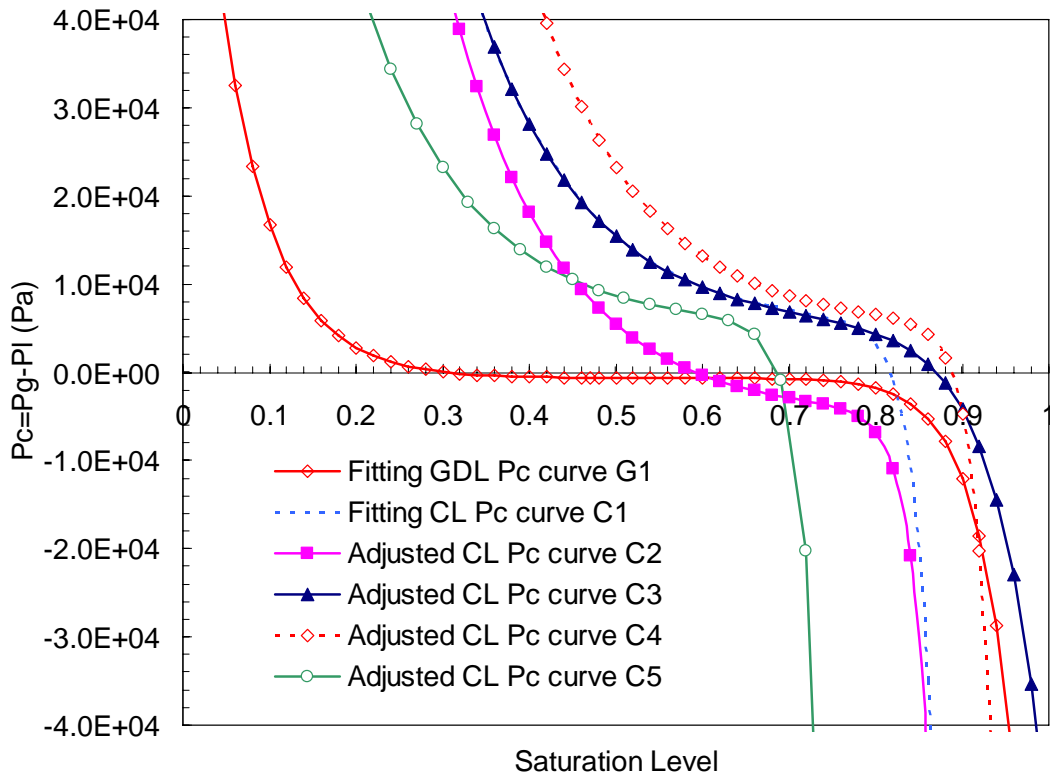


Figure 4.4 Adjusted capillary functions of CL.

In Fig. 4.4, curves G1 and C1 are fitted capillary pressure curves from Fig. 4.3.

For comparison, curves G1 and C1 are plotted together with the adjusted CL capillary curves in Fig. 4.4. The adjusted CL curves were obtained by adjusting curve C1 as follows:

C2 = C1 shifted downward (less hydrophilic);

C3 = C1 with lower slope in the hydrophobic region (more hydrophilic);

C4 = C1 shifted to the right (more hydrophilic);

C5 = C1 shifted to the left. (less hydrophilic).

These changes were selected to study how the shape, slope, magnitude and saturation range of the GDL and CL affect the liquid water transport rate out of the cathode, the liquid saturation level in the GDL and CL, and consequently, the performance of the cathode in a PEM fuel cell.

In Fig. 4.5, the experimentally determined curve for the GDL, G1, is also plotted for comparison. Curve C1 is the fitted CL capillary function shown in Fig. 4.3. The other curves, G2, G3, G4 and G5, are adjusted GDL capillary curves obtained as follows:

G2 = G1 shifted downward (less hydrophilic);

G3 = G1 with steeper slope in the hydrophobic region (less hydrophilic);

G4 = G1 with lower slope in the hydrophobic region (more hydrophilic);

G5 = G1 shifted to the left (less hydrophilic).

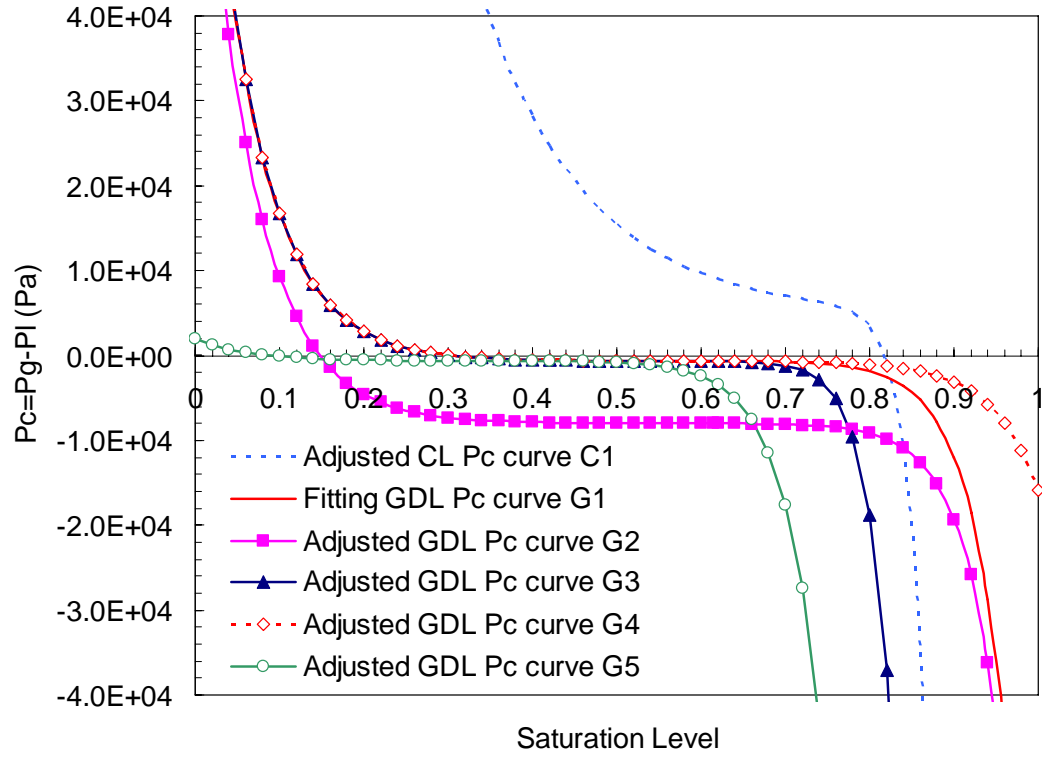


Figure 4.5 Adjusted capillary functions of GDL.

The parameters in Eq. 4.3 of the capillary functions shown in Figs. 4.4 and 4.5 are summarized in Table 1. The model development is discussed next.²²

Table 4.1 Parameters of the capillary functions.

| Capillary functions | a1, a2, b (Pa), c, d (Pa) |
|---------------------|---------------------------------------|
| Fig. 4.4 | |
| G1 | -22.69, -16.19, -644.86, 0.578, -7.59 |
| C1 | -45.0, -8.0, 5000.0, 0.78, -1106.56 |
| C2 | -45.0, -8.0, -5000.0, 0.78, -1106.56 |
| C3 | -18.0, -8.0, 5000.0, 0.78, -1106.56 |
| C4 | -45.0, -8.0, 5000.0, 0.85, -1106.56 |
| C5 | -45.0, -8.0, 5000.0, 0.65, -1106.56 |
| Fig. 4.5 | |
| G2 | -22.69, -16.19, -8000.0, 0.578, -7.59 |
| G3 | -35.0, -16.19, -644.86, 0.578, -7.59 |
| G4 | -18.0, -16.19, -644.86, 0.578, -7.59 |
| G5 | -22.69, -16.19, -644.86, 0.36, -7.59 |

4.3 Model Development

A 1-D, steady state, two-phase mass transport model for the cathode side of a PEM fuel cell is developed. The modeled domain is shown in Fig. 4.6. The modeled region consists of a gas diffusion layer, a catalyst layer and a membrane. The reactant, which is oxygen, diffuses from the channel into the porous media and reacts in the catalyst layer to produce liquid water.

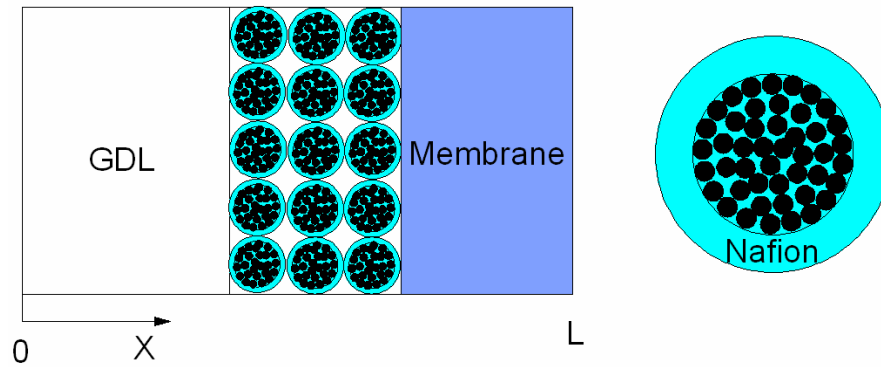


Figure 4.6 Schematic diagram of the modeled domain.

4.3.1 Assumptions

The model has the following assumptions:¹

- 1) Steady state, isothermal, and isobaric process;
- 2) Ideal gases;
- 3) Fully saturated ionic Nafion phase in the CL;
- 4) Uniform catalyst pellet size and property and uniform Nafion film thickness on the pellets;
- 5) Membrane is impermeable to gaseous species;
- 6) The water generated by reaction and existing in the membrane phase is in liquid form;
- 7) The electronic conduction of the GDL and CL is so high that we can neglect their electronic resistances;
- 8) The overpotential of hydrogen oxidation at the anode is negligible.

4.3.2 Governing Equations

There are six variables that need to be solved:

- 1) The oxygen gas concentration, $C_{O_2}^g$;
- 2) The water vapor concentration, C_v^g ;
- 3) The ionic potential, ϕ_+ ;
- 4) The liquid water saturation level in the GDL, s_{GDL} ;
- 5) The liquid water saturation level in the CL, s_{CL} ;
- 6) The concentration of water in the ionic phase, C_w^N .

The governing equations are summarized in Table 4.2.

Table 4.2 Governing equations.

| Variables | GDL | CL | MEM |
|-------------|----------------------------------|------------------------------------------------|--------------------------|
| $C_{O_2}^g$ | $-\frac{dN_{O_2}^g}{dx} = 0$ | $-\frac{dN_{O_2}^g}{dx} - R_{O_2} = 0$ | $C_{O_2}^g = 0$ |
| C_v^g | $-\frac{dN_v^g}{dx} - R_w^c = 0$ | $-\frac{dN_v^g}{dx} - R_w^c = 0$ | $C_v^g = 0$ |
| ϕ_+ | N/A | $-\frac{di_+}{dx} - 4FR_{O_2} = 0$ | $-\frac{di_+}{dx} = 0$ |
| s_{GDL} | $-\frac{dN_w}{dx} + R_w^c = 0$ | N/A | N/A |
| s_{CL} | N/A | $-\frac{dN_w}{dx} + (4n + 2)R_{O_2} + R_w = 0$ | N/A |
| C_w^N | N/A | $-\frac{dC_w^N}{dx} = 0$ | $-\frac{dC_w^N}{dx} = 0$ |

The flux terms N_i^g (i denotes the O₂ or vapor) and N_w are expressed by

$$N_i^g = -D_i^{g,eff} \frac{dC_i}{dx} \quad [4.5]$$

$$N_w = C_w v = \frac{\rho_w}{M_w} \left(-\frac{K_w(s)}{\mu_w} \frac{dp_l}{dx} \right) \quad [4.6]$$

The gas effective diffusion coefficient, $D_i^{g,eff}$, is calculated using the Bruggeman correction.²³ It is also corrected for the existence of liquid water inside the porous media

$$D_i^{g,eff} = D_i^g [\varepsilon_i (1-s)]^{1.5} \quad [4.7]$$

The permeability dependence on the liquid water saturation level is accounted for by¹³

$$K_w(s) = K_{w,0} s^{4.5} \quad [4.8]$$

Substituting Eqs. 4.1 and 4.8 into Eq. 4.6 yields the flux expression for liquid as

$$N_w = \frac{\rho_w K_{w,0}}{M_w \mu_w} s^{4.5} \frac{\partial p_c}{\partial x} = \frac{\rho_w K_{w,0}}{M_w \mu_w} \frac{\partial p_c}{\partial s} s^{4.5} \frac{\partial s}{\partial x} \quad [4.9]$$

As addressed in previous works,^{13, 24} the pre-parameters of the saturation gradient are grouped together and the capillary diffusion coefficient, D_c , is defined as

$$D_c = -\frac{K_{w,0}}{\mu_w} \frac{\partial p_c}{\partial s} s^{4.5} \quad [4.10]$$

Then Eq. 4.9 may be rewritten as

$$N_w = -D_c \frac{\rho_w}{M_w} \frac{\partial s}{\partial x} \quad [4.11]$$

where D_c may be determined by the liquid relative permeability and capillary function correlations. The value of D_c indicates the transport capability of liquid water in a porous medium.

As addressed in previous models,^{1,3} the phase change reaction R_w^c is expressed by

$$R_w^c = k_c \frac{\varepsilon_i (1-s) y_v}{RT} (y_v P - P_v^{sat}) q + k_v \frac{\varepsilon_i s \rho_w}{M_w} (y_v P - P_v^{sat}) (1-q) \quad [4.12]$$

where

$$q = \frac{1 + \frac{|(y_v P - P_v^{sat})|}{(y_v P - P_v^{sat})}}{2} \quad [4.13]$$

and k_c is the condensation rate constant, k_v is the evaporation rate constant, y_v is the mole fraction of water vapor; ρ_w is the density of liquid water; and M_w is the molecular weight of water.

In the catalyst layer, the oxygen reduction rate within the catalyst pellet is derived using the Thiele modulus approach.^{1,25} The detailed steps are presented in reference 1. Note that in this model spherical pellets are assumed instead of cylindrical pellets. The Nafion phase and water film on the catalyst pellets are assumed to be very thin to allow their effects on the agglomerate radius and outer surface area to be neglected

$$R_{O_2} = \frac{\frac{RT}{H_{O_2}^N}}{\frac{\delta_N}{\alpha_r D_{O_2}^N} + \frac{\delta_w}{\alpha_r D_{O_2}^w} \frac{H_{O_2}^w}{H_{O_2}^N} + \frac{1}{\xi k_T}} C_{O_2}^g \quad [4.14]$$

The outer surface area of the spherical pellets per unit catalyst volume, α_r , is calculated by

$$\alpha_r = \frac{4\pi r^2}{\frac{4}{3}\pi r^3 / (1 - \varepsilon_{CL})} = \frac{3}{r} (1 - \varepsilon_{CL}) \quad [4.15]$$

The water film thickness is a function of the saturation in the CL and is calculated by

$$\delta_w = \frac{\varepsilon_{CL} s_C}{a_r} \quad [4.16]$$

The reaction rate constant k_T is expressed by

$$k_T = (1 - \varepsilon_{CL}) \frac{1}{4FC_{O_2,ref}} a_{Pt}^{agg} i_0 \exp \left[-\frac{\alpha_c F}{RT} (V_A - \phi_+ - U_{ref}) \right] \quad [4.17]$$

where $a_{Pt}^{agg} = \frac{a_{Pt} m_{Pt}}{\delta_{CL} (1 - \varepsilon_{CL})}$ is the active catalyst surface area per unit volume of agglomerates; a_{Pt} is the surface area per unit mass of Pt; m_{Pt} is the catalyst loading of the electrode; and δ_{CL} is the thickness of the catalyst layer. This approach allows the effect of the catalyst morphological properties to be modeled.

For spherical pellets, the effectiveness factor is expressed by ²⁵

$$\xi = \frac{1}{\varphi} \frac{(3\varphi) \coth(3\varphi) - 1}{(3\varphi)} \quad [4.18]$$

where the modulus is

$$\phi = \text{modulus} = \frac{r}{3} \sqrt{\frac{k_p}{D_{O_2}^{N,eff}}} = \frac{r}{3} \sqrt{\frac{k_T / (1 - \varepsilon_{CL})}{D_{O_2}^{N,eff}}} \quad [4.19]$$

In the membrane, the water flux N_w^N consists of the concentration gradient and electro-osmotic drag driven transport terms

$$N_w^N = \frac{i_+}{F} n - D_w^N \frac{dC_w^N}{dx} \quad [4.20]$$

where i_+ is expressed by

$$i_+ = -k_N \frac{d\phi_+}{dx} \quad [4.21]$$

4.3.3 Boundary Equations

Table 4.3 lists the boundary conditions. The position at $x=0$ is the channel/GDL interface, and $x=L$ denotes the membrane/anode interface as shown in Fig. 4.6. At the GDL/CL interface, the GDL and CL capillary pressures are set equal. This is in order to capture the jump in the liquid saturation level occurring at the interface of two materials with different wetting properties. Note that previous works had incorrectly used the saturation continuity, instead of the pressure continuity, at this interface. Consequently, the saturation levels predicted for the porous media in the PEM fuel cell were incorrect, leading to incorrect predictions of the fuel cell performance. The expressions of the capillary functions are fitted from the experimental data,⁹ or those adjusted, based on those that were experimentally determined.

Table 4.3 Boundary conditions.

| Variables | x=0 | GDL/CL | CL/MEM | x=L |
|-------------|-----------------------------|--------------------------------------|--------------------------------------------------|---------------------------------------|
| $C_{O_2}^g$ | $C_{O_2}^g = C_{O_2}^{air}$ | $N_{O_2}^g _{GDL} = N_{O_2}^g _{CL}$ | $N_{O_2}^g _{CL} = 0$ | $C_{O_2}^g = 0$ |
| C_v^g | $C_v^g = C_v^{g,air}$ | $N_v^g _{GDL} = N_v^g _{CL}$ | $N_v^g _{CL} = 0$ | $C_v^g = 0$ |
| ϕ_+ | N/A | $i_+ _{CL} = 0$ | $i_+ _{CL} = i_+ _{MEM}$ | $\phi_+ = 0$ |
| s_{GDL} | $p_c(s) = 0$ | $N_w _{GDL} = N_w _{CL}$ | N/A | N/A |
| s_{CL} | N/A | $p_c _{GDL} = p_c _{CL}$ | $N_w _{CL} = N_w^{N,concentration\ part} _{MEM}$ | N/A |
| C_w^N | N/A | $N_w^N _{CL} = 0$ | $C_w^N = C_{w,(\alpha)}^{N,eq,cathode}$ | $C_w^N = C_{w,(\alpha)}^{N,eq,anode}$ |

Note that at the gas channel/GDL interface, the capillary pressure is set to zero ($p_l=p_g$) when the feeding gas is saturated air.²⁶ In this model, the gas pressure is assumed to be constant in the porous media. Since liquid water transport from the catalyst layer to the gas channel is driven by a gradient of liquid water pressure from high pressure to low pressure, the liquid pressure inside the porous media is always greater than that at the channel/GDL interface. Based on the definition of capillary pressure used in Eq. 4.1, with $p_l=p_g$ set at the channel/GDL interface, the capillary pressure in the porous media in the cathode is always negative and corresponds to the hydrophobic region of the capillary pressure curve. Thus, the boundary condition $p_l=p_g$ limits the liquid water transport in the porous media to the hydrophobic region of the capillary curve (see Fig. 4.1). By the capillary force balance at the GDL/CL interface liquid water transport in the CL is also bound to the hydrophobic region. For non-saturated air, the saturation level can be set to zero at this interface if the evaporation rate is assumed to be so fast that all liquid water evaporates into the gaseous phase.

At the CL/MEM interface, an assumption was made that only water transport by concentration gradient driven diffusion occurs. Also, it was assumed that water transport by the electro-osmotic drag part of the flux is released inside the CL as the oxygen reduction reaction occurs. To simplify the problem, the anode and cathode

gaseous concentrations were fixed at the inlet. When the air and hydrogen gases are saturated with water vapor, the membrane is fully saturated on both the cathode and anode sides of the membrane. Thus, there is no concentration gradient of water inside the membrane, and Eq. 4.20 will be simplified to

$$N_w^N = \frac{i_+}{F} n \quad [4.22]$$

The equilibrium content of liquid water in the membrane is determined by²⁷

$$C_w^{N,eq} = C_f \left(0.043 + 17.81\alpha_v - 39.85\alpha_v^2 + 36.0\alpha_v^3 \right) \quad [4.23]$$

where C_f is the fixed charge site concentration, and α_v is the activity of water vapor in the gas phase.

Tables 4.4 and 4.5 list the correlations and parameters used in the simulation, and Table 4.6 lists the simulation conditions.

Table 4.4 Correlations used in the model.

$$D_{O_2}^g = 0.181 \left(\frac{T}{273.15} \right)^{1.823}, \text{ cm}^2/\text{s}^{28}$$

$$D_{O_2}^w = 7.4 \times 10^{-8} \frac{T(\psi_{H_2O} M_{H_2O})^{0.5}}{\mu_w V_{O_2}^{0.6}}, \text{ cm}^2/\text{s}^{28}, \quad \psi_{H_2O} = 2.6; \quad M_{H_2O} = 18 \text{ g/mole};$$

$$\mu_w : \text{centipoise}, \quad V_{O_2} = 25.6 \text{ cm}^3/\text{mole}$$

$$D_v^g = 0.242 \left(\frac{T}{293.15} \right)^{2.334}, \text{ cm}^2/\text{s}^{28, 29}$$

$$D_{O_2}^N = 0.0031 e^{\frac{-2768}{T}}, \text{ cm}^2/\text{s}^{30}$$

$$D_w^N = \left(1.76 \times 10^{-5} + \beta 1.94 \times 10^{-4} \lambda \right) \exp \left(-\frac{2436}{T} \right), \text{ cm}^2/\text{s}^{31, 32}, \quad \beta = 2.2$$

$$H_{O_2}^N = 1.33 \times 10^6 e^{\frac{-666}{T}}, \text{ atm cm}^3/\text{mol}^{30}$$

$$H_{O_2}^w = 5.08 \times 10^6 e^{\frac{-498}{T}}, \text{ atm cm}^3/\text{mol}^{33}$$

$$\log_{10} P_{sat} = -2.1794 + 0.02953(T - 273.15) - 9.1837 \times 10^{-5} (T - 273.15)^2 + 1.4454 \times 10^{-7} (T - 273.15)^3, \quad P_{sat} : \text{atm}^{27}$$

$$\mu_{water} = 0.4656 - 5.3859 \times 10^{-3} T + 2.3469 \times 10^{-5} T^2 - 4.5570 \times 10^{-8} T^3 + 3.3231 \times 10^{-11} T^4,$$

$$\text{Pa} \cdot \text{s}^{29}, \text{ in the range of } 273.15\text{K} \sim 373.15\text{K}$$

$$k_N = \exp \left(1268 \left(\frac{1}{303} - \frac{1}{T} \right) \right) (0.005139 \lambda - 0.00326), \quad \frac{1}{\Omega \cdot \text{cm}}^{27}$$

$$\text{Water content in Nafion, } \lambda = \frac{C_w^N}{C_f}$$

$$\text{Electro-osmotic drag coefficient,}^{27} \quad n = \frac{2.5}{22} \lambda$$

$$\text{Exchange current density,}^1 \text{ A/cm}^2, \quad i_0 = i_{0,273} 2^{\frac{T-273}{10}}$$

Table 4.5 Parameters used in the model.

| | |
|-----------------------------------------------------------|----------------------------------------|
| GDL properties | |
| ε_{GDL} | 0.5 |
| δ_{GDL}^1 | 250 μm |
| $K_{w,0}^{GDL}$ | $2.0 \times 10^{-11} \text{ cm}^2$ |
| CL properties | |
| ε_{CL} | 0.12 |
| δ_{CL}^1 | 16 μm |
| $K_{w,0}^{CL}$ | $5.0 \times 10^{-13} \text{ cm}^2$ |
| m_{Pt}^1 | 0.4 mg Pt/cm ² |
| a_{Pt}^1 | 1000 cm ² /(mg Pt) |
| Volume fraction of Nafion in CL pellet, ε_N^p | 0.393 |
| Radius of the spherical catalyst pellet, r | $1 \times 10^{-5} \text{ cm}$ |
| Thickness of Nafion film, δ_N | $1 \times 10^{-6} \text{ cm}$ |
| Membrane properties | |
| δ_{MEM}^1 | 50 μm |
| C_f^1 | $1.2 \times 10^{-3} \text{ mole/cm}^3$ |

Table 4.6 Simulation conditions.

| | |
|-------------------------------------------------|-------------------------------------------|
| Temperature | 333.15 K |
| Pressure | 1 atm |
| Humidity of the air inlet | 100% |
| Humidity at anode | 100% |
| Evaporation rate constant, k_v | $100 \frac{1}{\text{atm} \cdot \text{s}}$ |
| Condensation rate constant, k_c | $100 \frac{1}{\text{s}}$ |
| Transfer coefficient, α_c | 1.0 |
| Open-circuit potential, U_{ref} | 1.0 V |
| Stoichiometry of air | 3 |
| Reference oxygen concentration, $C_{O_2,ref}$ | $5.55 \times 10^{-6} \text{ mole/cm}^3$ |
| Reference exchange current density, $i_{0,273}$ | $1.0 \times 10^{-6} \text{ A/cm}^2$ |

4.4 Results and Discussion

Fig. 4.7 shows the simulated results using the experimentally determined capillary curve of GDL (G1) and the fitted capillary curve of CL (C1) in Fig. 4.3 at three fuel cell voltages, 0.8, 0.6, and 0.4V. Note that as the cell voltage decreases from 0.8V to 0.6V, the current density increases, resulting in higher saturation levels in the GDL. The same phenomenon is also observed when the voltage decreases from 0.6V to 0.4V although the magnitude is little in the figure. The saturation levels in the GDL are in the ranges of 0.30 to 0.71 at the cell voltage of 0.4V. The saturation levels

in the CL are about 0.82 and are stable at different cell voltages. The CL has higher liquid water saturation level because, first, water is produced there; and, second, it is more hydrophilic than the GDL. Sufficient saturation gradient has to be generated in order to create the capillary driving force that is needed to transport liquid water out of the CL. Since the slope of the CL capillary curve in the hydrophobic region is very steep, small saturation gradient is needed to create the capillary driving force, leading to stable saturation levels in the CL. In the GDL, big saturation gradients are observed in Fig. 4.7.

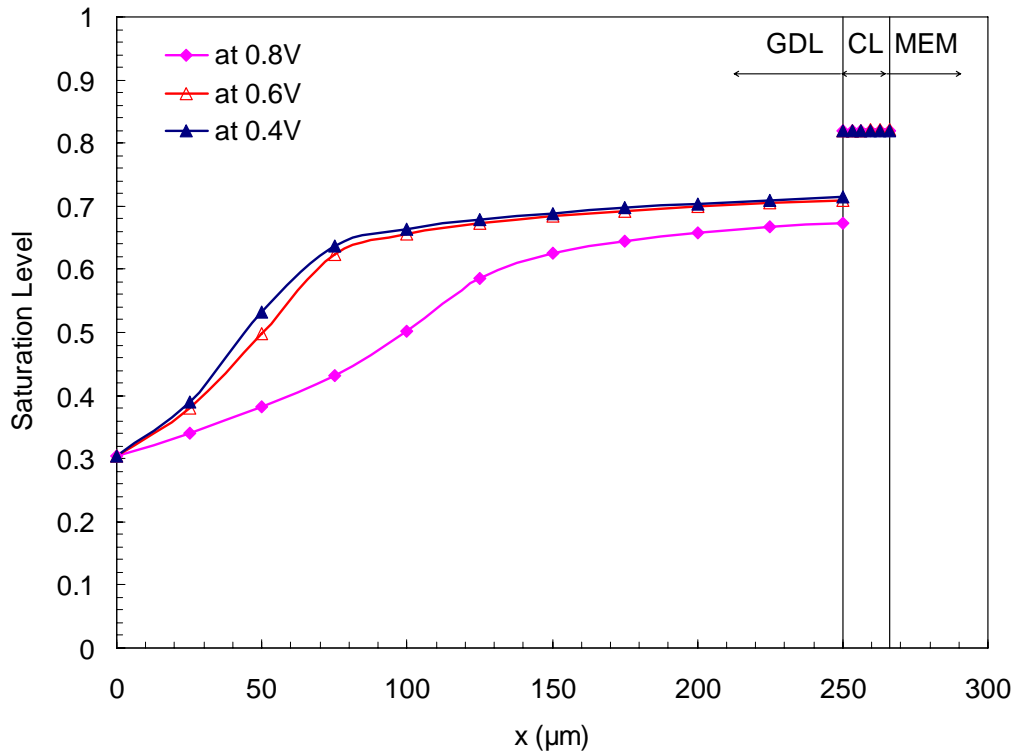


Figure 4.7 Saturation level in GDL and CL for the base case with G1 and C1 at various cell voltages (refer to Fig. 4.3 and Table 4.1).

As shown earlier in this chapter, the capillary pressure curves can be modified by changing the properties of the corresponding porous materials. The effect of this change is examined in this study. In the first case, the capillary function of the GDL is fixed to be the experimentally determined curve, G1, in Fig. 4.3. The capillary functions of the CL are those denoted by C1, C2, C3, C4 and C5 as shown in Fig. 4.4. These combinations are used to study the influences of the CL capillary function on the water management of PEM fuel cells. The saturation level profiles predicted by different CL capillary pressure curves are plotted in Fig. 4.8.

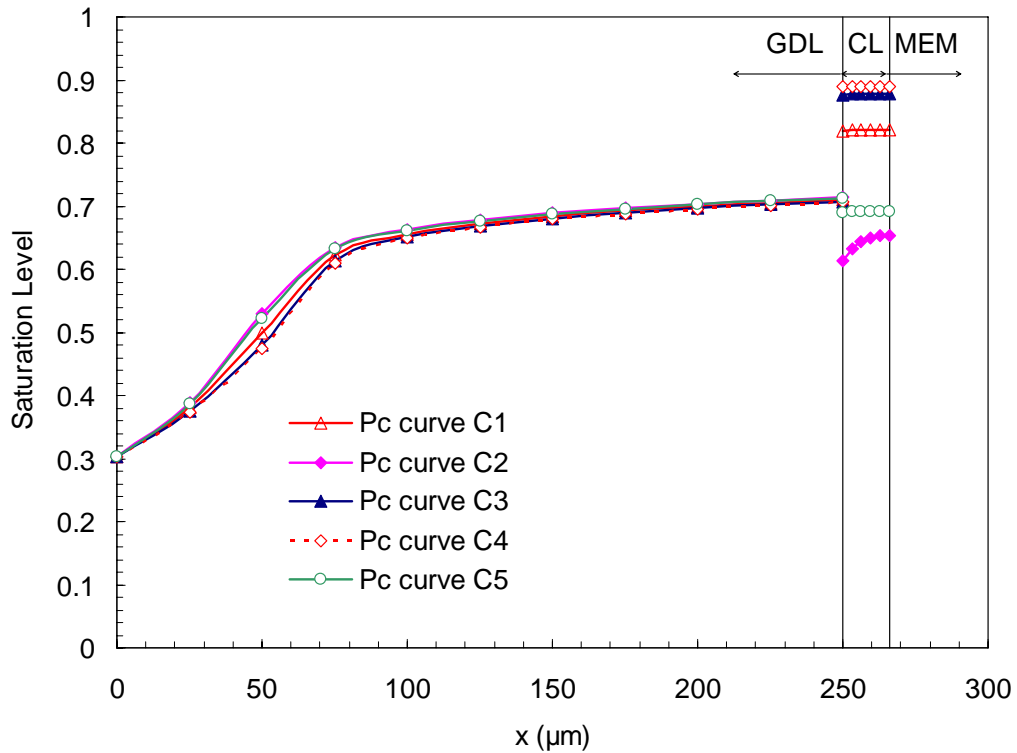


Figure 4.8 The effect of the CL capillary functions on the saturation levels in the GDL and CL at 0.6V (refer to Fig. 4.4 and Table 4.1).

Fig. 4.8 shows that for all the CL capillary pressure cases, from C1 to C5, the adjustment used in case C3 and C4 have the greatest impact on the saturation level in the CL. However, these changes have very little impact on the saturation level in the GDL. To explain the large increase in the saturation level in the CL in case C4, we will look at the values of the capillary diffusion coefficient D_c (Eq. 4.10) for these cases.

Fig. 4.9 shows the values of D_c for the cases of G1 and C1 to C5. First, note that the boundary condition of $p_c=0$ at the gas channel/GDL interface and the capillary force balance (Eq. 4.2) bind the transport phenomenon in the hydrophobic region of the capillary curves used in Fig. 4.4. This region is represented by the thicker part of the D_c curves in Fig. 4.9. Second, for all the CL capillary curves except for C2, the D_c values increase greatly within narrow saturation ranges, allowing liquid water in CL to be rapidly transported out of these porous media before they reach high values. This acts to restrain the saturation levels in the CL to the corresponding narrow ranges as shown in Fig. 4.9. Third, as the D_c curve moves to the left, as in cases C5 and C2 or C1, the saturation level in the CL also shifts to a lower range. In the case of C4 where the P_c curve is shifted to the right, the saturation level in the CL automatically increases for the same P_c value or saturation level in the GDL.

Furthermore, the D_c values of case C4 are high only at high saturation range ($s > 0.80$). Thus, the CL for case C4 reaches the highest saturation levels as shown in Fig. 4.8. For the capillary curve C5, shifting the curve to the left makes it less hydrophilic or more hydrophobic. Consequently, the D_c values, as well as the capillary curve, cover a lower saturation level range, and the predicted water saturation level in the CL for case C5 is lower. Note that the saturation level in the CL is even lower than that of the GDL, because in the hydrophobic region of the capillary curve, C5, its D_c values cover lower saturation levels as shown in Figs. 4.4 and 4.9. Although the case of having a CL more hydrophobic than a GDL is quite rare in practice, it was used here to elucidate what kind of CL would result in better fuel cell performance. This could be achieved by adding a hydrophobic material such as PTFE into the CL as done by Nguyen's group.^{20, 34} It showed that within certain range, the more hydrophobic the CL was, the better fuel cell performance was obtained.

Finally, note that the D_c curves of cases C1 and C2 are exactly the same in Fig. 4.9 as expected, because shifting the P_c curve downward does not change D_c because values of the ∇p_c term stay the same (see Eq. 4.10). However, shifting the capillary curve downward moves the cross point ($p_c=0$) to the left, which leads to different saturation levels in the CL. The more hydrophobic curve, C2, results in much lower saturation levels in the CL.

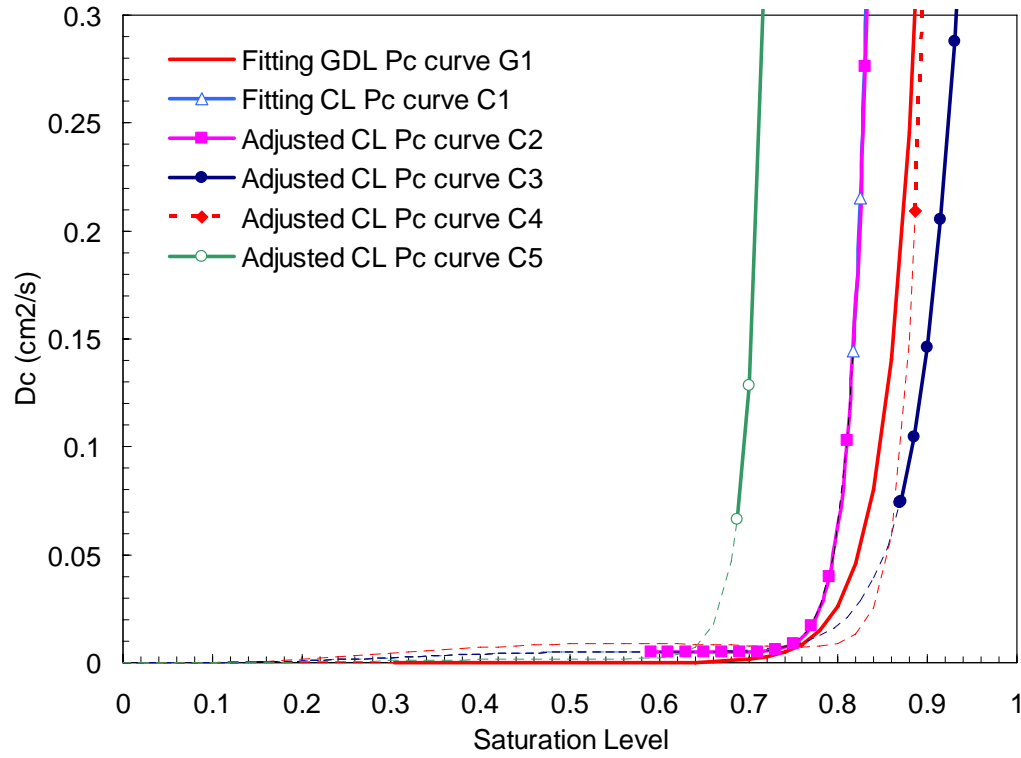


Figure 4.9 Capillary diffusion coefficients for different CL capillary functions (refer to Fig. 4.4 and Table 4.1).

These results show that in addition to the impact of the capillary pressure curve on the capillary diffusion term, which affects the water removal rate, the interaction between the capillary property of the GDL and CL plays a very important role in determining the saturation levels in the GDL and CL. This shows that neglecting this effect will lead to inaccurate predictions of the liquid water effect on the performance of the cathode.

Fig. 4.10 shows the polarization curves with the corresponding CL capillary

functions. The polarization curves are the same at high cell voltages because of the low current densities and associated low saturation levels. While at low cell voltages, particularly below 0.7V, the CLs with least water, curves C2 and C5, predict the best fuel cell performance. The most hydrophilic capillary curves, C3 and C4, result in the highest saturation levels in the CL and, consequently, the worst fuel cell performances in Fig. 4.10. Note that even though cases C1 and C2 have the same D_c , fuel cell performances are different due to different liquid saturation levels in the CLs.

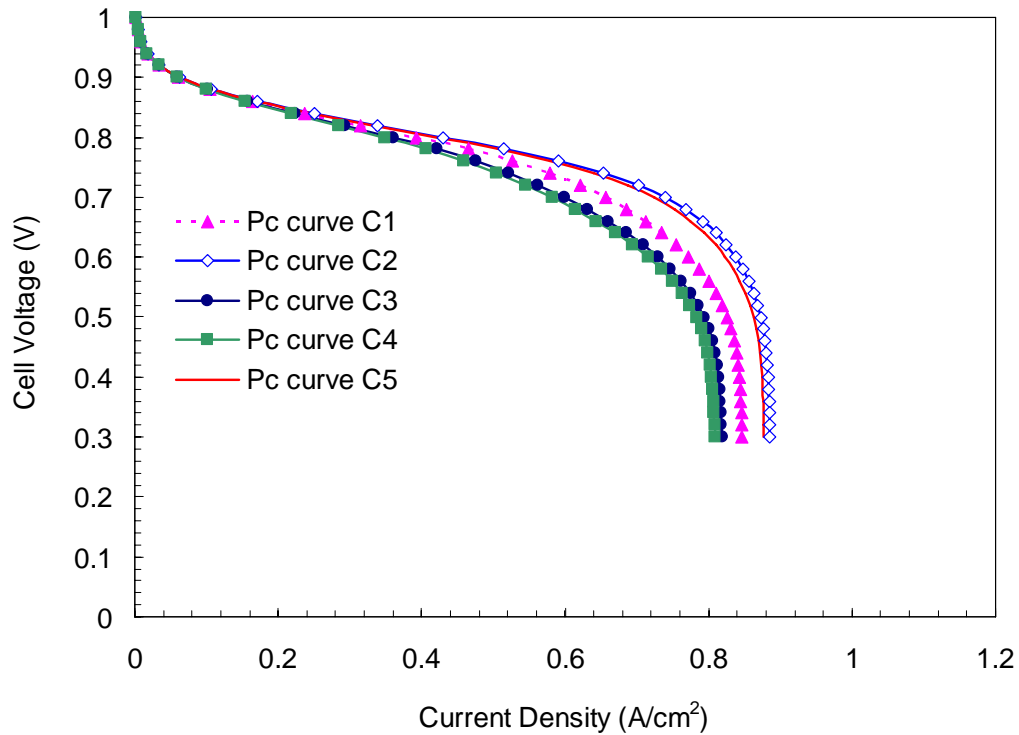


Figure 4.10 The effects of the CL capillary pressure functions on the fuel cell performance (refer to Fig. 4.4 and Table 4.1).

The analysis of the effect of the GDL capillary function on the saturation levels in the GDL and CL and the fuel cell performance is carried out similarly to those discussed above for the CL. To examine the GDL capillary effect, curve C1 in Fig. 4.5 is used as the CL capillary function, while the GDL capillary curves are those denoted with G1, G2, G3, G4 and G5 in Fig. 4.5. The results are shown in Figs. 4.11, 4.12 and 4.13.

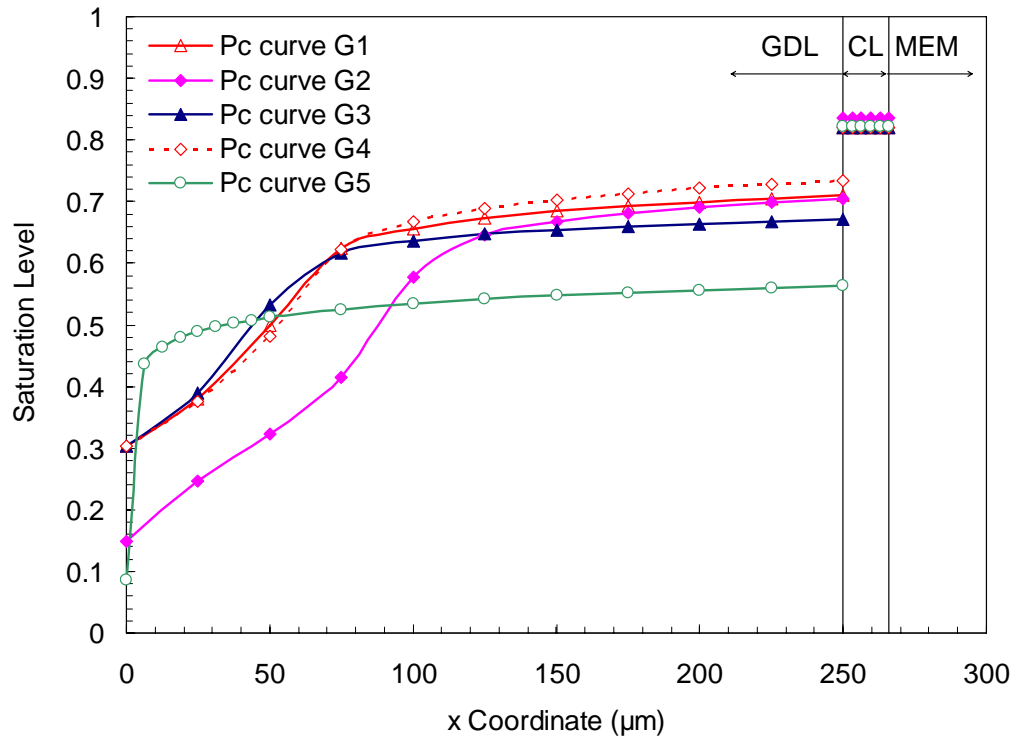


Figure 4.11 The effect of the GDL capillary functions on the saturation levels in the GDL and CL at 0.6V (refer to Fig. 4.5 and Table 4.1).

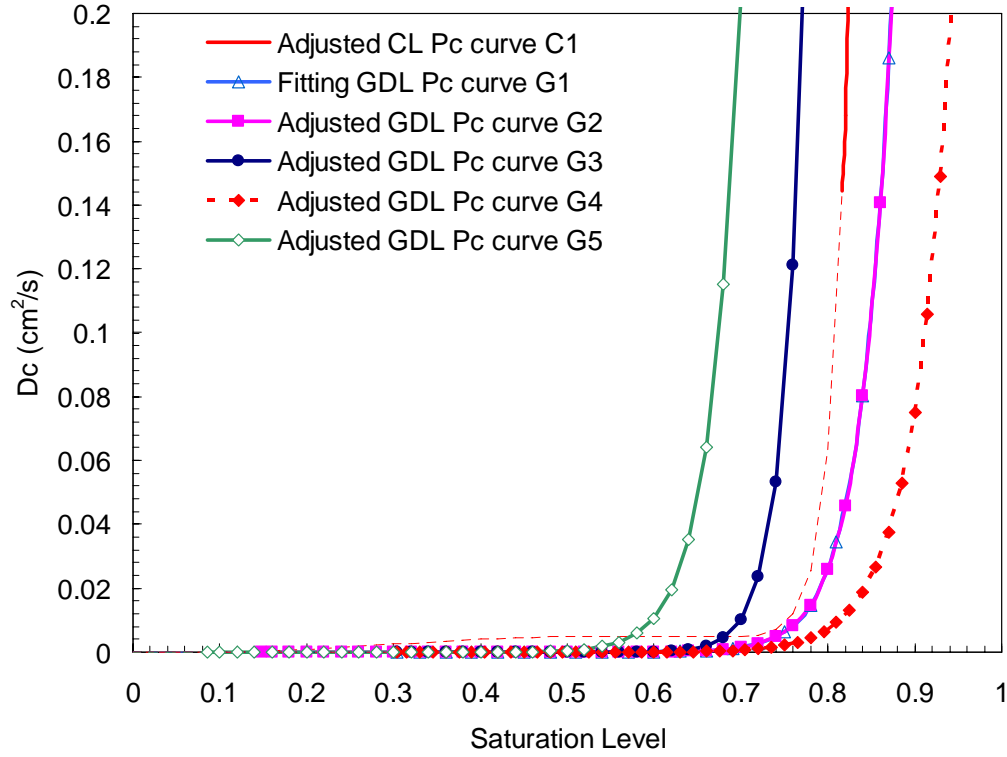


Figure 4.12 Capillary diffusion coefficients for different GDL capillary functions (refer to Fig. 4.5 and Table 4.1).

Fig. 4.12 shows that the capillary diffusion coefficient (D_c) of the CL, curve C1, increases greatly within a very narrow saturation level region, which means that the saturation level in the CL will be restricted to this region and will not be affected too much by the change of the GDL capillary properties. Consequently, one can consider only the GDL capillary effects in these cases.

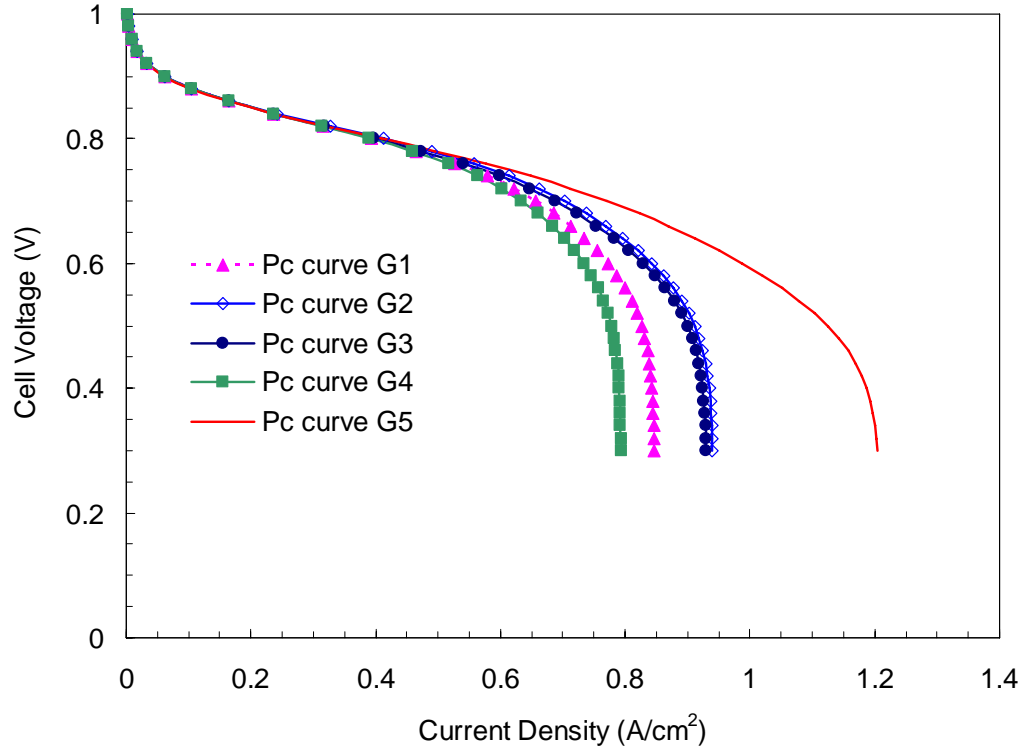


Figure 4.13 The effects of the GDL capillary pressure functions on the fuel cell performance (refer to Fig. 4.5 and Table 4.1).

The capillary diffusion coefficients (D_c) for cases G1 and G2 are the same, as expected because the term ∇p_c does not change. The saturation level ranges covered by the capillary diffusivity, D_c , ranking from high saturation level to low saturation level as shown in Fig. 4.12, are G4, G1/G2, G3 and G5. Note that the saturation level profiles in the GDL follow a similar order as shown in Fig. 4.11. The only exception is in the region near the GDL/Channel interface where the saturation level of case G1 is higher than that of case G2. This is attributed to the fact that shifting the capillary curve G1 downward shifts the $p_c=0$ point, boundary condition applied at the

GDL/Channel, to a lower saturation level, which causes the region near this interface to be lower. The saturation levels in the CL for all these cases, G1-G5, are in a very close range because of the narrow saturation range covered by the D_c values of the CL as discussed earlier.

The cell performance shown in Fig. 4.13 is consistent with the saturation levels shown in Fig. 11 and the capillary transport capability in Fig. 4.12. That is, the lower saturation level is for the GDL, the better cell performance is. Note that Lin and Nguyen³⁵ had studied the effects of the GDL hydrophobicity on the fuel cell performances. It was shown that for both the SGL and Toray carbon papers, the water-proofed GDLs improved the fuel cell performances. However, beyond certain range, the fuel cell performances decreased. This might result from the decreased porosity in the GDL, when too much PTFE was added. Lim and Wang³⁶ found similar phenomena and they showed that the 10% wt PTFE loading GDL gave the best fuel cell performance. These experimental results confirmed this model's results that more hydrophobic GDL leads to the better cell performance.

The results of this study are summarized in Table 4.7. It is seen from Table 4.7 that the GDL capillary function greatly affects the saturation levels in GDL and CL, as well as the cell performance. However, the CL capillary function has very minimal effect on the saturation levels and cell performance within the changes considered

here, because the gas phase transport rate in the GDL is the dominating factor. The boundary condition of $p_c=0$ at the gas channel/GDL interface restrains the GDL and CL capillary functions to be effective only in the hydrophobic region.

Table 4.7 Summary of the capillary effects.

| Curve | | Operation | Saturation range covered by Dc | Saturation level | | Limiting current |
|-------|----|--------------------------------------------|--------------------------------|------------------|-----------|------------------|
| GDL | CL | | | GDL | CL | |
| G1 | C1 | Fitted (base case) | = | = | = | = |
| | C2 | Shift downward of C1 | = | \approx | ↓ | ↑ |
| | C3 | Decrease slope in hydrophobic region of C1 | ↑ | \approx | ↑ | ↓ |
| | C4 | Shift to the right of C1 | ↑ | \approx | ↑ | ↓ |
| | C5 | Shift to the left of C1 | ↓ | \approx | ↓ | ↑ |
| G1 | C1 | Experimentally determined (base case) | = | = | = | = |
| G2 | | Shift downward of G1 | = | ↓ | \approx | ↑ |
| G3 | | Increase slope in hydrophobic region of G1 | ↓ | ↓ | \approx | ↑ |
| G4 | | Decrease slope in hydrophobic region of G1 | ↑ | ↑ | \approx | ↓ |
| G5 | | Shift to the left of G1 | ↓ | ↓ | \approx | ↑ |

Note: the comparisons are made relative to the base case, which corresponds to the case of (G1, C1). “=” denotes no change, “ \approx ” denotes very small change, “↑” denotes increase, and “↓” denotes decrease.

4.5 Conclusions

A two-phase model was developed for a PEM fuel cell in which 1) experimentally obtained capillary pressure curve of the GDL and fitted capillary pressure curve of the CL were used; 2) liquid water saturation level jump condition at the GDL/CL interface resulting from the capillary force balance was included; and 3) the effect of the capillary pressure properties of the GDL and CL on the liquid water transport rate, the liquid water saturation level in these porous media, and the fuel cell performance was investigated. From the analysis of the CL and GDL capillary effects, it is evident that both the liquid transport capability and the interaction between the GDL and CL capillary properties play important roles in the liquid transport in these porous media. Neglecting one or the other will result in significant loss of information, and sometimes misleading predictions. Both the GDL and CL capillary curves may be modified by changing the material properties, which makes it possible to make better porous media used in PEM fuel cells. Capillary curves of the GDL and CL are useful properties that may be used in predicting the saturation levels in the porous media, as well as comparing the cell performances. The capillary function of the GDL within the range included here has greater effects on the saturation levels and fuel cell performance than that of the CL. Higher fuel cell performance is obtained with GDL and CL with capillary properties that result in lower saturation levels in these media

during operation. The key properties are high capillary diffusion capability and low hydrophilic porosity. Multi-dimensional effect is not included in this chapter and may be studied in the future.

4.6 References

1. G. Lin, W. He and T. V. Nguyen, Modeling Liquid Water Effects in the Gas Diffusion and Catalyst Layers of the Cathode of a PEM Fuel Cell, *J. Electrochem. Soc.*, 151 (12), A1999, **2004**.
2. G. Lin and T. V. Nguyen, A Two-Dimensional Two-Phase Model of a PEM Fuel Cell, *J. Electrochem. Soc.*, 153 (2), A372, **2006**.
3. D. Natarajan and T. V. Nguyen, A Two-Dimensional, Two-Phase, Multicomponent, Transient Model for the Cathode of a Proton Exchange Membrane Fuel Cell Using Conventional Gas Distributors, *J. Electrochem. Soc.*, 148 (12), A1324, **2001**.
4. T. Berning and N. Djilali, A 3D, Multiphase, Multicomponent Model of the Cathode and Anode of a PEM Fuel Cell, *J. Electrochem. Soc.*, 150 (12), A1589, **2003**.
5. H. Meng and C.-Y. Wang, Model of Two-Phase Flow and Flooding Dynamics in Polymer Electrolyte Fuel Cells, *J. Electrochem. Soc.*, 152 (9), A1733, **2005**.

6. U. Pasaogullari and C.-Y. Wang, Two-Phase Modeling and Flooding Prediction of Polymer Electrolyte Fuel Cells, *J. Electrochem. Soc.*, 152 (2), A380, **2005**.
7. U. Pasaogullari and C. Y. Wang, Liquid Water Transport in Gas Diffusion Layer of Polymer Electrolyte Fuel Cells, *J. Electrochem. Soc.*, 151 (3), A399, **2004**.
8. Y. Wang, Porous-Media Flow Fields for Polymer Electrolyte Fuel Cells II. Analysis of Channel Two-Phase Flow, *J. Electrochem. Soc.*, 156 (10), B1134, **2009**.
9. J. D. Fairweather, P. Cheung, J. St-Pierre and D. T. Schwartz, A Microfluidic Approach for Measuring Capillary Pressure in PEMFC Gas Diffusion Layers, *Electrochem. Commun.*, 9 (9), 2340, **2007**.
10. T. V. Nguyen, G. Lin, H. Ohn and X. Wang, Measurement of Capillary Pressure Property of Gas Diffusion Media Used in Proton Exchange Membrane Fuel Cells, *Electrochem. Solid-State Lett.*, 11 (8), B127, **2008**.
11. T. V. Nguyen, G. Lin, H. Ohn, X. Wang, D. S. Hussey, D. L. Jacobson and M. Arif, Measurements of Two-Phase Flow Properties of the Porous Media Used in PEM Fuel Cells, *ECS Trans.*, 3 (1), 415, **2006**.
12. H. Ohn, D. Hussey, D. Jacobson, M. Arid and T. Nguyen, The Capillary Pressure Properties of Gas Diffusion Materials Used in PEM Fuel Cells, *ECS Trans.*, 1 (6), 481, **2006**.

13. Q. Ye and T. V. Nguyen, Three-Dimensional Simulation of Liquid Water Distribution in a PEMFC with Experimentally Measured Capillary Functions, *J. Electrochem. Soc.*, 154 (12), B1242, **2007**.
14. J. T. Gostick, M. W. Fowler, M. A. Ioannidis, M. D. Pritzker, Y. M. Volfkovich and A. Sakars, Capillary Pressure and Hydrophilic Porosity in Gas Diffusion Layers for Polymer Electrolyte Fuel Cells, *J Power Sources*, 156 (2), 375, **2006**.
15. J. T. Gostick, M. A. Ioannidis, M. W. Fowler and M. D. Pritzker, Direct measurement of the capillary pressure characteristics of water-air-gas diffusion layer systems for PEM fuel cells, *Electrochem. Commun.*, 10 (10), 1520, **2008**.
16. I. R. Harkness, N. Hussain, L. Smith and J. D. B. Sharman, The Use of a Novel Water Porosimeter to Predict the Water Handling Behaviour of Gas Diffusion Media Used in Polymer Electrolyte Fuel Cells, *J Power Sources*, 193 (1), 122, **2009**.
17. E. C. Kumbur, K. V. Sharp and M. M. Mench, Validated Leverett Approach for Multiphase Flow in PEFC Diffusion Media I. Hydrophobicity Effect, *J. Electrochem. Soc.*, 154 (12), B1295, **2007**.
18. E. C. Kumbur, K. V. Sharp and M. M. Mench, Validated Leverett Approach for Multiphase Flow in PEFC Diffusion Media II. Compression Effect, *J. Electrochem. Soc.*, 154 (12), B1305, **2007**.

19. E. C. Kumbur, K. V. Sharp and M. M. Mench, Validated Leverett Approach for Multiphase Flow in PEFC Diffusion Media - III. Temperature Effect and Unified Approach, *J. Electrochem. Soc.*, 154 (12), B1315, **2007**.
20. R. Friedmann and T. V. Nguyen, Optimization of the Cathode Catalyst Layer Composition Using a Novel 2-Step Preparation Method, *ECS Trans.*, 16 (2), 2021, **2008**.
21. C.-Y. Wang, Two-Phase Flow and Transport. In *Handbook of Fuel Cells - Fundamentals, Technology and Applications*, W. Vielstich, H. A. Gasteiger and A. Lamm, Eds. John Wiley & Sons, Ltd.: Vol. 3: Fuel Cell Technology and Applications, pp 337, 2003.
22. X. Wang and T. V. Nguyen, A Theoretical Study of the Effects of Two-Phase Transport Properties of the Catalyst and Gas Diffusion Layers in the Cathode on the Performance of a PEMFC, *ECS Trans.*, 11 (1), 693, **2007**.
23. A. Z. Weber, R. M. Darling and J. Newman, Modeling Two-Phase Behavior in PEFCs, *J. Electrochem. Soc.*, 151 (10), A1715, **2004**.
24. W. He, J. S. Yi and T. V. Nguyen, Two-Phase Flow Model of the Cathode of PEM Fuel Cells Using Interdigitated Flow Fields, *AIChE J.*, 46 (10), 2053, **2000**.
25. G. F. Froment and K. B. Bischoff, *Chemical Reactor Analysis and Design*, 2nd ed.; Wiley: New York, p xxxiv, 1990.

26. A. Z. Weber and J. Newman, Effects of Microporous Layers in Polymer Electrolyte Fuel Cells, *J. Electrochem. Soc.*, 152 (4), A677, **2005**.
27. T. E. Springer, T. A. Zawodzinski and S. Gottesfeld, Polymer Electrolyte Fuel-Cell Model, *J. Electrochem. Soc.*, 138 (8), 2334, **1991**.
28. R. B. Bird, W. E. Stewart and E. N. Lightfoot, *Transport phenomena*, 2nd ed.; J. Wiley: New York, p xii, 2002.
29. D. R. Lide, *CRC Handbook of Chemistry and Physics, Internet Version 2007, (87th Edition)*, <<http://www.hbcpnetbase.com>>, Taylor and Francis: Boca Raton, FL, 2007.
30. D. M. Bernardi and M. W. Verbrugge, Mathematical-Model of a Gas Diffusion Electrode Bonded to a Polymer Electrolyte, *AIChE J.*, 37 (8), 1151, **1991**.
31. S. Motupally, A. J. Becker and J. W. Weidner, Diffusion of Water in Nafion 115 Membranes, *J. Electrochem. Soc.*, 147 (9), 3171, **2000**.
32. T. V. Nguyen and R. E. White, A Water and Heat Management Model for Proton-Exchange-Membrane Fuel Cells, *J. Electrochem. Soc.*, 140 (8), 2178, **1993**.
33. J. C. Amphlett, R. M. Baumert, R. F. Mann, B. A. Peppley, P. R. Roberge and T. J. Harris, Performance Modeling of the Ballard Mark Iv Solid Polymer Electrolyte Fuel Cell 1. Mechanistic Model Development, *J. Electrochem. Soc.*, 142 (1), 1,

1995.

34. T. V. Nguyen, D. Natarajan and R. Jain, Optimized Catalyst Layer Structure for PEM Fuel Cells, *ECS Trans.*, 1 (6), 501, **2006**.
35. G. Lin and T. V. Nguyen, Effect of Thickness and Hydrophobic Polymer Content of the Gas Diffusion Layer on Electrode Flooding Level in a PEMFC, *J. Electrochem. Soc.*, 152 (10), A1942, **2005**.
36. C. Lim and C. Y. Wang, Effects of Hydrophobic Polymer Content in GDL on Power Performance of a PEM Fuel Cell, *Electrochim. Acta*, 49 (24), 4149, **2004**.

Chapter 5

Modeling the Effects of the Micro-Porous Layer on the Net Water Transport Rate Across the Membrane in a PEM Fuel Cell

5.1 Introduction

The conventional water management approach of adding water (gas/liquid phase) to the anode side and removing water from the cathode side is a self-defeating process. A more efficient process of water management in a PEM fuel cell is by engineering the material properties of the porous media used in the membrane and electrode assembly (MEA) to force the liquid water in the cathode back to the anode so that a zero-net-water-transport-across-the-membrane can be achieved.¹ If this could be achieved, it would minimize or eliminate the need for anode gas humidification.

Previous experimental studies have shown that the performance of a PEM fuel cell was improved by the application of an MPL in the cathode.²⁻¹³ The PTFE content in the MPL was found to have a great effect on the fuel cell performance. The optimal PTFE content was reported to be between 10 %wt and 30 %wt in literature.^{6, 7, 11} Lin and Nguyen⁵ hypothesized that the MPL improved the fuel cell performance by forcing more liquid water to flow from the cathode to the anode. Atiyeh *et al.*² and Karan *et al.*⁴ showed that although the MPL improved the fuel cell performance at 60

°C (60%/100% and 100%/60% RH for cathode/anode), the liquid water flux across the membrane was not affected by the MPL. The improved fuel cell performance was attributed to the better contact between the MPL and CL. On the other hand, Fujii *et al.*¹⁴ showed that at 80 °C and low humidity (20%/20% RH for cathode/anode), the water flux from the cathode to the anode through the membrane was improved with an MPL at the cathode side. The discrepancy between these two experiments may result from the different operation conditions and materials used. One normally would expect the MPL to have even greater impact, when the cathode operates under saturated or flooding conditions typical of low operating temperature and/or high relative humidity operation. We hypothesize that the discrepancies observed by Atiyeh *et al.*² and Karan *et al.*⁴ were caused by cracks formed in the MPLs.

Nguyen *et al.*¹⁵ showed that MPLs with cracks (See Fig. 5.1) exhibited capillary pressure curves resembling those of the GDLs. Cracks in the MPL allow liquid water to by-pass the pores in the MPL and their associated interfacial properties. Since these cracks were much larger than the average pore size of the MPL, the resulting capillary pressure was much lower. MPLs with no cracks prepared by a confidential client exhibited much higher capillary pressure. Hizir *et al.*¹⁶ also observed cracks in the MPLs and the lack of a liquid water saturation level jump condition at the MPL and CL interface in their neutron scattering measurements. Based on the results from

Nguyen *et al.*¹⁵ and Hizir *et al.*¹⁶, it is reasonable to hypothesize that PEM fuel cells using MPLs with cracks could lead to behavior contrary to the results to be expected. Since MPLs with cracks exhibited similar capillary pressure properties to those of the GDLs, no higher liquid pressure would be created to help drive liquid water back to the anode. Consequently, no effect on the water flux across the membrane would be observed as reported by Atiyeh *et al.* and Karan *et al.* Also, Lin¹⁷ from TVN Systems, Inc. recently confirmed that excessive anode flooding was observed in the hydrogen electrode of a PEM fuel cell when an MPL was used at the cathode, while no or minimal anode flooding was observed when the MPLs were used in both the cathode and anode. The explanation was that the MPL in the cathode forced excessive water back to the anode, leading to anode flooding. However, when the same MPLs were used in both the anode and cathode, which created high liquid water pressure at both electrodes, a smaller liquid pressure gradient was generated, leading to lower water permeation from the cathode to the anode. Finally, very recent works by Gostick *et al.*¹⁸ and Dai *et al.*¹⁹ on the effect of the MPL on the water flux in a PEM fuel cell suggests that the MPL limited the liquid water access to the GDL, leading to lower saturation levels in the GDL.



Figure 5.1 SEM picture of an MPL.

Numerical simulations have shown that the MPL improved the PEM fuel cell performance.²⁰⁻²⁵ These models focused either on properties of the MPL such as porosity, thickness, pore size, and the wettability,^{20-22, 24, 25} or on operational conditions such as the humidity and the fuel concentration.²³ The conclusions drawn depended on the aspects investigated. When the electrical aspects were considered, the suggestion was that the dense MPL reduced the contact resistance between the GDL and the CL. When the liquid water transport aspects were considered, the suggestion²⁴ was that the highly hydrophobic MPL forced liquid water generated at the cathode back to the anode, resulting in higher membrane hydration and conductivity and low liquid water saturation level in the cathode.

Weber and Newman²⁴ focused on the water management effects of the MPLs in PEM fuel cells and suggested that highly hydrophobic MPLs force the liquid water

generated at the cathode back to the anode. The increased back liquid water permeation results in higher membrane hydration and conductivity, and low liquid water saturation level in the cathode. The capillary property of the MPL was adjusted by changing the fraction of the hydrophilic pores. This work is probably the most comprehensive modeling study of the effects of the MPL on a PEM fuel cell performance. By determining the morphological property (porosity, thickness, pore size distribution and fraction of hydrophilic pore volume) of the MPL that provided a good fit between the experimental data and the model predictions, this work helped explain the effect of the presence of an MPL at the cathode on the water transport processes in the fuel cell and the morphological properties that played a dominant role in these processes. However, the capillary pressure property generated by the theoretical approach used in Weber and Newman's model ^{24, 26} is not representative of the capillary property of actual PTFE treated carbon-based gas diffusion media used in PEM fuel cells. Pasaogullari *et al.* ^{21, 22} showed similar phenomena in a PEM fuel with an MPL on the cathode side. The back-transport rate of liquid water was greatly affected by the properties of the porous media. However, since the wrong capillary pressure property-Leverett function developed for sands-was used in Pasaogullari *et al.*'s work, the model predicted unrealistically low liquid water saturation levels in the porous media.

Based on the work by Weber and Newman,²⁴ our group has proposed a water management approach in which the capillary property of the porous media used in a PEM fuel cell will be engineered to achieve a condition of zero-net-water-transport-across-the-membrane.¹ If this could be achieved, it would minimize or eliminate the need for anode gas humidification. To achieve this specific goal in a more efficient manner, a two-phase flow model that includes an MPL on the cathode side was developed. This model is an extension of a previous model²⁷ where the effect of the shape and magnitude of an experimentally obtained capillary curve of a GDL on the water transport processes in a membrane and electrode of a PEM fuel cell was evaluated. This model took into account the recently discovered mixed (both hydrophobic and hydrophilic) capillary property of PTFE treated carbon-based gas diffusion materials used in PEM fuel cells^{28,29} and our knowledge of how to modify the capillary pressure property of these carbon-base porous media. The model was used to evaluate the role of the MPL and the effect of its capillary property on the net water transport rate across the membrane, the liquid water saturation levels in the porous media in the cathode, and consequently, the PEM fuel cell performance. The results from this study could shed light on the material engineering strategy needed to achieve the condition of zero-net-water-transport-across-the-membrane. Cases with and without the MPLs are compared to elucidate the MPL effect. Next, the effects of

the capillary property of the MPL on the water transport rate across the membrane and fuel cell performance were investigated by adjusting the shapes and values of the capillary curves.

5.2 Model Development

5.2.1 Modeled Domain

The modeled domain is shown in Fig. 5.2. The MPL is located between the GDL and CL. In this study, only the cathode side is considered since the cathode plays a dominant role in the fuel cell performance because of the sluggish oxygen reduction reaction. The porous media were considered isotropic for simplicity. The CL was assumed to consist of spherical agglomerate of C/Pt/Nafion. Other assumptions listed in Chapter 4 and reference 27 are still valid here.

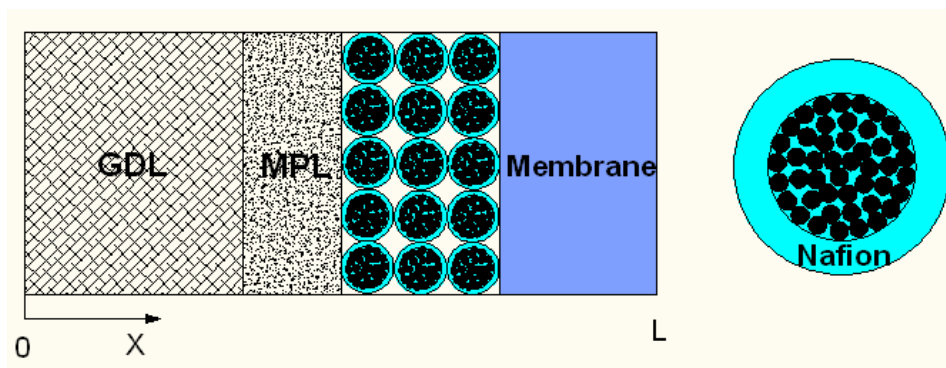


Figure 5.2 Schematic diagram of the modeled domain.

5.2.2 Governing Equations

There are eight variables to be solved in the modeled domain. The governing equations are summarized in Table 5.1. The detailed steps were also included in Chapter 4 and references 27 and 30. Note that in this study, two additional variables, the water saturation level in the MPL (s_{MPL}) and the liquid water pressure (p_l) in the modeled domain, are included. The liquid water pressure is used to account for the transport of liquid water across the membrane from the cathode to the anode. The governing equation of water transport in the MPL is similar to that in the GDL. The capillary pressure expression is of the form ^{27, 31}

$$p_c = d \left[e^{-a_1(s-c)} - e^{a_2(s-c)} \right] + b \quad [5.1]$$

where s is the saturation level, and a_1 , a_2 , b , c and d are adjustable parameters.

In the previous study, the pressure driven permeation was not included, because this term is very small compared to the electro-osmotic drag term in the case without the MPL. In this study, because the MPL may increase the liquid pressure to a very high level, the term that accounts for the pressure-gradient driven permeation across the membrane was included. In Table 5.1, the water flux in the membrane, N_w^N , consists of the concentration gradient-driven diffusion, electro-osmotic drag, and pressure driven permeation terms, respectively, as shown below.

$$N_w^N = \frac{i_+}{F} n - D_w^N \frac{dC_w^N}{dx} - \frac{\rho_w}{M_w} \frac{K_l^{MEM}}{\mu_w} \frac{dp_l}{dx} \quad [5.2]$$

The parameters, ρ_w , M_w , and μ_w are the liquid water density, molecular weight, and viscosity, respectively. K_l^{MEM} is the liquid relative permeability of the membrane. The electro-osmotic drag coefficient, n , is expressed by ³²

$$n = \frac{2.5}{22} \lambda \quad [5.3]$$

In Eq. 5.3, the water content in the membrane, λ , is of the form

$$\lambda = \frac{C_w^N}{C_f} \quad [5.4]$$

where C_w^N and C_f are the water content in the Nafion phase and the fixed charge concentration, respectively.

The liquid water pressure gradient across the membrane was treated as constant.³³

$$\frac{d^2 p_l}{dx^2} = 0 \quad [5.5]$$

The liquid pressure in the GDL, MPL, and CL were calculated using the capillary pressure correlations for these porous media.

Table 5.1 Governing equations.

| Variables | GDL | MPL | CL | MEM* |
|-------------|----------------------------------|----------------------------------|------------------------------------------------|----------------------------|
| $C_{O_2}^g$ | $-\frac{dN_{O_2}^g}{dx} = 0$ | $-\frac{dN_{O_2}^g}{dx} = 0$ | $-\frac{dN_{O_2}^g}{dx} - R_{O_2} = 0$ | $C_{O_2}^g = 0$ |
| C_v^g | $-\frac{dN_v^g}{dx} - R_w^c = 0$ | $-\frac{dN_v^g}{dx} - R_w^c = 0$ | $-\frac{dN_v^g}{dx} - R_w^c = 0$ | $C_v^g = 0$ |
| ϕ_+ | N/A | N/A | $-\frac{di_+}{dx} - 4FR_{O_2} = 0$ | $-\frac{di_+}{dx} = 0$ |
| s_{GDL} | $-\frac{dN_w}{dx} + R_w^c = 0$ | N/A | N/A | N/A |
| s_{MPL} | N/A | $-\frac{dN_w}{dx} + R_w^c = 0$ | N/A | N/A |
| s_{CL} | N/A | N/A | $-\frac{dN_w}{dx} + (4n+2)R_{O_2} + R_w^c = 0$ | N/A |
| C_w^N | N/A | N/A | $-\frac{dC_w^N}{dx} = 0$ | $-\frac{dN_w^N}{dx} = 0$ |
| p_l | $p_l = p_g - p_c$ | $p_l = p_g - p_c$ | $p_l = p_g - p_c$ | $\frac{d^2 p_l}{dx^2} = 0$ |

5.2.3 Boundary Conditions

Table 5.2 lists the boundary conditions used in this model. The position at $x=0$ is the gas channel/GDL interface, and $x=L$ denotes the membrane/anode interface as shown in Fig. 5.2. At the GDL/MPL and MPL/CL interfaces, the capillary pressures are set equal to satisfy the force balance besides the liquid water flux continuity. A saturation level jump condition occurs at these interfaces if the adjacent materials have different wetting properties. This condition is experimentally demonstrated in Chapter 4 Fig. 4.2 for the case of two porous beds consisting of packed porous materials of different wetting properties.

The flux continuities were set at the inner boundaries. The liquid pressure was calculated at the inner boundaries using the obtained saturation level at that point. The liquid pressures at the channel/cathode GDL and the membrane/anode interfaces were fixed at 1 atm. At the CL/MEM interface, the liquid water flux in the CL, consisting of the liquid pressure-gradient-driven transport term, is set equal to the flux in the membrane consisting of the concentration-gradient-driven diffusion term and a similar liquid pressure-gradient-driven permeation term ($N_w^N|_{MEM}^{C,P}$). The electro-osmotic drag part of the water flux was assumed to be released inside the CL as the oxygen reduction reaction occurs.

$$N_w|_{CL} = N_w^N|_{MEM}^{C,P} \quad [5.6]$$

As shown in Chapter 4, the capillary pressure is defined as

$$p_c = p_g - p_l \quad [5.7]$$

where p_g and p_l are the gas phase pressure and liquid phase pressure, respectively. The liquid permeability is a correlation of the liquid saturation level³¹

$$K_w^{CL} = K_{w,0}^{CL} s^{4.5} \quad [5.8]$$

where K_w^{CL} is the liquid relative permeability of CL; $K_{w,0}^{CL}$ is the absolute permeability of CL; and s is the saturation level.

From Darcy's law, the left side of Eq. 5.6, $N_w|_{CL}$, is expressed by²⁷

$$N_w|_{CL} = -\frac{\rho_w}{M_w} \frac{K_w^{CL}}{\mu_w} \frac{dp_l}{dx} \quad [5.9]$$

By substituting Eqs.5.7 and 5.8 into Eq. 5.9, the following equation is obtained

$$N_w|_{CL} = \frac{\rho_w}{M_w} \frac{K_{w,0}^{CL}}{\mu_w} s^{4.5} \frac{dp_c}{ds} \frac{ds}{dx} \quad [5.10]$$

$N_w^N|_{MEM}^{C,P}$ consists of the concentration-gradient-driven diffusion and pressure-gradient-driven permeation terms of Eq. 5.2. Substitute the expression of

$N_w|_{CL}$ (Eq. 5.10) and $N_w^N|_{MEM}^{C,P}$ into Eq. 5.6, the following equation is obtained

$$\frac{\rho_w}{M_w} \frac{K_{w,0}^{CL}}{\mu_w} \frac{dp_c}{ds} s^{4.5} \frac{ds}{dx} = -D_w^N \frac{dC_w^N}{dx} - \frac{\rho_w}{M_w} \frac{K_l^{MEM}}{\mu_w} \frac{dp_l}{dx} \quad [5.11]$$

where p_c is expressed by Eq. 5.1.

Fully saturated air feed is used in this study. In this 1-D simulation, the anode channel is fixed at the inlet condition to accelerate the computation speed. To address

the changes in the gas phase along the anode channel, a 2-D model will be needed.

Table 5.2 Boundary conditions.

| Variables | $x=0$ | GDL/MPL | MPL/CL | CL/MEM | $x=L$ |
|-------------|-------------------------------|---------------------------------------|--------------------------------------|---------------------------------|-------------------------------|
| $C_{O_2}^g$ | $C_{O_2}^g = C_{O_2}^{g,air}$ | $N_{O_2}^g _{GDL} = N_{O_2}^g _{MPL}$ | $N_{O_2}^g _{MPL} = N_{O_2}^g _{CL}$ | $N_{O_2}^g _{CL} = 0$ | $C_{O_2}^g = 0$ |
| C_v^g | $C_v^g = C_v^{g,air}$ | $N_v^g _{GDL} = N_v^g _{MPL}$ | $N_v^g _{MPL} = N_v^g _{CL}$ | $N_v^g _{CL} = 0$ | $C_v^g = 0$ |
| ϕ_+ | N/A | N/A | $i_+ _{CL} = 0$ | $i_+ _{CL} = i_+ _{MEM}$ | $\phi_+ = 0$ |
| s_{GDL} | $p_{c,GDL} = 0$ | $N_w _{GDL} = N_w _{MPL}$ | N/A | N/A | N/A |
| s_{MPL} | N/A | $p_{c,GDL} = p_{c,MPL}$ | $N_w _{MPL} = N_w _{CL}$ | N/A | N/A |
| s_{CL} | N/A | N/A | $p_{c,MPL} = p_{c,CL}$ | $N_w _{CL} = N_w^{C,P} _{MEM}$ | N/A |
| C_w^N | N/A | N/A | $N_w^N _{CL} = 0$ | $C_w^N = C_w^{N,eq} _{cathode}$ | $C_w^N = C_w^{N,eq} _{anode}$ |
| p_l | $p_l = p_g = latm$ | $p_l = p_g - p_c$ | $p_l = p_g - p_c$ | $p_l = p_g - p_c$ | $p_l = p_g = latm$ |

5.2.4 Parameters and Correlations Used in the Simulation

Table 5.3 lists the parameters used in the simulation. Parameters and correlations that are the same as those used in reference 27 are not listed here. Table 5.4 summarizes the simulation conditions.

Table 5.3 Parameters.

| | | |
|---------------------------------------------------------|--|------------------------------------|
| GDL properties | | |
| Porosity, ²⁷ ε_{GDL} | | 0.5 |
| Thickness, ²⁷ δ_{GDL} | | 230 μm |
| Absolute liquid water permeability, $K_{w,0}^{GDL}$ | | $1.0 \times 10^{-10} \text{ cm}^2$ |
| MPL properties | | |
| Porosity, ε_{MPL} | | 0.3 |
| Thickness, δ_{MPL} | | 20 μm |
| Absolute liquid water permeability, $K_{w,0}^{MPL}$ | | $1.0 \times 10^{-12} \text{ cm}^2$ |
| CL properties | | |
| Porosity, ²⁷ ε_{CL} | | 0.12 |
| Thickness, ²⁷ δ_{CL} | | 16 μm |
| Absolute liquid water permeability, $K_{w,0}^{CL}$ | | $5.0 \times 10^{-13} \text{ cm}^2$ |
| Membrane properties | | |
| Thickness, ²⁷ δ_{MEM} | | 50 μm |
| Membrane liquid permeability, ³⁴ K_l^{MEM} | | $1.8 \times 10^{-14} \text{ cm}^2$ |

Table 5.4 Simulation conditions.

| | |
|---------------------------|-------|
| Temperature, T | 60 °C |
| Pressure, P | 1 atm |
| Humidity of the air inlet | 100% |
| Humidity at anode | 100% |
| Stoichiometry of air | 2 |

5.3 Results and Discussion

The effects of the presence of an MPL in the cathode of a PEM fuel cell will be investigated first. Next, the effects of the MPL capillary property on the saturation levels, the liquid pressure, the liquid water fluxes in the modeled domain, and the PEM fuel cell performance will be studied to elucidate the preferred water management strategy in a PEM fuel cell. The hydrophobicity of the MPL was adjusted by changing the values and shapes of the capillary curves.

5.3.1 With and Without MPL

Fig. 5.3 shows the capillary curves of the GDL (G1), MPL (M1), and CL (C1) used in this model.

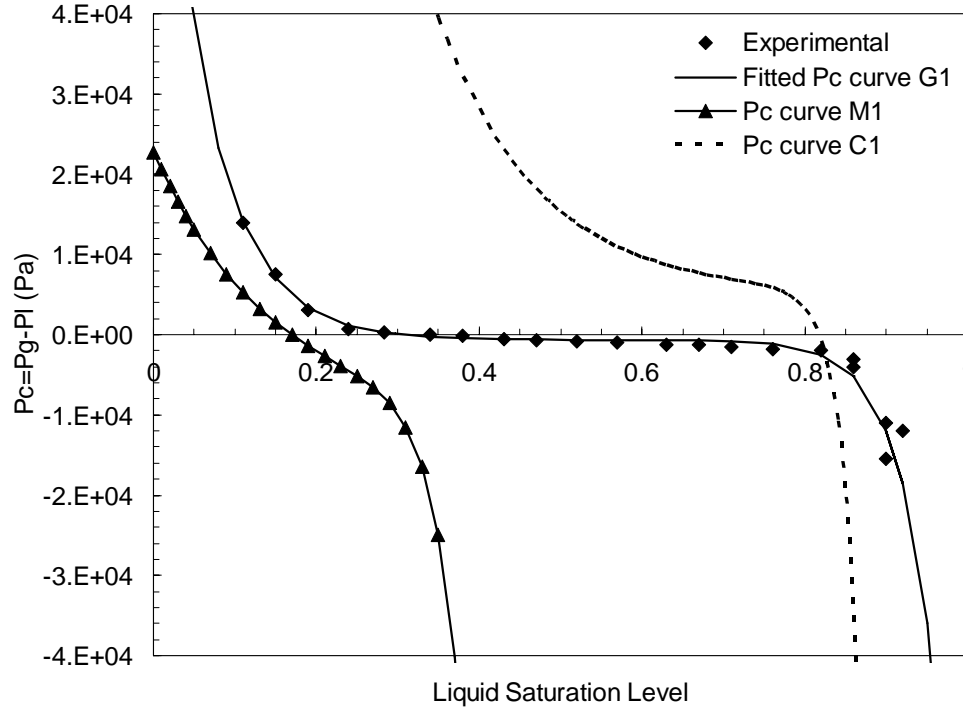


Figure 5.3 Capillary curves used in the case with and without the MPL. The fitting parameters of a_1 , a_2 , b , c , and d are -22.7, -16.2, -644.9, 0.58, -7.6 for G1, -30.0, -7.0, -9878.4, 0.3, -4000.0 for M1, and -45.0, -8.0, 5000.0, 0.78, -1106.56 for C1, respectively.

Profiles of the simulated saturation levels and liquid differential pressure in the modeled domain using the capillary curves in Fig. 5.3 are shown in Fig. 5.4. For the case with MPL, G1, M1, and C1 are used for the GDL, MPL, and CL, respectively; for the case without MPL, only G1 and C1 are used for the GDL and CL, respectively. Fig. 5.4 (a) shows that the MPL increases the saturation levels in the CL and decreases the saturation levels in the GDL. In the MPL, the low permeability causes steep saturation profiles close to the GDL/MPL interface. The hydrophobic MPL

forces liquid water from the cathode side back to the anode side, resulting in lower saturation levels in the GDL and higher saturation levels in the CL. Note that the liquid water saturation jump condition at the GDL/MPL and MPL/CL interfaces is captured in this model. Fig. 5.4 (b) also shows that the MPL raises the liquid pressure in the CL to a very high level. The much higher liquid pressure gradient across the membrane created with the MPL significantly increases the pressure permeation rate of liquid water from the cathode back to the anode.

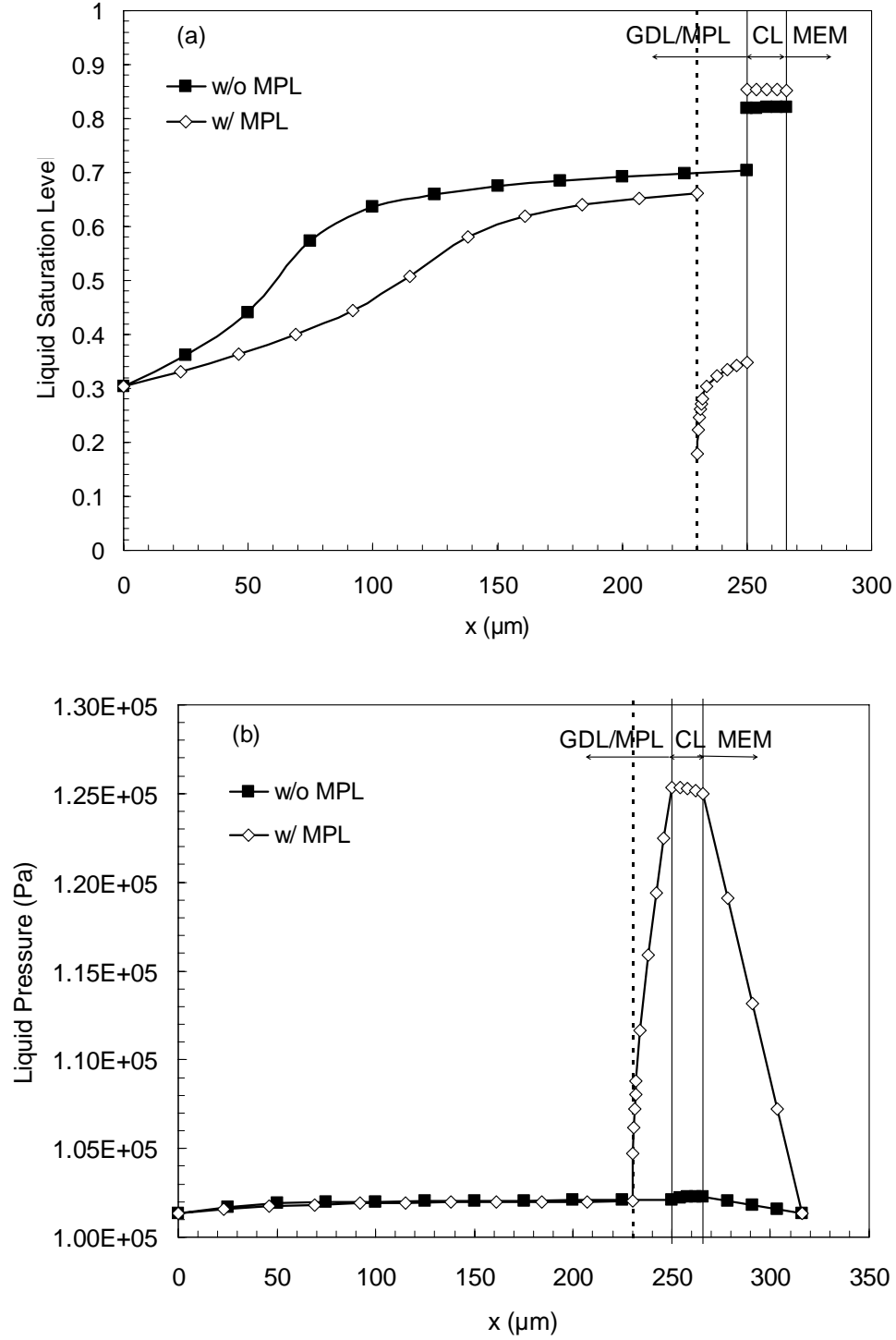
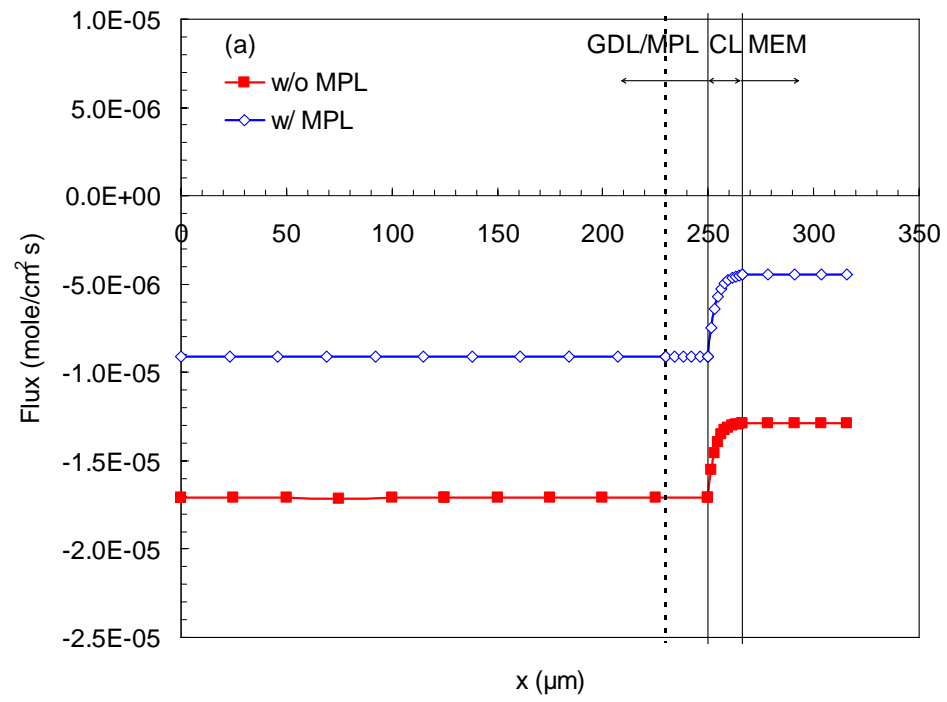


Figure 5.4 (a) Liquid water saturation level, and (b) liquid pressure at 0.6V. G1, M1, and C1 were used in the case with the MPL; G1 and C1 were used in the case without the MPL (Refer to Fig. 5.3).

Fig. 5.5 (a) shows the liquid water fluxes in the modeled domain. The negative sign means liquid water is transported from the anode to the cathode or opposite to the x-direction as shown in Fig. 5.2. Note that the application of an MPL in the cathode side reduces the flux of liquid water transport from the cathode CL to the cathode GDL, as well as the net water flux across the membrane from the anode side to the cathode side. The water flux in the GDL of the case with the MPL ($-0.913\text{E-}5$ mole/(cm² s)) is about half of that without the MPL ($-1.71\text{E-}5$ mole/(cm² s)). The electro-osmotic drag effect is mitigated by the pressure driven permeation resulting from the liquid pressure gradient across the membrane. The liquid water fluxes in the GDL and MPL are identical when saturated cathode gases are used in the model since the effect of water evaporation is eliminated.

Fig. 5.5 (b) and (c) show the flux profiles of each component of the cases without MPL and with MPL, respectively. Note that the water flux in the membrane by concentration-driven diffusion is zero because of the saturated anode and cathode feed condition used in this model. Note also that the pressure driven permeation rate of water in the membrane increases greatly by the application of the MPL. The increased water permeation rate in the membrane leads to lower saturation levels in the GDL at the cathode side (See Fig. 5.4 (a)) and faster transport of gaseous reactant

to the reactive catalyst sites.



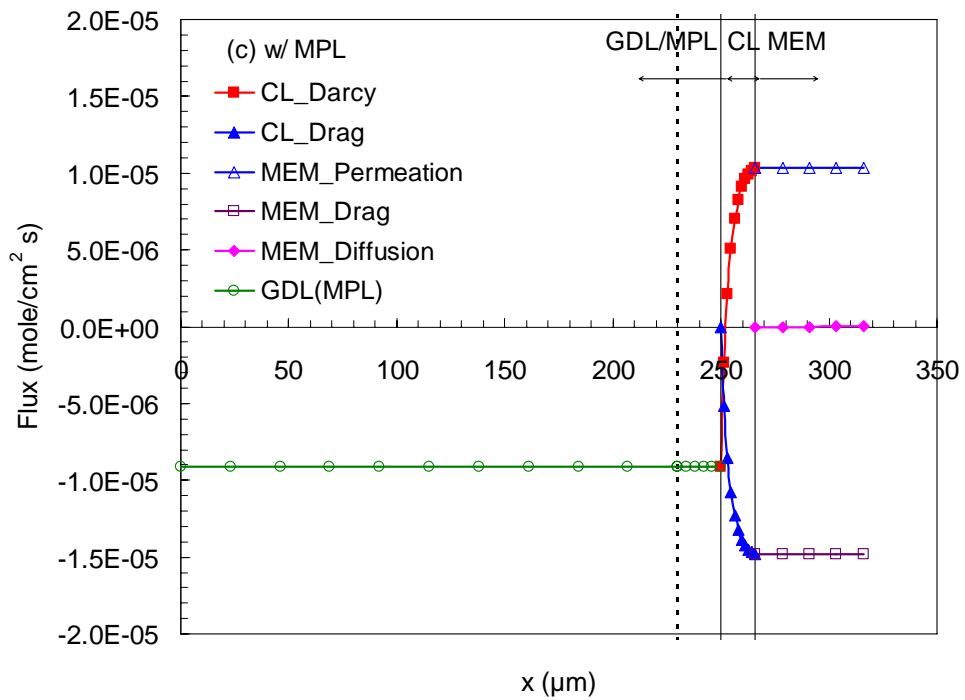
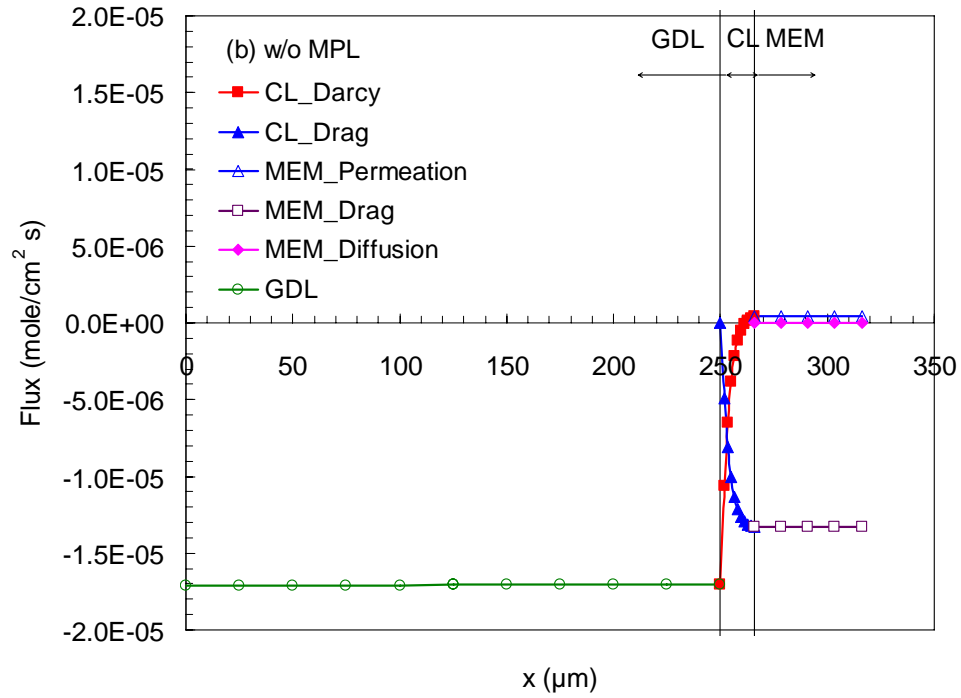


Figure 5.5 (a) Net liquid water fluxes, (b) liquid water fluxes of each component for the case without MPL, and (c) liquid water fluxes of each component for the case with MPL at 0.6V. G1, M1, and C1 were used in the case with the MPL; G1 and C1

were used in the case without the MPL (Refer to Fig. 5.3).

The liquid water fluxes versus current density are plotted in Fig. 5.6. As stated earlier, the water fluxes in the GDL and the MPL are equal because of the saturated feed air condition used in the cathode side. Only the liquid water fluxes in the GDL and membrane are shown in Fig. 5.6.

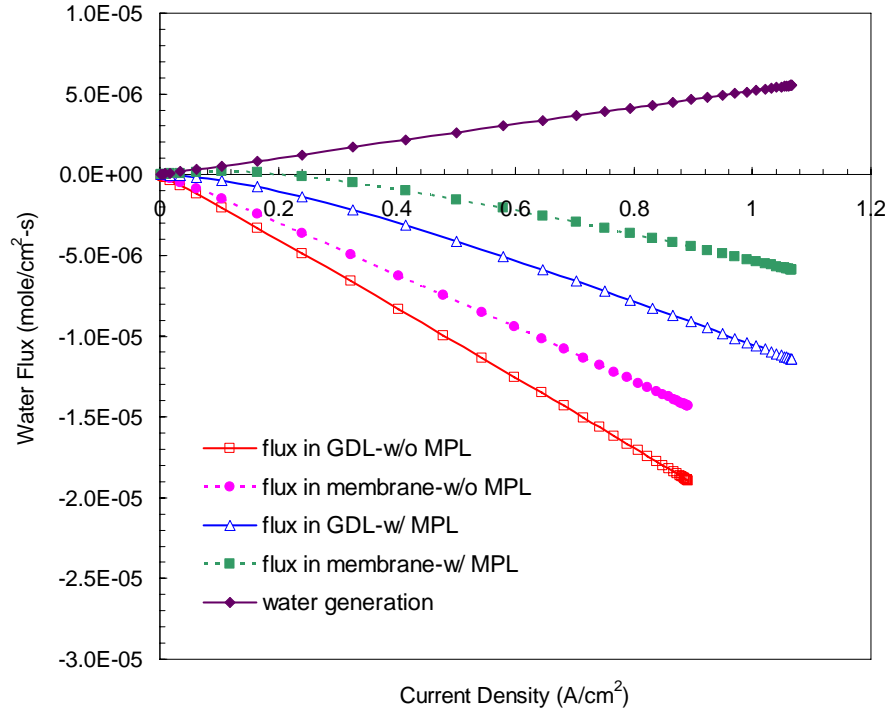


Figure 5.6 Water fluxes in the simulated domain at 0.6V. G1, M1, and C1 were used in the case with the MPL; G1 and C1 were used in the case without the MPL (Refer to Fig. 5.3).

First, Fig. 5.6 shows that for both cases, with and without the MPL, liquid water is

transported from the anode side to the cathode side (negative sign) over most of the current density range. This leads to the need of humidification of the fuel in the anode side and water removal at the cathode side. The only exception is the case with the MPL at low current density ($<0.2 \text{ A/cm}^2$), where liquid water is transported from the cathode side to the anode side (positive sign). The water fluxes in the GDL and membrane increase with the current density because of increased water generation rate and electro-osmosis rate at high current density. Second, it is seen from Fig. 5.6 that the MPL prevents liquid water from being transported from the CL to the cathode GDL, which leads to lower liquid water flux in the GDL. When the electro-osmotic flux of water from the anode to the cathode is higher than the back-transport flux (e.g., at high current density), the net liquid water flux in the membrane is negative (from the anode to the cathode). Otherwise (at low current density), the direction of liquid water flux in the membrane is reversed. The fact that the liquid water flux in the membrane in the case with MPL is still negative at high current density means that the MPL used in the base case, M1, is not hydrophobic enough to meet the goal of non-humidified anode feed.

As more water is driven back to the anode, liquid water saturation level in the cathode GDL is reduced. However, when the hydrophobic MPL forces liquid water back to the anode, it also causes the cathode CL saturation level to increase. A more

saturated CL may limit the gas transport rate to the catalyst sites by reducing the gas porosity and creating a thicker liquid water diffusion barrier on the catalyst sites. Note that the CL used in this study is treated with a hydrophobic phase to provide continuous gas transport pathways through the CL, even at very high liquid saturation level. The simulated fuel cell performance is shown in Fig. 5.7. The fuel cell with the MPL on the cathode side has better fuel cell performance than that without the MPL.

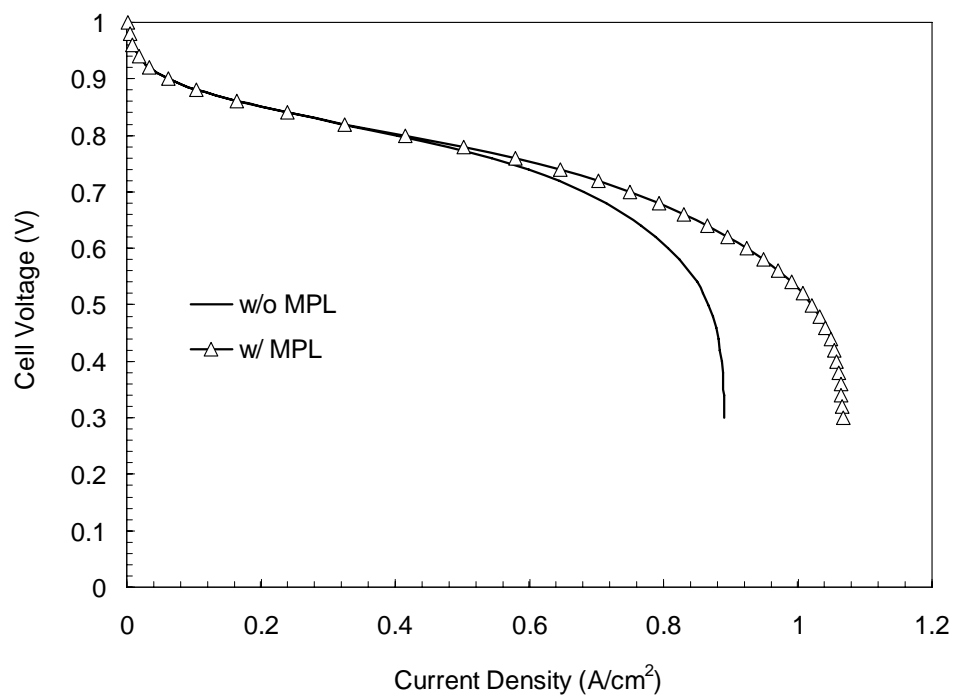


Figure 5.7 Fuel cell performance. G1, M1, and C1 were used in the case with the MPL; G1 and C1 were used in the case without the MPL (Refer to Fig. 5.3).

5.3.2 Capillary Effect of the MPL

To fully investigate the effect of the MPL on the performance of a PEM fuel cell, various capillary curves in Fig. 5.8 are simulated to help determine what type of MPL will be needed to achieve the goal of zero-net-water-transport-across-the-membrane. G1, M1 and C1 are the same as those in Fig. 5.3. The capillary curves for the GDL and CL are fixed to be G1 and C1, respectively; M1, M2 and M3 with different capillary properties are used for the MPLs. As shown in Fig. 5.8, M2 is the most hydrophobic MPL while M3 is the most hydrophilic MPL. In Chapter 4, we have investigated the effect of shifting the capillary pressure curves in multiple ways, including shifting the capillary curve up, down, left, right, and higher and lower slopes. Note that the capillary curve of a porous medium can be made hydrophobic in such a way as to shift it downward (i.e., into the negative capillary pressure region) by changing the wetting property of the substrate surface, and to shift leftward by introducing a porous hydrophobic phase into its pores. In this study, we will consider only shifting the MPL capillary pressure curve left/right and making the slope in the hydrophobic region steeper. We believe this could be achieved by adjusting the PTFE content in the MPL.

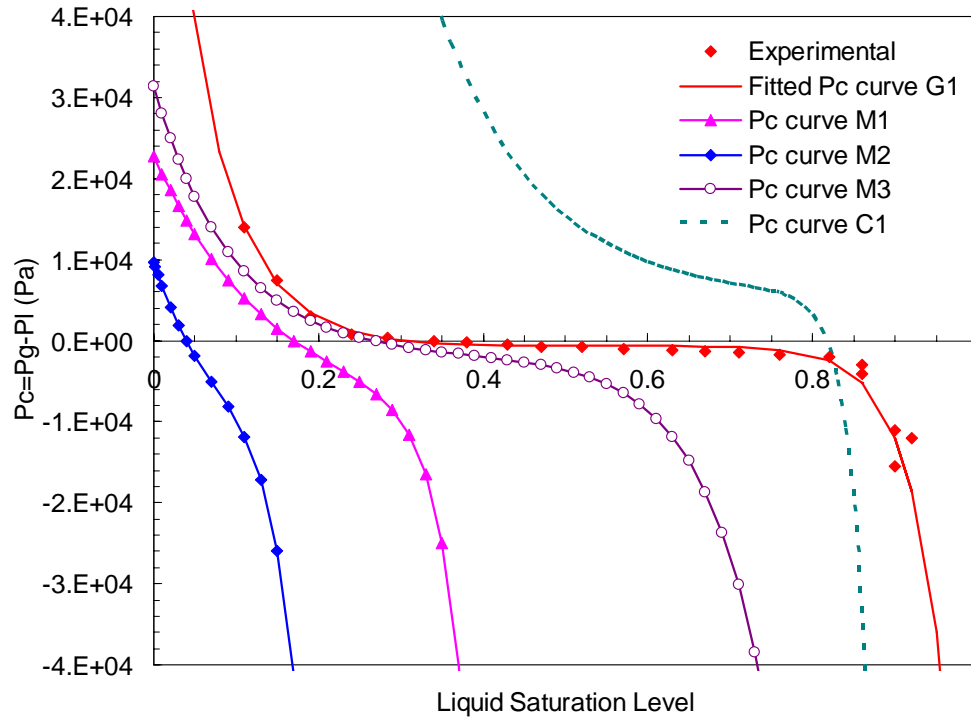
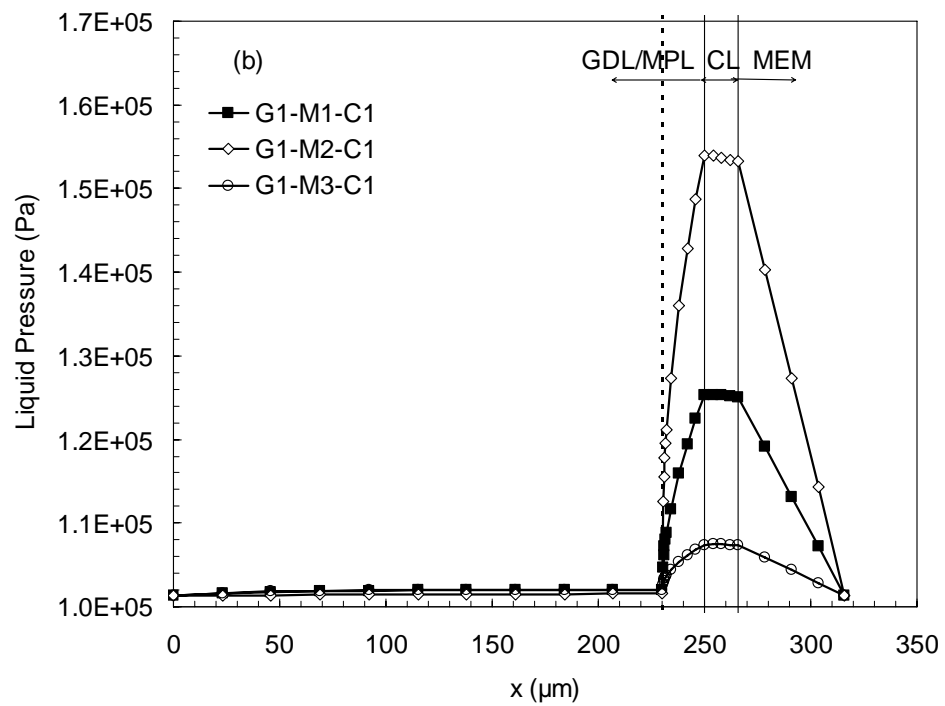
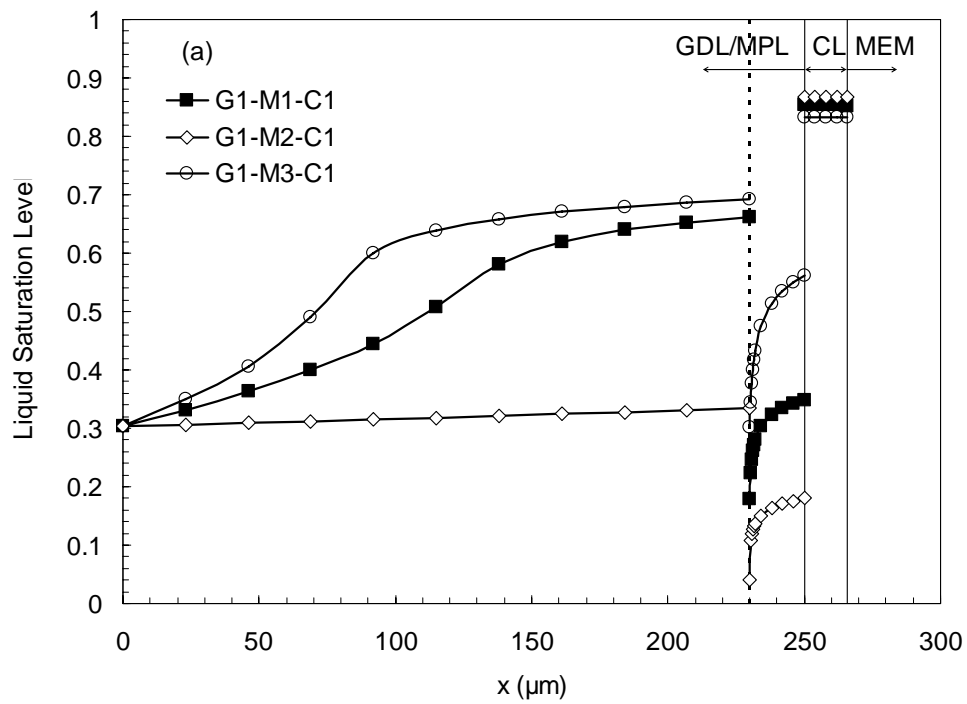


Figure 5.8 Capillary curves used in the study of MPL capillary effect. The fitting parameters of a_1 , a_2 , b , c , and d are -30.0, -16.0, -9878.4, 0.1, -4000.0 for M2, -13.0, -10.5, -2000.0, 0.4, -500.0 for M3, respectively. G1, M1, and C1 are the same as those in Fig. 5.3.

The simulated liquid water saturation levels, liquid pressure, and liquid water flux are plotted in Fig. 5.9. The results show that the most hydrophobic MPL, M2, results in the lowest saturation levels in the GDL and MPL and the highest saturation levels in the CL. However, the differences in the saturation levels in the CL are very small because of the steep slope of the CL capillary curve in the hydrophobic region. The most hydrophilic MPL, M3, leads to the opposite trend, with the highest saturation levels in the GDL and MPL and the lowest saturation levels in the CL. The

most hydrophobic MPL, M2, raises the liquid pressure at the CL/membrane interface to the highest level. And consequently, the liquid water flux resulting from capillary pressure driven permeation is so high that it overcomes the electro-osmotic flux, which leads to positive water flux (from the cathode to the anode) in the membrane. Note that if the anode feed gas is unsaturated with water vapor, this positive flux of water could be used to reduce the anode humidification requirement. For the less hydrophobic MPLs, M1 and M3, liquid water fluxes in the GDL (MPL) and membrane are always negative (from the anode to the cathode). This implies that when M1 and M3 are used, anode humidification and cathode water removal are required in order to obtain optimal fuel cell performance.



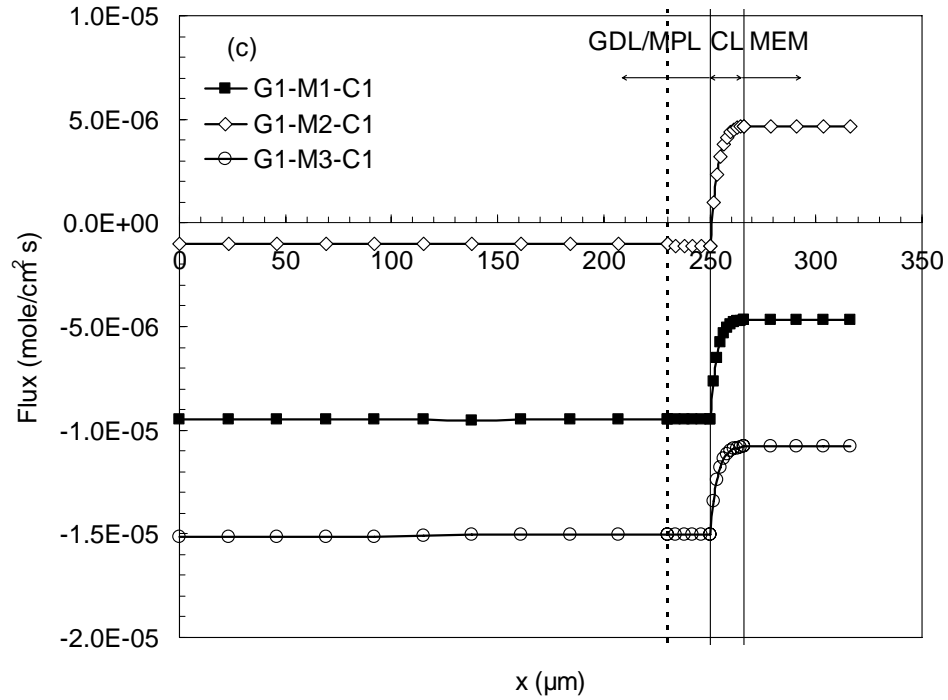


Figure 5.9 MPL capillary effects on (a) the liquid water saturation level, (b) liquid pressure, and (c) liquid water flux at 0.6V (Refer to Fig. 5.8).

The effects of the MPL on the liquid water fluxes at various current densities are shown in Fig. 5.10. The results show that the hydrophobicity of the MPL directly affects the liquid water flux in the membrane. On one hand, for the three MPL capillary curves selected in this study, the most hydrophilic one, M3, results in the highest negative liquid water flux in the membrane (from the anode to the cathode). The low liquid pressure associated with low hydrophobicity of the MPL does not promote the permeation of liquid water from the cathode to the anode. On the other hand, the most hydrophobic MPL, M2, leads to positive liquid water flux (from the

cathode to the anode) in the membrane over the whole current density range shown in Fig. 10. Note that although cathode GDL flooding is reduced, anode flooding could occur in this case (as observed by Lin in his fuel cell experiment).¹⁷

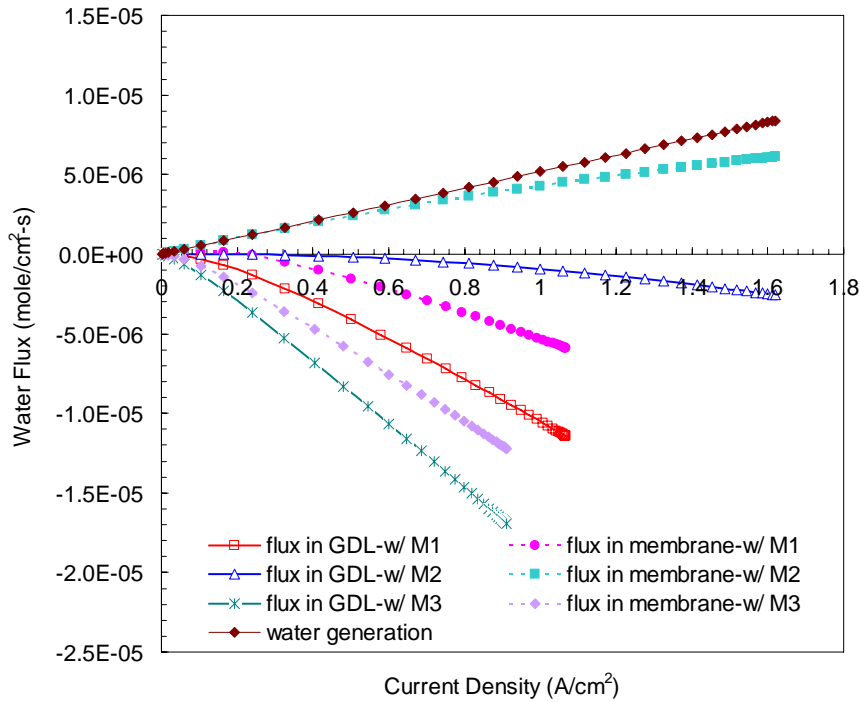


Figure 5.10 MPL capillary effects on the water fluxes at 0.6V. Capillary curves of the GDL and CL were fixed to be G1 and C1, respectively (Refer to Fig. 5.8).

The fuel cell performance in Fig. 5.11 shows that there are very small differences at high voltages (above 0.7V). This is to be expected, because at these high voltages and low current densities the fuel cell is not operating in a mass transport limiting region. At low voltages (below 0.7V) and high current densities, the

hydrophobic MPL greatly improves the PEM fuel cell performance. The most hydrophobic MPL, M2, leads to the best fuel cell performance, showing that the advantage resulted from a less flooded cathode GDL overcomes the disadvantage of a more flooded cathode CL.

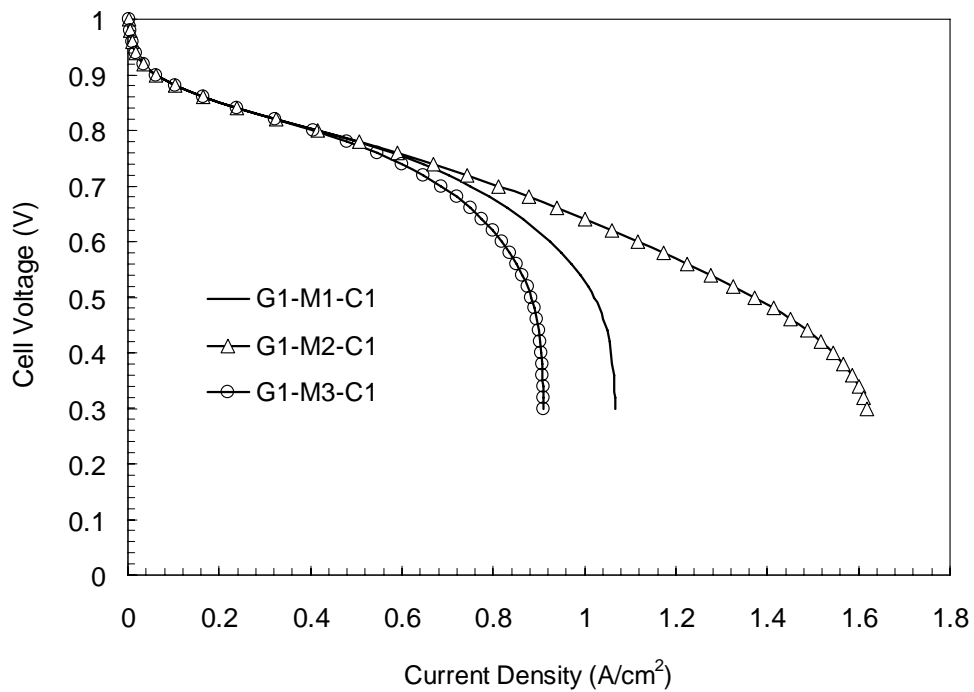


Figure 5.11 MPL capillary effects on the fuel cell performances (Refer to Fig. 5.8).

5.3.3 Preferred Combination of the GDL, MPL and CL

It is seen from the above case studies that the MPL improves the fuel cell performance by forcing liquid water generated at the cathode to the anode to reduce

the flooding condition at the cathode. The more hydrophobic is the MPL, the better the fuel cell performance is obtained. In the following discussion, a case with a super hydrophobic GDL is investigated. This case will be compared to the previous best case, G1-M2-C1. We define a super hydrophobic GDL as a GDL with high hydrophobicity and permeability. However, although it is not shown here, it is found that within the range used in the model the liquid permeability of the GDL has a minor impact on the fuel cell performance, because the saturation level in the GDL is significantly reduced when an MPL is used. Thus, in this case, a GDL with the same liquid permeability but more hydrophobic capillary pressure (shifted both leftward and downward) is used. The capillary curves used are plotted in Fig. 5.12.

The conventional way to make a hydrophobic GDL is to add PTFE into the porous medium. The problem is, since PTFE is a pore filling solid, when the amount of PTFE increases, the pore volume decreases, leading to lower gas permeability. Thus, it is impossible to make highly hydrophobic GDLs without negatively impeding the gas transport properties of the porous media by the conventional method. If the surface of the pores in a GDL can also be modified without negatively affecting the porosity in a novel way, highly hydrophobic GDLs with high gas permeability and capillary pressure curves with shapes and values as assumed here are possible. Experimental details on how a super hydrophobic GDL can be obtained will be

discussed in the future. Capillary curves, G1 and G2, in Fig. 5.12 represent the GDLs modified with the conventional and novel methods, respectively.

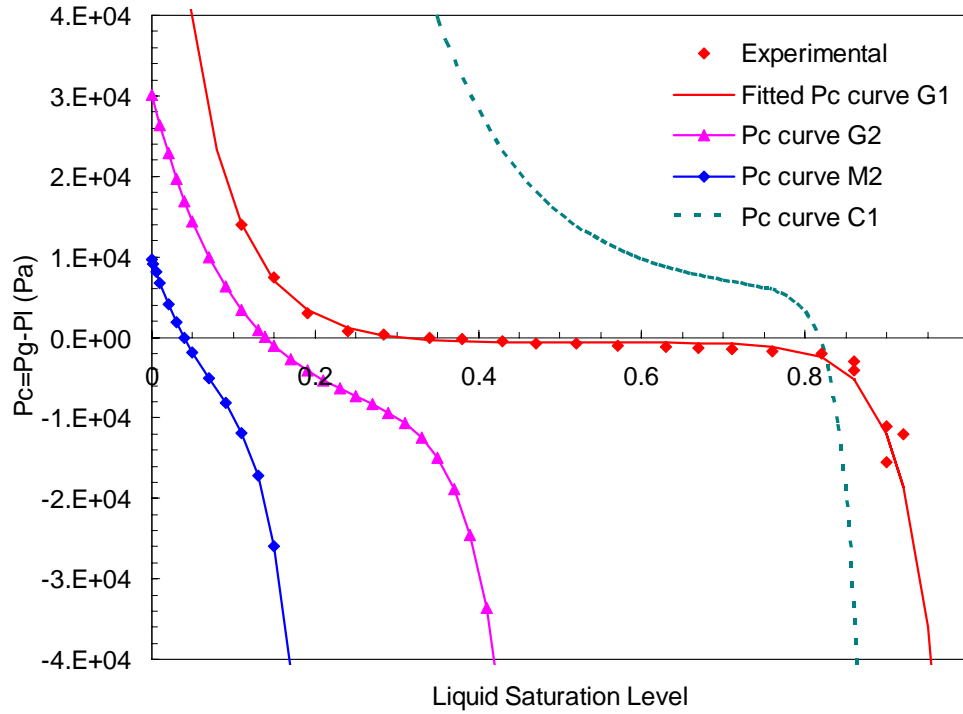
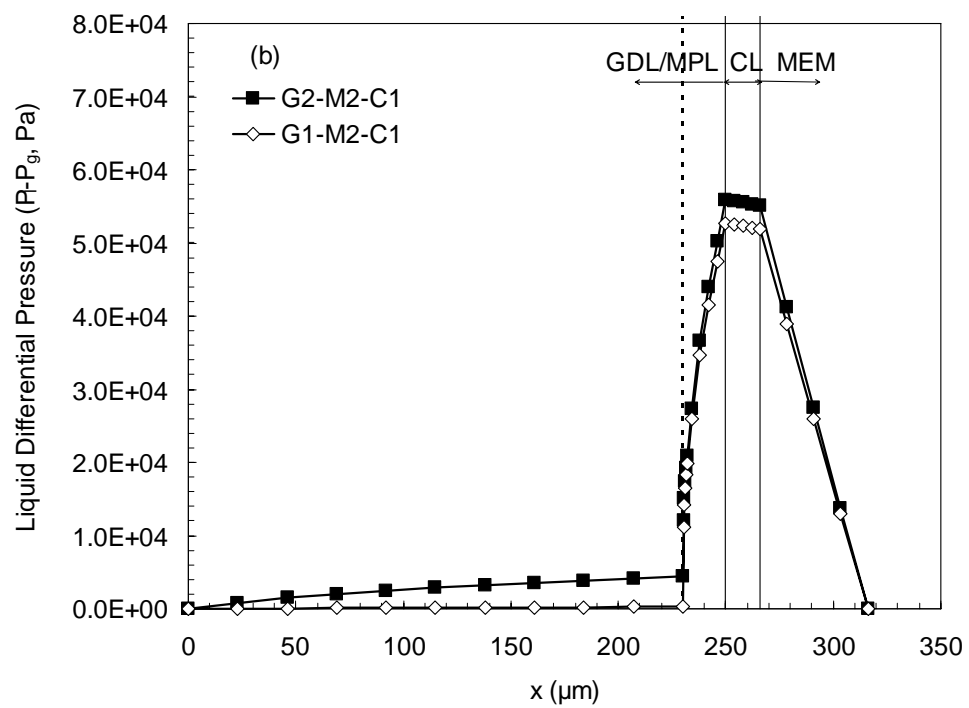
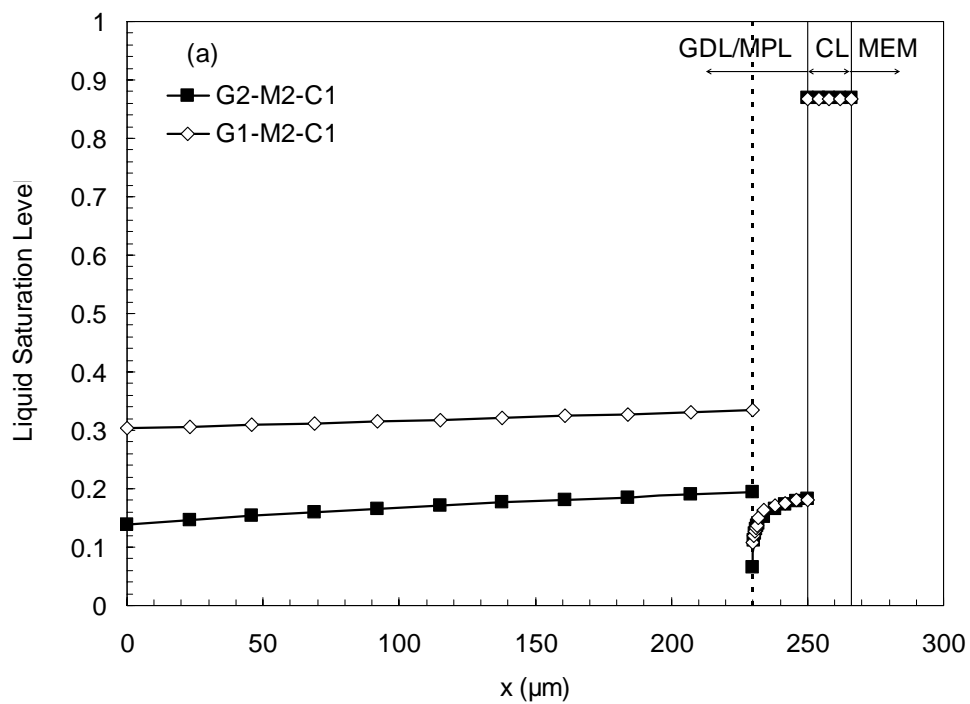


Figure 5.12 Capillary curves used in the preferred combinations. The fitting parameters of a_1 , a_2 , b , c , and d are -22.7, -10.0, -10000.0, 0.3, -2000.0, respectively, for G2. G1, M2, and C1 are the same as in Fig. 5.8.

The saturation level, liquid pressure, and liquid water flux are plotted in Fig. 5.13. First, the saturation levels in the GDLs are more uniform than those in the MPL because of the higher permeability of the GDLs (G1 and G2) as compared to those of the MPL and CL used in this model. The steep slope of the capillary curve of the CL in the hydrophobic region confines the saturation levels in the CL to a narrow region.

Second, the saturation levels and liquid pressure in the MPL and CL for the two cases, G1-M2-C1 and G2-M2-C1, are very close because the same MPL and CL are used in these cases. Little liquid water flux in the GDL (MPL) was observed when the MPLs were used, because the hydrophobic MPL prevents liquid water from transporting out of the cathode CL, as demonstrated in the previous cases. Fig. 5.13 (c) shows that the water fluxes are negative (from anode to cathode) in the GDL (MPL) and positive (from cathode to anode) in the membrane, respectively. Thus, water is removed from the cathode side by two processes: liquid water transport out of the cathode through the CL, MPL and GDL on the cathode side and by back permeation to the anode. The water fluxes in the GDL and membrane of the two cases are very close, showing that the more hydrophobic GDL, G2, does not force much more liquid water from the cathode to the anode. However, the less saturated GDL (G2) is more accessible and provides faster oxygen gas transport to the catalyst layer.



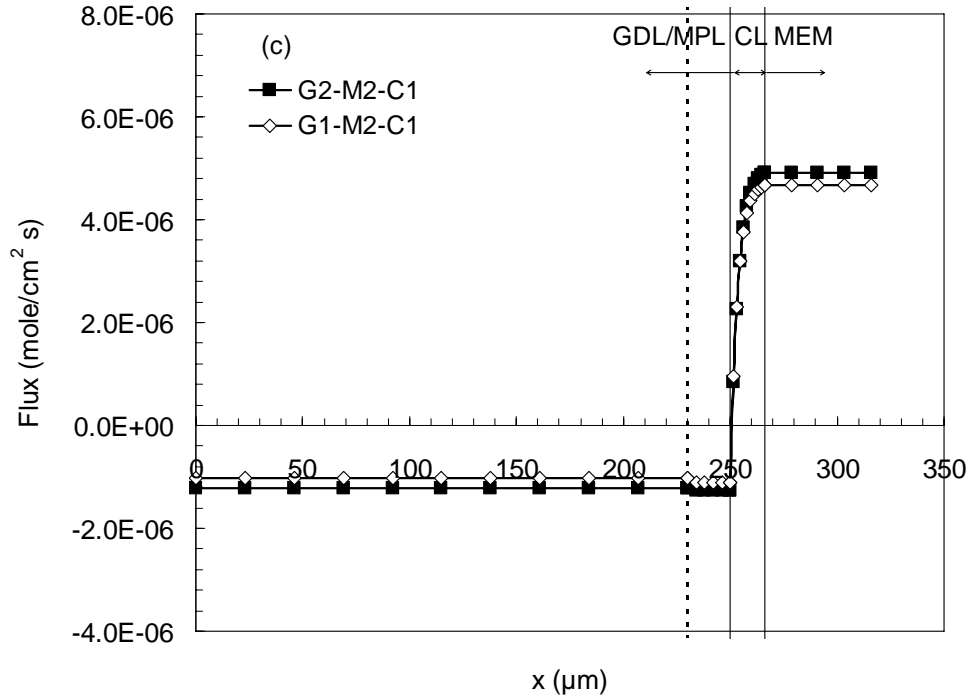


Figure 5.13 (a) Liquid water saturation levels, (b) liquid pressure, and (c) liquid water fluxes at 0.6V (Refer to Fig. 5.12).

It is seen from Fig. 5.14 that the case with the super hydrophobic GDL, G2-M2-C1, shows better fuel cell performance than the case in which a less hydrophobic GDL is used (G1-M2-C1). When the results in Fig. 5.14 are compared to those in Fig. 5.11, one should note that the cell performance increases much more when a more hydrophobic MPL is used (Fig. 5.11) than when a more hydrophobic GDL is used (Fig. 5.14). This shows that having a more hydrophobic MPL is more important than having a more hydrophobic GDL. The reason is that a more hydrophobic MPL further raises the liquid water pressure in the cathode which drives

more water to the anode, resulting in even less water leaving the cathode through the cathode GDL. A more hydrophobic GDL (lower saturation level at $P_c=0$ and higher capillary pressure versus saturation level slope in the hydrophobic region) reduces the saturation level in the GDL and increases the capillary diffusion rate of water out of the cathode GDL. One deals with the source while the other deals with the process. Clearly, reducing the amount of water going out of the cathode has a more significant impact than the rate at which water is removed from the cathode.

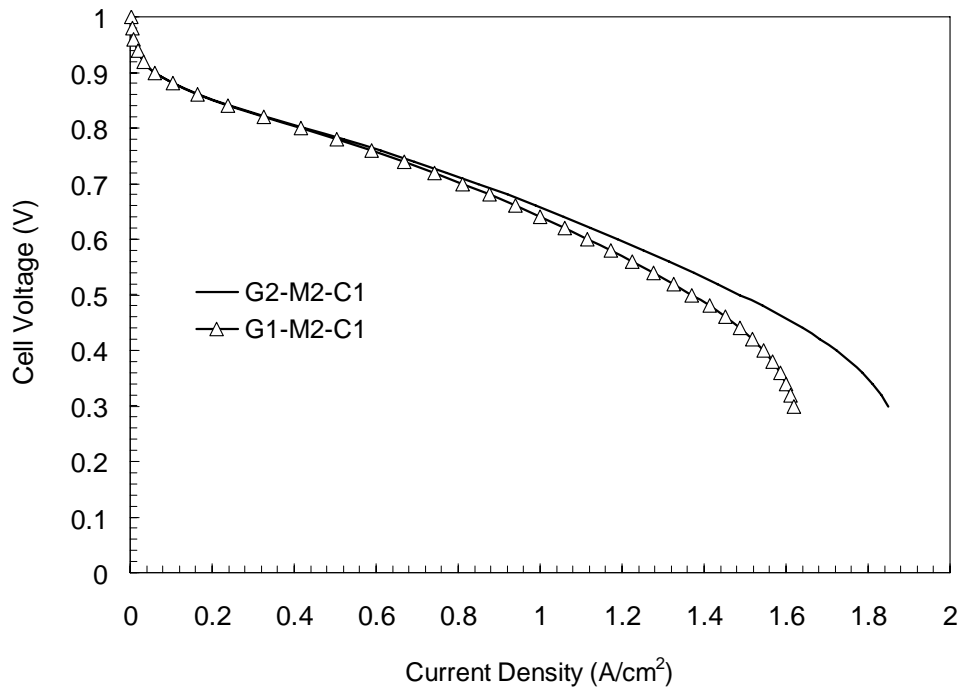


Figure 5.14 GDL effects on the fuel cell performances (Refer to Fig. 5.12).

5.4 Conclusions

This study helps to explain the mechanism by which the performance of a PEM fuel cell is improved by adding an MPL between the GDL and the CL in the cathode side. Note that the additional benefit of having better electrical contact between the CL and GDL is recognized but not included here. The MPL, due to its high hydrophobicity, partially blocks the liquid water generated in the CL from transporting out to the cathode GDL, resulting in higher saturation level in the CL and lower saturation level in the GDL. Correspondingly, the MPL increases the liquid water pressure in the cathode to the levels much higher than those in the anode, leading to an increased net back-transport rate of liquid water from the cathode to the anode. This increased back-transport rate of liquid water reduces the liquid water removal rate from the CL to the cathode GDL, as well as the net liquid water transport rate from the anode to the cathode by electro-osmosis. As a result, the liquid water saturation levels in the GDL are reduced, and consequently, higher oxygen gas transport rate to the catalyst sites in the CL in the cathode is achieved. It should be noted that higher liquid water pressure created by the use of an MPL could also lead to high liquid water saturation level in the catalyst layer unless this layer is treated with a hydrophobic material to create gas transport pathways for oxygen. The CL used in this study is assumed to have this property.

The results also show that the more hydrophobic the MPL is, the higher liquid water pressure increases, and consequently, the higher driving force is created across the membrane to drive liquid water from the cathode to the anode. The back-transport of liquid water from the cathode to the anode mitigates the requirement of water addition at the anode side and water removal at the cathode side. Zero-net-water-transport-across-the-membrane could be achieved by using an appropriate MPL. The liquid water saturation level at $p_c=0$ ($p_c=p_g-p_l$) and the slope of the hydrophobic region of the capillary curve are identified as two most important variables. To minimize cathode flooding and to promote water transport from the cathode to the anode, low liquid saturation level at $p_c=0$ and high slope in the hydrophobic region are desirable. This study also shows that a highly hydrophobic GDL that can maintain high permeability could lead to even better fuel cell performance. Finally, even though the effect of the membrane liquid permeability was not investigated it is expected to be an important variable affecting the liquid permeation rate from the cathode to the anode.

5.5 References

1. T. V. Nguyen, Water Management by Material Design and Engineering for PEM Fuel Cells, *ECS Trans.*, 3 (1) (1), 1171, **2006**.

2. H. K. Atiyeh, K. Karan, B. Peppley, A. Phoenix, E. Halliop and J. Pharoah, Experimental Investigation of the Role of a Microporous Layer on the Water Transport and Performance of a PEM Fuel Cell, *J. Power Sources*, 170 (1), 111, **2007**.
3. N. Holmstrom, J. Itonen, A. Lundblad and G. Lindbergh, The Influence of the Gas Diffusion Layer on Water Management in Polymer Electrolyte Fuel Cells, *Fuel Cells*, 7 (4), 306, **2007**.
4. K. Karan, H. Atiyeh, A. Phoenix, E. Halliop, J. Pharoah and B. Peppley, An Experimental Investigation of Water Transport in PEMFCs - The Role of Microporous Layers, *Electrochem. Solid-State Lett.*, 10 (2), B34, **2007**.
5. G. Lin and T. V. Nguyen, Effect of Thickness and Hydrophobic Polymer Content of the Gas Diffusion Layer on Electrode Flooding Level in a PEMFC, *J. Electrochem. Soc.*, 152 (10), A1942, **2005**.
6. S. Park, J.-W. Lee and B. N. Popov, Effect of Carbon Loading in Microporous Layer on PEM Fuel Cell Performance, *J. Power Sources*, 163 (1), 357, **2006**.
7. S. Park, J.-W. Lee and B. N. Popov, Effect of PTFE Content in Microporous Layer on Water Management in PEM Fuel Cells, *J. Power Sources*, 177 (2), 457, **2008**.
8. Z. Qi and A. Kaufman, Improvement of Water Management by a Microporous

- Sublayer for PEM Fuel Cells, *J. Power Sources*, 109 (1), 38, **2002**.
9. R. P. Ramasamy, E. C. Kumbar, M. M. Mench, W. Liu, D. Moore and M. Murthy, Investigation of Macro- and Micro-Porous Layer Interaction in Polymer Electrolyte Fuel Cells, *Int. J. Hydrogen Energy*, 33 (13), 3351, **2008**.
 10. H. Tang, S. Wang, M. Pan and R. Yuan, Porosity-Graded Micro-Porous Layers for Polymer Electrolyte Membrane Fuel Cells, *J. Power Sources*, 166 (1), 41, **2007**.
 11. G. Velayutham, J. Kaushik, N. Rajalakshmi and K. S. Dhathathreyan, Effect of PTFE Content in Gas Diffusion Media and Microlayer on the Performance of PEMFC Tested under Ambient Pressure, *Fuel Cells*, 7 (4), 314, **2007**.
 12. X. Wang, H. Zhang, J. Zhang, H. Xu, X. Zhu, J. Chen and B. Yi, A Bi-Functional Micro-Porous Layer with Composite Carbon Black for PEM Fuel Cells, *J. Power Sources*, 162 (1), 474, **2006**.
 13. X. L. Wang, H. M. Zhang, J. L. Zhang, H. F. Xu, Z. Q. Tian, J. Chen, H. X. Zhong, Y. M. Liang and B. L. Yi, Micro-Porous Layer with Composite Carbon Black for PEM Fuel Cells, *Electrochim. Acta*, 51 (23), 4909, **2006**.
 14. Y. Fujii, S. Tsushima, K. Fukuzato and S. Hirai, Effect of the Micro Porous Layer on Water Transport under Low Humidity Condition, *ECS Trans.*, 16 (2) (2), 1635, **2008**.
 15. T. V. Nguyen, G. Lin, H. Ohn, X. Wang, D. S. Hussey, D. L. Jacobson and M. Arif,

- Measurements of Two-Phase Flow Properties of the Porous Media Used in PEM Fuel Cells, *ECS Trans.*, 3 (1), 415, **2006**.
16. F. E. Hizir, T. Swamy, S. O. Ural, E. C. Kumbur and M. M. Mench, Characterization of the Micro Porous Layer - Catalyst Layer Interface Structure in Polymer Electrolyte Fuel Cells, *Proceedings of ASME 2009 7th International Fuel Cell Science, Engineering and Technology Conference*, Newport Beach, California, FuelCell2009, **2009**.
 17. G. Lin, *TVN Systems, Inc.*, Private Communication, **June 2009**.
 18. J. T. Gostick, M. A. Ioannidis, M. W. Fowler and M. D. Pritzker, On the Role of the Microporous Layer in PEMFC Operation, *Electrochem. Commun.*, 11 (3), 576, **2009**.
 19. W. Dai, H. Wang, X.-Z. Yuan, J. Martin, J. Shen, M. Pan and Z. Luo, Measurement of Water Transport Rates Across the Gas Diffusion Layer in a Proton Exchange Membrane Fuel Cell, and the Influence of Polytetrafluoroethylene Content and Micro-Porous Layer, *J. Power Sources*, 188 (1), 122, **2009**.
 20. J. Chen, T. Matsuura and M. Hori, Novel Gas Diffusion Layer with Water Management Function for PEMFC, *J. Power Sources*, 131 (1-2), 155, **2004**.
 21. U. Pasaogullari and C.-Y. Wang, Two-Phase Transport and the Role of

- Micro-Porous Layer in Polymer Electrolyte Fuel Cells, *Electrochim. Acta*, 49 (25), 4359, **2004**.
22. U. Pasaogullari, C.-Y. Wang and K. S. Chen, Two-Phase Transport in Polymer Electrolyte Fuel Cells with Bilayer Cathode Gas Diffusion Media, *J. Electrochem. Soc.*, 152 (8), A1574, **2005**.
23. S. Shimpalee, U. Beuscher and J. W. Van Zee, Investigation of Gas Diffusion Media Inside PEMFC Using CFD Modeling, *J. Power Sources*, 163 (1), 480, **2006**.
24. A. Z. Weber and J. Newman, Effects of Microporous Layers in Polymer Electrolyte Fuel Cells, *J. Electrochem. Soc.*, 152 (4), A677, **2005**.
25. Z. Zhan, J. Xiao, Y. Zhang, M. Pan and R. Yuan, Gas Diffusion Through Differently Structured Gas Diffusion Layers of PEM Fuel Cells, *Int. J. Hydrogen Energy*, 32 (17), 4443, **2007**.
26. A. Z. Weber, R. M. Darling and J. Newman, Modeling Two-Phase Behavior in PEFCs, *J. Electrochem. Soc.*, 151 (10), A1715, **2004**.
27. X. Wang and T. V. Nguyen, Modeling the Effects of Capillary Property of Porous Media on the Performance of the Cathode of a PEMFC, *J. Electrochem. Soc.*, 155 (11), B1085, **2008**.
28. J. D. Fairweather, P. Cheung, J. St-Pierre and D. T. Schwartz, A Microfluidic

- Approach for Measuring Capillary Pressure in PEMFC Gas Diffusion Layers,
Electrochem. Commun., 9 (9), 2340, **2007**.
29. T. V. Nguyen, G. Lin, H. Ohn and X. Wang, Measurement of Capillary Pressure Property of Gas Diffusion Media Used in Proton Exchange Membrane Fuel Cells,
Electrochem. Solid-State Lett., 11 (8), B127, **2008**.
30. X. Wang and T. V. Nguyen, Modeling the Effects of the Cathode Micro-Porous Layer on the Performance of a PEM Fuel Cell, *ECS Trans.*, 16 (2) (2), 3, **2008**.
31. Q. Ye and T. V. Nguyen, Three-Dimensional Simulation of Liquid Water Distribution in a PEMFC with Experimentally Measured Capillary Functions, *J. Electrochem. Soc.*, 154 (12), B1242, **2007**.
32. T. E. Springer, T. A. Zawodzinski and S. Gottesfeld, Polymer Electrolyte Fuel-Cell Model, *J. Electrochem. Soc.*, 138 (8), 2334, **1991**.
33. D. M. Bernardi and M. W. Verbrugge, Mathematical Model of a Gas-Diffusion Electrode Bonded to a Polymer Electrolyte, *AIChE J.*, 37 (8), 1151, **1991**.
34. D. M. Bernardi and M. W. Verbrugge, A Mathematical Model of the Solid-Polymer-Electrolyte Fuel Cell, *J. Electrochem. Soc.*, 139 (9), 2477, **1992**.

Chapter 6

A Modeling Study of the Effects of Anode Porous Layer on the Performance of a PEM Fuel Cell

6.1 Introduction

Chapter 4 and Chapter 5 investigated the effects of the porous media on the liquid water saturation levels and fuel cell performance of a PEM fuel cell. When the MPL exists in the cathode side, the permeation and back diffusion of the liquid water from the cathode to the anode could be greater than the electro-osmosis from the anode to the cathode, leading the less flooded cathode and possibly flooded anode. However, the models in Chapter 4 and Chapter 5 are cathode models only, in which the anode is simplified to an interface. This treatment is valid when the anode is not the limiting step. When too much liquid water is forced to the anode, a flooded anode may lead to poor fuel cell performance. This chapter addressed the complete region of a PEM fuel cell, in which the anode was included in the model. This model will be used to study the effects of the anode side on the liquid water transport within an MEA and subsequently the fuel cell performance.

6.2 Model Development

6.2.1 Modeled Domain

The modeled domain is shown in Fig. 6.1. The cathode side consists of a macro-porous GDL, an MPL, and a CL. The anode side shown in Fig. 6.1 consists of a macro-porous GDL and a CL only. For the case with an MPL in the anode side, the schematic view is similar to that of the cathode side. In this model, the x direction is defined from the cathode to the anode.

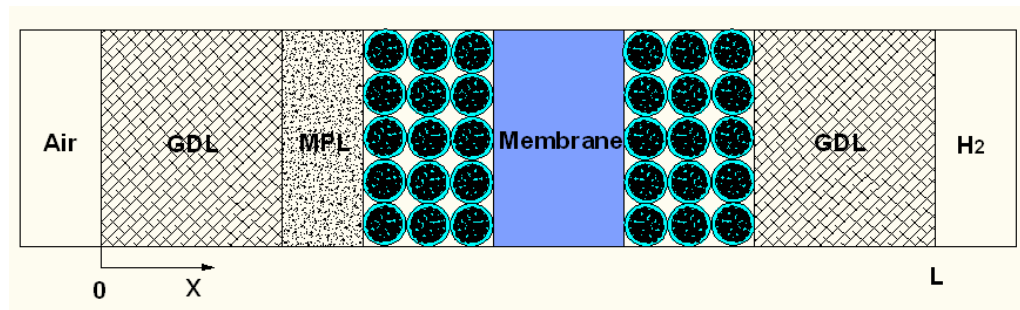


Figure 6.1 Schematic diagram of the modeled domain.

6.2.2 Governing Equations

The governing equations of the anode side are summarized in Table 6.1. For details on the cathode equations, one is referred to Chapter 4 and Chapter 5 as well as references 1 and 2.

Table 6.1 Governing equations of the anode.

| Variables | CL | GDL |
|-------------|----------------------------------------|----------------------------------|
| $C_{H_2}^g$ | $-\frac{dN_{H_2}^g}{dx} - R_{H_2} = 0$ | $-\frac{dN_{H_2}^g}{dx} = 0$ |
| C_v^g | $-\frac{dN_v^g}{dx} - R_w^c = 0$ | $-\frac{dN_v^g}{dx} - R_w^c = 0$ |
| ϕ_+ | $-\frac{di_+}{dx} + 2FR_{H_2} = 0$ | N/A |
| s_{GDL} | N/A | $-\frac{dN_w}{dx} + R_w^c = 0$ |
| s_{CL} | $-\frac{dN_w}{dx} + R_w^c = 0$ | N/A |
| C_w^N | $-\frac{dN_w^N}{dx} = 0$ | N/A |
| p_l | $p_l = p_g - p_c$ | $p_l = p_g - p_c$ |

An agglomerate model of the CLs of both the cathode and anode sides is used. In the catalyst layer at the anode side, the hydrogen oxidation reaction (HOR) is expressed by

$$R_{H_2} = \frac{\frac{RT}{H_{H_2}^N}}{\frac{\delta_N}{a_r D_{H_2}^N} + \frac{\delta_w}{a_r D_{H_2}^w} \frac{H_{H_2}^w}{H_{H_2}^N} + \frac{1}{\xi k_T}} C_{H_2}^g \quad [6.1]$$

The parameters in Eq. 6.1 are similarly defined as those in Chapter 4 as well as in Ref. 1. The reaction rate constant is expressed by

$$k_T = \frac{a_{Pt}^{agg} i_0 (1 - \varepsilon_{CL})}{RT C_{H_2}^{ref}} (-\phi_+) \quad [6.2]$$

where a_{Pt}^{agg} is the active catalyst surface area per unit volume of agglomerates; ε_{CL} is the CL porosity; i_0 is the hydrogen reference exchange current density; $C_{H_2}^{ref}$ is the hydrogen reference concentration; ϕ_+ is the ionic potential. Since the ionic overpotential is very low in the anode side as a result of the extremely fast hydrogen oxidation reaction, a linear approximation of Butler-Volmer equation is used in Eq. 6.2.

For spherical agglomerate pellets, the effectiveness factor is defined by ³

$$\xi = \frac{\coth(3\varphi)}{\varphi} - \frac{1}{3\varphi^2} \quad [6.3]$$

where the modulus is expressed by

$$\varphi = \frac{r}{3} \sqrt{\frac{k_T / (1 - \varepsilon_{CL})}{D_{H_2}^{N,eff}}} \quad [6.4]$$

6.2.3 Boundary Conditions

The boundary conditions of the anode side used in this model are summarized in Table 6.2. The boundary conditions of the cathode side are the same as those in Chapter 4 and Chapter 5. At the membrane and anode CL interface (MEM/CL), the fluxes of hydrogen and water vapor are set to zero. Continuity of current density connects the anode side to the cathode side. Permeation and diffusion of water from the membrane are set equal to the liquid flux in the anode CL.

$$N_w^{p,c} \Big|_{MEM} = N_w \Big|_{CL} \quad [6.5]$$

where the $N_w^{p,c}|_{MEM}$ and $N_w|_{CL}$ are expressed by

$$N_w^{p,c}|_{MEM} = -D_w^N \nabla C_w^N - \frac{\rho_w}{M_w} \frac{K_l^{MEM}}{\mu_w} \nabla p_l \quad [6.6]$$

$$N_w|_{CL} = \frac{\rho_w}{M_w} \frac{K_{w,0}^{CL}}{\mu_w} \frac{\partial p_c}{\partial s} s^{4.5} \frac{\partial s}{\partial x} \quad [6.7]$$

At the anode CL/GDL interface, flux continuities of hydrogen, water vapor, and liquid water are used. Capillary force balance at this interface leads to the discontinuity of liquid water saturation level when two porous media with different wetting properties are placed in contact.

Conditions at the inlet are used as boundary conditions at the anode GDL/channel ($x=L$) interface. Liquid pressure is set equal to gas pressure when the anode gas stream is saturated with water vapor, and the liquid water saturation level corresponding to this $p_c = 0$ point is used. As shown in the following parts of this chapter, when a cathode with a hydrophobic MPL is used, the anode gas is saturated because the liquid water driven from the cathode to the anode is greater than the amount transported by electro-osmosis.

Table 6.2 Boundary conditions.

| Variables | MEM/CL | CL/GDL | x=L |
|-------------|---------------------------------------|--------------------------------------|-----------------------------------|
| $C_{H_2}^g$ | $N_{H_2}^g _{CL} = 0$ | $N_{H_2}^g _{CL} = N_{H_2}^g _{GDL}$ | $C_{H_2}^g = C_{H_2}^{g,initial}$ |
| C_v^g | $N_v^g _{CL} = 0$ | $N_v^g _{CL} = N_v^g _{GDL}$ | $C_v^g = C_v^{g,initial}$ |
| ϕ_+ | $i_+ _{MEM} = i_+ _{CL}$ | $i_+ = 0$ | N/A |
| s_{GDL} | N/A | $N_w _{CL} = N_w _{GDL}$ | $p_{c,GDL} = 0$ |
| s_{CL} | $N_w _{MEM}^{p,c} = N_w _{CL}$ | $p_c _{CL} = p_c _{GDL}$ | N/A |
| C_w^N | $C_w^N = C_{w,(\alpha)}^{N,eq,anode}$ | $N_w^N _{\alpha} = 0$ | N/A |
| p_l | $p_l = p_g - p_c$ | $p_l = p_g - p_c$ | $p_l = p_g = 1atm$ |

6.2.4 Capillary Curves

As what have been done in Chapter 4 and Chapter 5, capillary curves for the carbon GDLs and MPLs are fitted in the form of ⁴

$$p_c = d \left[e^{-a_1(s-c)} - e^{a_2(s-c)} \right] + b \quad [6.7]$$

The fitted parameters of the capillary curves are summarized in Table 6.3. These curves are shown in Fig. 6.2. In this model, the capillary curves in the cathode side are fixed as G1, M2, and C1 for the cathode GDL, MPL, and CL, respectively. It is assumed that the anode GDL, MPL, and CL have the same capillary properties as those used in the cathode side. G1, M2, and C1 are the same as those shown in

Chapter 5. M2 is selected here since it led to the positive liquid water flux (from the cathode side to the anode side) as shown in Chapter 5.

Table 6.3 Capillary functions.

| | | | |
|---------------------------|------------------------------|-------------|-------------------|
| Curve G1, a1, a2, b, c, d | -22.69, -16.19, -644.86 Pa, | 0.578, | -7.59 Pa |
| Curve C1, a1, a2, b, c, d | -45.00, -8.00, | 5000.00 Pa, | 0.78, -1106.56 Pa |
| Curve M2, a1, a2, b, c, d | -30.00, -16.00, -9878.42 Pa, | 0.10, | -4000.00 Pa |

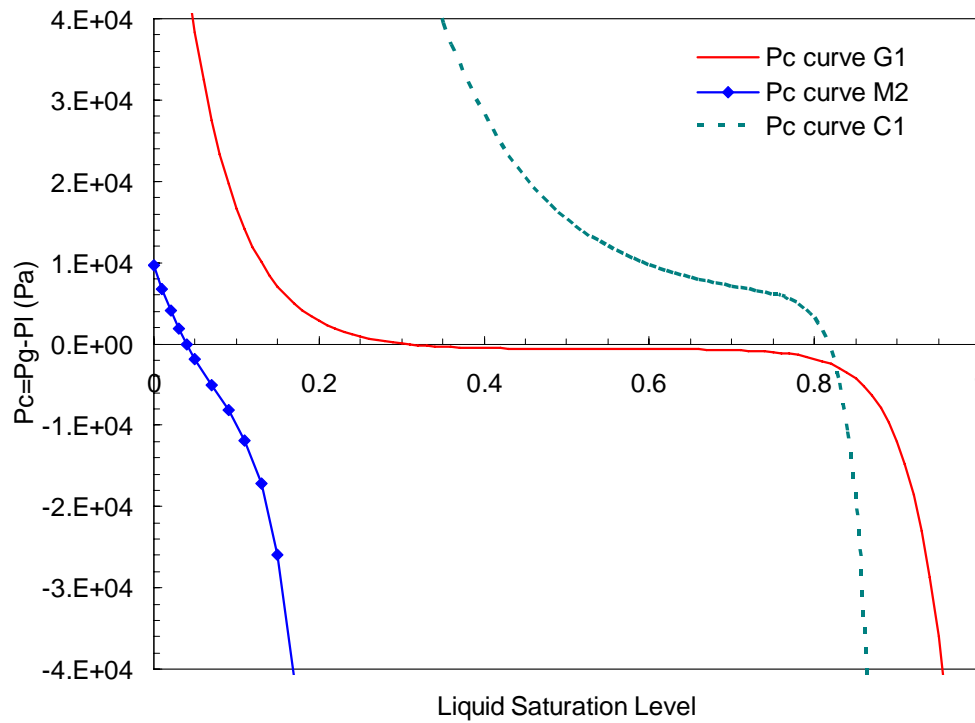


Figure 6.2 Capillary curves used in the model.

6.2.5 Parameters Used in the Simulation

Table 6.4 lists the parameters used in the simulation. Table 6.5 summarizes the operational conditions. Other parameters can be found in Chapter 4, Chapter 5, and reference 1.

Table 6.4 Parameters.

| | |
|-----------------------------------------------------|--------------------------------------------------|
| cGDL and aGDL properties | |
| Porosity, ε_{GDL} | 0.5 |
| Thickness, δ_{GDL} | 230 μm for cathode 250 for μm anode |
| Absolute liquid water permeability, $K_{w,0}^{GDL}$ | $1.0 \times 10^{-10} \text{ cm}^2$ |
| cMPL and aMPL properties | |
| Porosity, ε_{MPL} | 0.3 |
| Thickness, δ_{MPL} | 20 μm |
| Absolute liquid water permeability, $K_{w,0}^{MPL}$ | $1.0 \times 10^{-12} \text{ cm}^2$ |
| cCL and aCL properties | |
| Porosity, ε_{CL} | 0.12 |
| Thickness, δ_{CL} | 16 μm |
| Absolute liquid water permeability, $K_{w,0}^{CL}$ | $5.0 \times 10^{-13} \text{ cm}^2$ |
| Catalyst loading, m_{Pt} | 0.4 mg Pt/cm ² |
| Specific surface area of Pt, a_{Pt} | 1000 cm ² /mg Pt |

| | |
|-----------------------------------------------------------------|-------------------------|
| Volume fraction of Nafion in catalyst pellet, ε_N^p | 0.393 |
| Radius of the spherical catalyst pellet, r | 1.0×10^{-5} cm |
| Thickness of Nafion film, δ_N | 1.0×10^{-6} cm |

Membrane properties

| | |
|--------------------------------------------------------|-------------------------------------------|
| Thickness, δ_{MEM} | 50 μm |
| Fixed charge site concentration, C_f | 1.2×10^{-3} mole/cm ³ |
| Membrane liquid permeability, ⁵ K_l^{MEM} | 1.8×10^{-14} cm ² |

cGDL, cMPL, and cCL represent cathode GDL, MPL and CL, respectively.

aGDL, aMPL, and aCL represent anode GDL, MPL and CL, respectively.

Table 6.5 Operation conditions.

| | |
|-------------------------------------------------------|--------------------------------------------|
| Temperature, T | 60 °C |
| Pressure, P | 1 atm |
| Humidity of the air inlet | 100% |
| Humidity at anode | 100% |
| Anode stoich | 2.0 |
| Evaporation rate constant, k_v | 100 $\frac{1}{atm \cdot s}$ |
| Condensation rate constant, k_c | 100 $\frac{1}{s}$ |
| Reference hydrogen concentration, $C_{H_2}^{ref}$ | 2.23×10^{-5} mole/cm ³ |
| Hydrogen exchange current density, ⁶ i_0 | 1.4×10^{-3} A/cm ² |

6.3 Results and Discussion

Fig. 6.3 shows the amount of water needed to saturate a dry anode with different

hydrogen stoichiometry. As expected, the water needed increases with the current density and hydrogen stoichiometric flow rate. Anode feed gas humidification could be eliminated when the liquid water back transport rate from the cathode to the anode is equal or greater than the electro-osmotic rate.

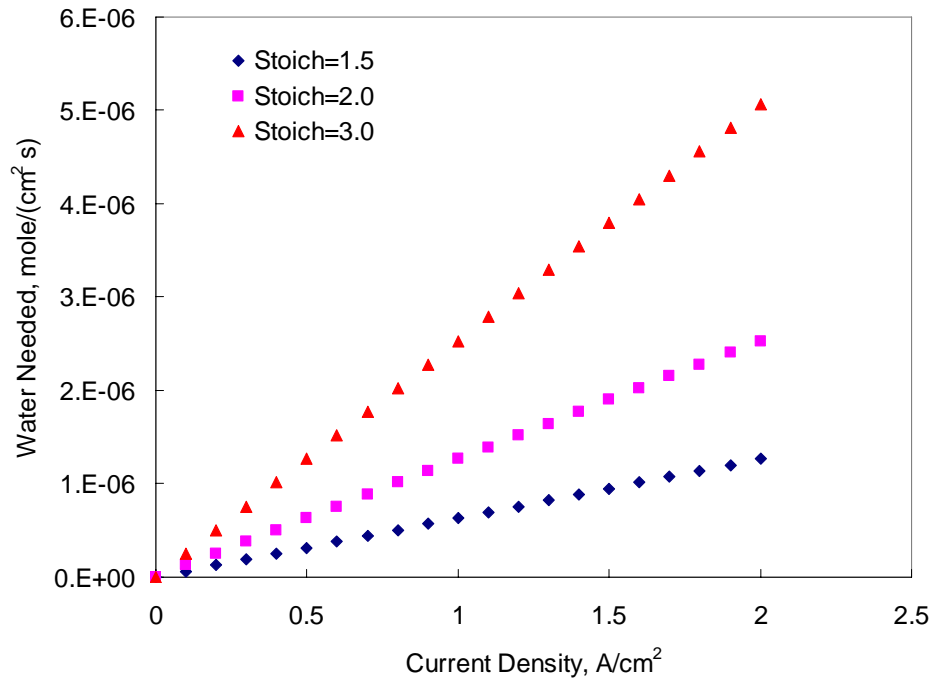


Figure 6.3 Water needed to saturate a dry anode at 60 °C.

Distributions of liquid water saturation level and liquid pressure in the modeled domain are plotted in Fig. 6.4. When an MPL exists on the anode side, the saturation levels in the anode GDL are lower than those without an MPL in the anode side because the hydrophobic MPL blocks the liquid water from getting into the anode

GDL. The anode MPL has an opposite effect on the saturation levels in the cathode side since more liquid water accumulates in the cathode when an anode MPL exists. The liquid pressure changes correspondingly to the saturation levels as shown in Fig. 6.4 (b). In the case with anode MPL, although the liquid pressures in the anode and cathode are higher, the pressure gradient is lower compared to the case without anode MPL.

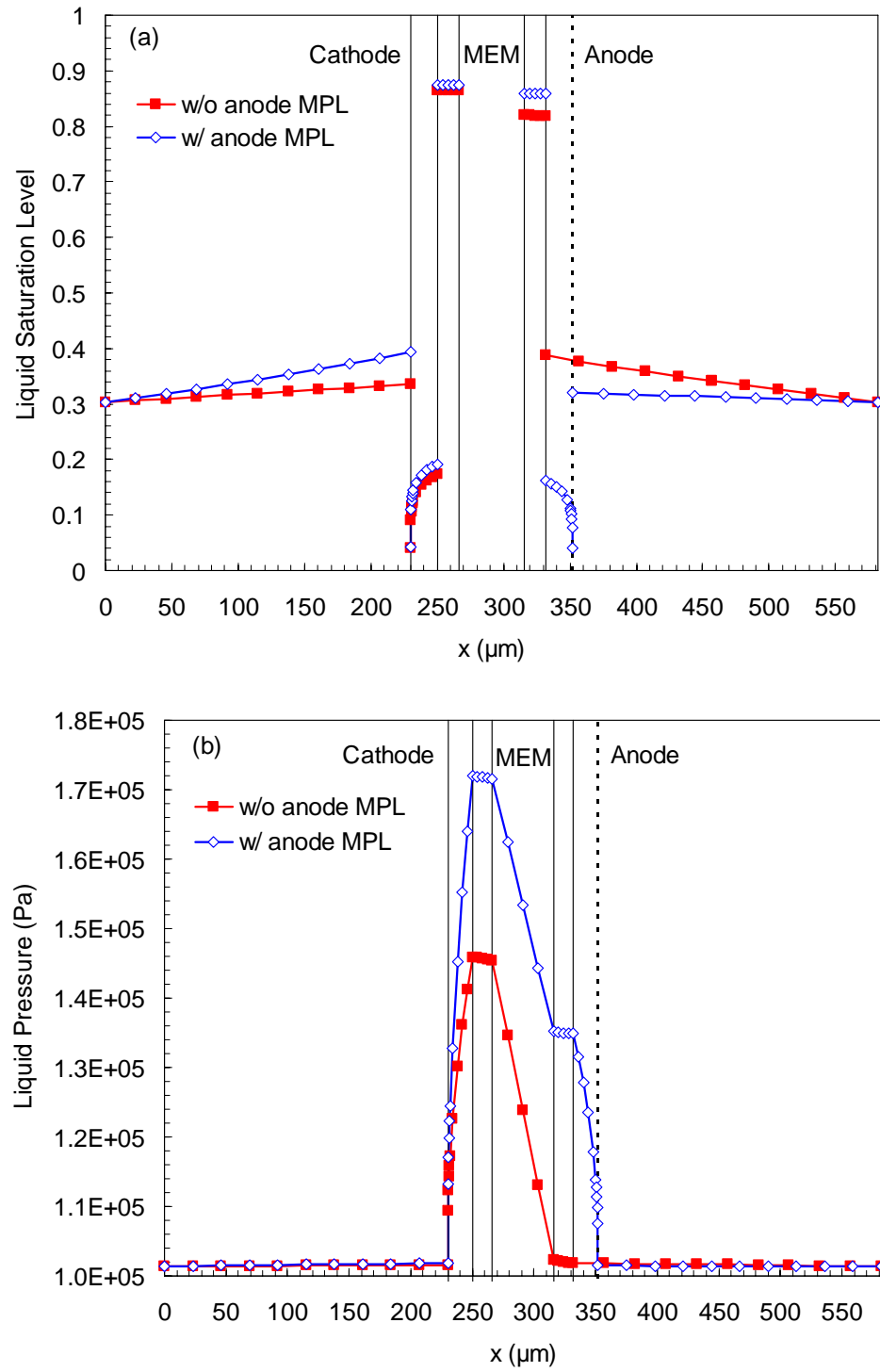


Figure 6.4 Distribution of (a) saturation levels, and (b) liquid water pressure in the modeled domain at 0.6 V.

Liquid water flux is shown in Figure 6.5. It is seen that liquid water flux in the anode side is lower in the case with an anode MPL while an opposite trend in the cathode side is seen. Since a saturated hydrogen fuel is used in this model, evaporation is assumed to be eliminated either at the anode GDL/channel interface or in the anode gas channels. Thus, the liquid water flux in the modeled domain shows the effects of the anode MPL on the water flux direction. It is seen that the anode MPL prevents the liquid water from being transported out to the anode side.

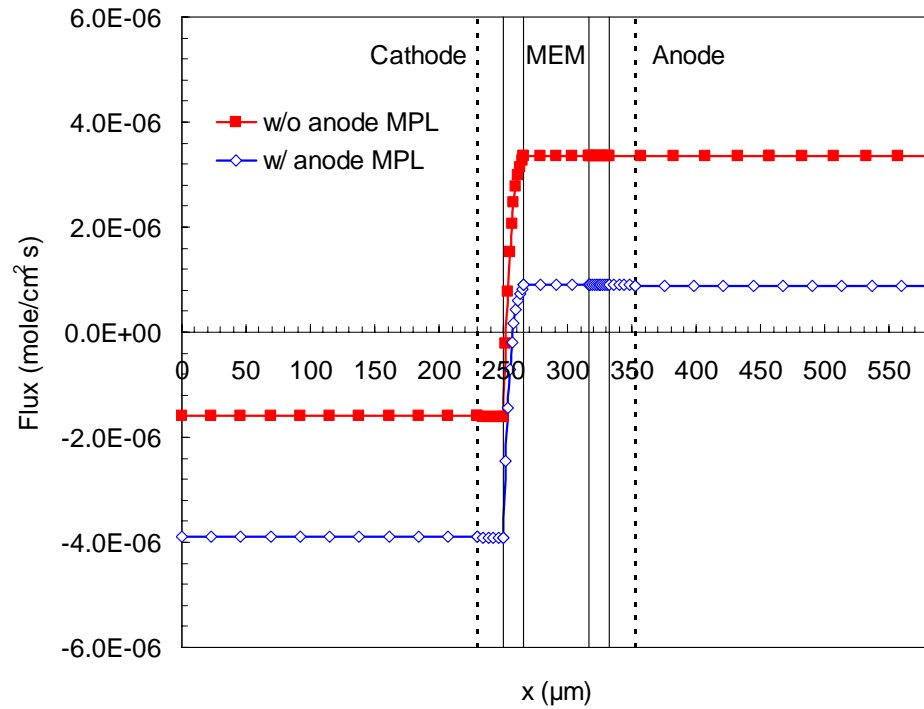


Figure 6.5 Liquid water flux in the modeled domain at 0.6 V.

Fig. 6.6 shows that having an MPL in the anode side leads to slightly lower fuel cell performance. This is attributed to higher liquid saturation levels in the cathode GDL and CL and anode CL, which impedes the transport of reactant gases (mainly oxygen) to the reactive surfaces. The case without an MPL in the anode allows more liquid water transports back from the cathode to the anode, which indicates zero-net water flux, or even positive net water flux, across the membrane is possible when the properties of porous media of both the anode and cathode are well designed. The anode might be able to tolerate higher levels of flooding since hydrogen transport and reaction are more facile than oxygen. With the current parameters in this model, the fuel cell performances of the two cases studied show comparable fuel cell performance.

It is seen from Fig. 6.3 that at current density $1\text{A}/\text{cm}^2$ and stoichiometry of 2, the theoretical amount of liquid water needed to saturate dry hydrogen in anode side is about $1.3\text{E-}6\text{ mole}/(\text{cm}^2\cdot\text{s})$. It is seen that liquid water flux from the cathode to the anode in the case without an MPL in the anode side is more than sufficient to saturate the dry fuel in the anode side (in Fig. 6.5, 0.6V is corresponding to about $1\text{A}/\text{cm}^2$). This shows that the pressure driven permeation of liquid water from the cathode to the anode is greater than the electro-osmosis from the anode to the cathode. Thus, the MPL is preferred in the cathode side while the opposite electrode structure is

preferred in the anode side (without the MPL in the anode side).

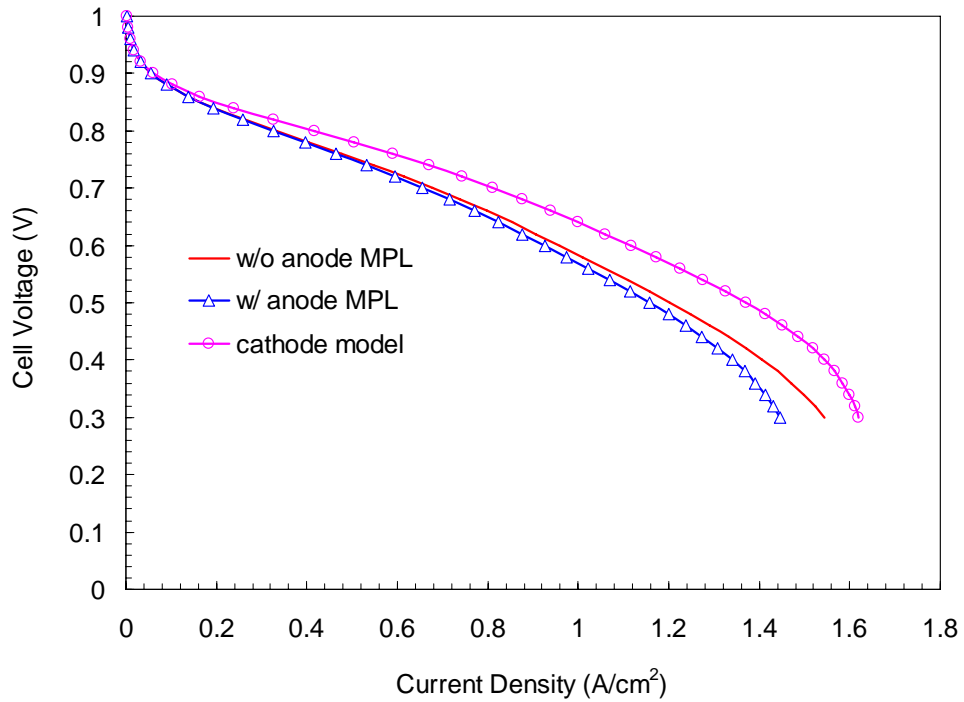


Figure 6.6 Effects of anode MPL on fuel cell performance.

The results of the cathode model in Chapter 5 (G1-M2-C1) are also presented in Fig. 6.6 to show that cathode model over predicts the fuel cell performance. The over-prediction of the fuel cell voltage of the cathode model results, mainly from the omission of the ohmic losses in the anode. Comparison of the ionic potential is shown in Fig. 6.7. The comparison verifies that the ionic potentials in the complete model are bigger (more negative) than that of the cathode model.

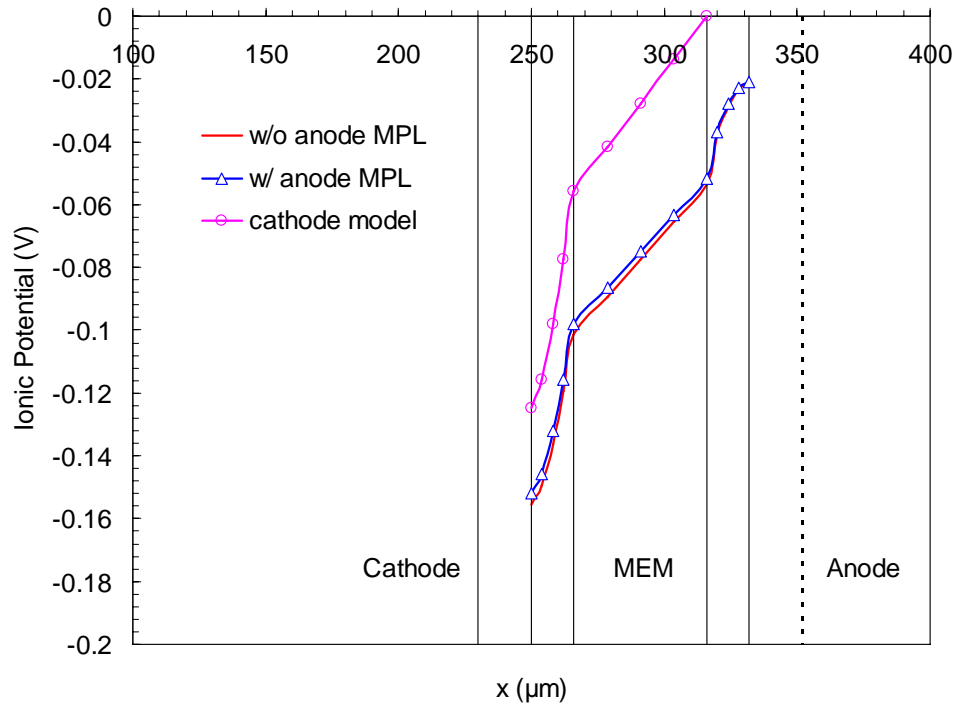


Figure 6.7 Ionic potential in the modeled domain.

6.4 Conclusions

The results show that a hydrophobic MPL in the anode side reduces the transport rate of liquid water into the anode gas channels. While its presence reduces the liquid water saturation levels in anode GDL, it increases the saturation levels in anode CL and cathode CL and GDL. The simulation shows that the amount of liquid water transported back from the cathode side to the anode side in the case without anode MPL is more than sufficient to saturate the anode fuel, which indicates a possible elimination of anode humidification. The fuel cell performances of the two cases investigated in this study are comparable with the current parameters used in this

model, showing that an MPL in the anode is not preferred. Zero-net liquid water flux across the membrane is achievable when the properties of the porous media used in a PEM fuel are properly designed. The complete model also showed that when the anode was treated as an interface instead of a complete porous electrode, over-prediction of the fuel cell voltage resulted, mainly from the omission of the ohmic losses in the anode. Experimental validation of this model study needs to be carried out.

6.5 References

1. X. Wang and T. V. Nguyen, Modeling the Effects of Capillary Property of Porous Media on the Performance of the Cathode of a PEMFC, *Journal of The Electrochemical Society*, 155 (11), B1085, **2008**.
2. X. Wang and T. V. Nguyen, Modeling the Effects of the Cathode Micro-Porous Layer on the Performance of a PEM Fuel Cell, *ECS Transactions*, 16 (2) (2), 3, **2008**.
3. G. F. Froment and K. B. Bischoff, *Chemical Reactor Analysis and Design*, 2nd ed.; Wiley: New York, p xxxiv, 1990.
4. Q. Ye and T. V. Nguyen, Three-Dimensional Simulation of Liquid Water Distribution in a PEMFC with Experimentally Measured Capillary Functions,

- Journal of the Electrochemical Society*, 154 (12), B1242, **2007**.
5. D. M. Bernardi and M. W. Verbrugge, A Mathematical Model of the Solid-Polymer-Electrolyte Fuel Cell, *Journal of the Electrochemical Society*, 139 (9), 2477, **1992**.
 6. A. Z. Weber and J. Newman, Effects of Microporous Layers in Polymer Electrolyte Fuel Cells, *Journal of the Electrochemical Society*, 152 (4), A677, **2005**.

Chapter 7

Conclusions and Recommendations

7.1 Conclusions

This study focused on the effects of the properties of porous media and water management strategies in PEM fuel cells. Chapter 2 presented the experimental measurement of the relative permeability of the porous media used in PEM fuel cells. In Chapter 3, the liquid water saturation levels in the cathode side of a PEM fuel cell were determined using the experimentally determined relative permeability from Chapter 2. The experimentally determined properties of the porous media can be used in numerical simulations to accurately predict fuel cell performance. Chapters 4, 5 and 6 presented the simulated results of the PEM fuel cells. Those simulated results can be used to direct further experimental work and develop new materials with preferred two-phase flow properties in order to achieve optimal fuel cell performance.

7.1.1 Experimental

The liquid and gas permeability of the porous media used in PEM fuel cells was experimentally measured using both gravimetric analysis and neutron imaging. At low liquid water saturation levels, the measurements from these two methods closely coincided. However, discrepancies between these two methods arose at high liquid saturation levels. The discrepancy was attributed to the procedure used to determine

the saturation levels in the porous media. In the gravimetric analysis method, the liquid water may be imbibed back into the sample once the pressure applied on the sample is released. Liquid relative permeability was difficult to obtain at both high and low saturation levels. The gas and liquid relative permeability showed that the 3rd-order power correlations were inappropriate for the porous media used in PEM fuel cells because porous media exhibit different properties than well sorted hydrophilic sands.

Using the experimentally determined correlations of relative permeability and liquid saturation levels developed in Chapter 2, the liquid water saturation levels were determined in fuel cells under serpentine and interdigitated operating conditions. These results are described in Chapter 3. This technique used the pressure drop of the interdigitated flow field to indicate the flooding content in a fuel cell.¹ The fuel cell was first operated under serpentine flow mode followed by a switch to interdigitated flow mode. Better fuel cell performances were obtained under interdigitated mode because the gaseous reactant transport was more effective and the liquid water saturation levels were lower. Both higher stoichiometry and increased temperature were beneficial to the fuel cell. The former led to lower saturation levels in the cathode due to higher flow velocity, while the latter increased the evaporation rate to remove the liquid water in the fuel cell.

7.1.2 Modeling

A two-phase flow model was presented in Chapter 4 using the experimentally determined capillary pressure of the GDL. The saturation level jump condition at two porous media with different wettability was included. The force balance between the porous media causes the saturation level jump condition. This discontinuity is very common in chemical and physical systems. For example, the difference of gas solubility in the gas phase versus the liquid/solid phase is well known and justified. The saturation levels in the GDL and CL were correctly addressed by using the capillary force balance. In the past, the Leverett function developed for the hydrophilic sands was commonly used due to the lack of data in literature about capillary pressure curves of GDLs.²⁻⁶ The GDLs used in the PEM fuel cells are made of graphite fibers which have totally different morphological and wetting properties than the sands. Therefore, the Leverett function has been inappropriately applied to PEM fuel cells. The model developed in Chapter 4 avoided this by using an experimentally measured capillary curve of the GDL.⁷ The shape, position, and magnitude of the capillary curves of the GDL and CL were investigated to elucidate the effect of the properties of the porous media on the PEM fuel cell performance. It showed that the GDL was important in achieving optimal fuel cell performance when the gaseous react transport was the limiting step.

In the model developed in Chapter 4 to simulate the cathode GDL, CL, and the membrane, the pressure driven permeation was neglected because the liquid pressure gradient across the membrane was low. Chapter 5 numerically solved a problem consisting of the cathode GDL, MPL, CL, and the membrane. The pressure gradient across the membrane was much higher than without the MPL. Thus, the pressure driven permeation part was considered in Chapter 5 in order to address the liquid water transport in the porous media correctly. Chapter 5 aimed at numerical optimization of the fuel cell to achieve the condition of zero-net-water-transport-across-the-membrane. This study helps to explain the mechanism by which the performance of a PEM fuel cell is improved by adding an MPL between the GDL and the CL in the cathode side. The hydrophobic MPL prevents the liquid water from transporting out of the cathode CL, leading to increased saturation levels in the CL and decreased saturation levels in the GDL. Increased saturation in the CL leads to an increased liquid pressure gradient across the membrane, resulting in a corresponding increase in the permeation from the cathode to the anode. The net effect of adding an MPL is improved gas transport in the cathode and a lower humidification requirement in the anode. When the properties of the porous media are appropriately arranged, the goal of zero-net-water-transport-across-the-membrane is achievable, eliminating the anode

humidification requirement and improving the fuel cell performance. This model will assist in the engineering and manufacturing of porous media used in PEM fuel cells.

Chapter 6 presented a model in which the cathode and anode were included. The anode side was neglected in Chapter 4 and Chapter 5 by assuming that the anode overpotential was insignificant. Chapter 6 showed that the fuel cell performance was seldom affected by the MPL in the anode side, indicating that the MPL in the anode side could be eliminated to simplify the anode electrode. Under this circumstance, the anode CL and GDL must be hydrophobic to prevent the anode from being flooded because liquid water was forced from the cathode side to the anode side by the cathode MPL.

7.2 Recommendations

The experimental work and the numerical modeling in this study will help researchers in this area to better understand PEM fuel cells and design more effective studies in the future. The following section presents specific recommendations for subsequent models and experiments.

7.2.1 Experimental

In Chapter 2, the relative permeability experiment was carried out at a constant thickness by controlling the thickness of the shims in the fixture. The fuel cell tests in Chapter 3 were carried out at constant pressure by controlling the compression force

when assembling the fuel cells. The difference in compression controls led to a large change of the GDLs' permeability because it was greatly affected by the compression. This problem can be solved either by controlling the thickness of the electrodes in Chapter 3 (fuel cell performance measurement) or by controlling the compression force in Chapter 2 (relative permeability measurement).

In recent years, the capillary curves of the GDLs used in PEM fuel cells have become available.⁷⁻¹⁴ However, the available data in literature were obtained at ambient temperature instead of at the temperature of a typical operating fuel cell. Temperature affects the capillary curve greatly because the surface tension changes with temperature. Therefore, future experimental work on the capillary curve should be carried out at the fuel cell operating temperatures.

Due to the thinness of the MPL (about 20 μm) and CL (about 15 μm), the two-phase transport properties of these layers are not available in the literature. This study assumed a more hydrophilic CL and a more hydrophobic MPL than the GDL in the simulations. Experimental investigation of the relative permeability and capillary curve of these layers is greatly needed.

The models showed that GDL properties were important in water management strategies to achieve the optimal fuel cell performance. Thus, surface modification of GDLs by material engineering should be fully investigated to improve the fuel cell

performances. The hydrophobicity of the CLs in both the cathode and anode is an important factor in achieving the desired fuel cell performance. This study showed that hydrophobic CLs in the cathode and anode were required to prevent the fuel cell electrodes from being flooded. Hydrophobic CLs were obtained by adding hydrophobic solid phase, PTFE, to the corresponding CLs. As discussed in Chapter 1, CLs are three-phase transport regions in which the gas phase, liquid phase, and solid phase are involved. Although preliminary work has been carried out in Nguyen's group, novel methods of modifying the CLs to meet the three-phase transport requirement and the hydrophobic properties need to be further developed.

7.2.2 Modeling

The models developed in this study are one-dimensional, steady state, and isothermal only. Two- and three-dimensional models are needed to address the reactants and product distributions along the channels, as well as across the channels and shoulders. The temperature distribution also affects the water management strategies, which was not considered in this study.

In practice, particularly when applied in automobiles, fuel cells are subject to frequent start-ups and shut-downs. To address the unstable phenomena involved in these transient processes, transient models need to be developed to investigate the phenomena in the start-up and shut-down stages. Such models need to be developed

and validated by experimental work. Furthermore, the models involved in this study consisted of only a single fuel cell. Future models of the fuel cell stack will be helpful in better understanding the application of PEM fuel cells in automobiles.

7.3 Contributions to This Area

7.3.1 Direct Contributions

This research contributed to the PEM fuel cell area through the following publications.

1. Xuhai Wang, Trung Van Nguyen, Daniel S. Hussey, David L. Jacobson, and Muhammad Arif, “Experimental Study of Relative Permeability of Porous Media Used in PEM Fuel Cells,” *J. Electrochem. Soc.*, **“in preparation”**.
2. Xuhai Wang and Trung Van Nguyen, “Experimental Evaluation of Saturation Levels in the Cathode side and Cell Performance of a PEM Fuel Cell,” *J. Electrochem. Soc.*, **“in preparation”**.
3. Xuhai Wang and Trung Van Nguyen, “Modeling the Effects of the Micro-Porous Layer on the Net Water Transport Rate Across the Membrane in a PEM Fuel Cell,” *J. Electrochem. Soc.*, **157** (3), 1-XXXX (2010).
4. Xuhai Wang and Trung Van Nguyen, “A Modeling Study of the Anode Porous Layer on the Performance of a PEM Fuel Cell,” *ECS Trans.*, **25** (1), 29 (2009).

5. Xuhai Wang and Trung Van Nguyen, "Modeling the Effects of the Cathode Micro-Porous Layer on the Performance of a PEM Fuel Cell," *ECS Trans.*, **16** (2), 3 (2008).
6. Xuhai Wang and Trung Van Nguyen, "Modeling the Effects of Capillary Property of Porous Media on the Performance of the Cathode of a PEM Fuel Cell," *J. Electrochem. Soc.*, **155** (11), B1085 (2008).
7. Xuhai Wang and Trung Van Nguyen, "A Theoretical Study of the Effects of Two-Phase Transport Properties of the Catalyst and Gas Diffusion Layers in the Cathode on the Performance of a PEMFC," *ECS Trans.*, **11** (1), 693, (2007).

7.3.2 Indirect Contributions

The contributions that are indirectly related to this project are listed as follows.

1. Yan Gao, Xuhai Wang, and Trung Van Nguyen, "Root-Cause of Hysteresis in Capillary Pressure Curves of Porous Media Used in PEM Fuel Cells," *ECS Trans.*, **25** (1), 1765 (2009).
2. Trung Van Nguyen, Guangyu Lin, Heebong Ohn, and Xuhai Wang, "Measurement of Capillary Pressure Property of Gas Diffusion Media Used in PEM Fuel Cells," *Electrochem. Solid-State Lett.*, **11** (8), B127 (2008).
3. T.V. Nguyen, G. Lin, H. Ohn, X. Wang, D.S. Hussey, D.L. Jacobson, and M.

Arif, "Measurements of Two-Phase Flow Properties of the Porous Media Used in PEM Fuel Cells," *ECS Trans.*, **3** (1), 415-423 (2006).

7.4 References

1. W. He, G. Lin and T. V. Nguyen, Diagnostic Tool to Detect Electrode Flooding in Proton-Exchange-Membrane Fuel Cells, *AIChE J.*, 49 (12), 3221, **2003**.
2. T. Berning and N. Djilali, A 3D, Multiphase, Multicomponent Model of the Cathode and Anode of a PEM Fuel Cell, *J Electrochem Soc*, 150 (12), A1589, **2003**.
3. H. Meng and C.-Y. Wang, Model of Two-Phase Flow and Flooding Dynamics in Polymer Electrolyte Fuel Cells, *J Electrochem Soc*, 152 (9), A1733, **2005**.
4. U. Pasaogullari and C.-Y. Wang, Two-Phase Modeling and Flooding Prediction of Polymer Electrolyte Fuel Cells, *J Electrochem Soc*, 152 (2), A380, **2005**.
5. U. Pasaogullari and C. Y. Wang, Liquid Water Transport in Gas Diffusion Layer of Polymer Electrolyte Fuel Cells, *J Electrochem Soc*, 151 (3), A399, **2004**.
6. Y. Wang, Porous-Media Flow Fields for Polymer Electrolyte Fuel Cells II. Analysis of Channel Two-Phase Flow, *J Electrochem Soc*, 156 (10), B1134, **2009**.
7. J. D. Fairweather, P. Cheung, J. St-Pierre and D. T. Schwartz, A Microfluidic Approach for Measuring Capillary Pressure in PEMFC Gas Diffusion Layers,

- Electrochem Commun*, 9 (9), 2340, **2007**.
8. J. T. Gostick, M. W. Fowler, M. A. Ioannidis, M. D. Pritzker, Y. M. Volfkovich and A. Sakars, Capillary Pressure and Hydrophilic Porosity in Gas Diffusion Layers for Polymer Electrolyte Fuel Cells, *J Power Sources*, 156 (2), 375, **2006**.
 9. J. T. Gostick, M. A. Ioannidis, M. W. Fowler and M. D. Pritzker, Direct measurement of the capillary pressure characteristics of water-air-gas diffusion layer systems for PEM fuel cells, *Electrochem Commun*, 10 (10), 1520, **2008**.
 10. I. R. Harkness, N. Hussain, L. Smith and J. D. B. Sharman, The Use of a Novel Water Porosimeter to Predict the Water Handling Behaviour of Gas Diffusion Media Used in Polymer Electrolyte Fuel Cells, *J Power Sources*, 193 (1), 122, **2009**.
 11. E. C. Kumbur, K. V. Sharp and M. M. Mench, Validated Leverett Approach for Multiphase Flow in PEFC Diffusion Media I. Hydrophobicity Effect, *J Electrochem Soc*, 154 (12), B1295, **2007**.
 12. E. C. Kumbur, K. V. Sharp and M. M. Mench, Validated Leverett Approach for Multiphase Flow in PEFC Diffusion Media II. Compression Effect, *J Electrochem Soc*, 154 (12), B1305, **2007**.
 13. E. C. Kumbur, K. V. Sharp and M. M. Mench, Validated Leverett Approach for Multiphase Flow in PEFC Diffusion Media - III. Temperature Effect and Unified

Approach, *J Electrochem Soc*, 154 (12), B1315, **2007**.

14. T. V. Nguyen, G. Lin, H. Ohn and X. Wang, Measurement of Capillary Pressure Property of Gas Diffusion Media Used in Proton Exchange Membrane Fuel Cells, *Electrochemical and Solid-State Letters*, 11 (8), B127, **2008**.

Appendix

Experimental Data

Table A.1 Experimental data for Fig. 2.4

| Gravimetric Analysis | | Neutron Imaging | | 3-order Exponential | |
|----------------------|-------------------|-----------------|-------------------|---------------------|-------------------|
| S | K, m ² | S | K, m ² | S | K, m ² |
| 0 | 2.105E-11 | 0.339 | 1.013E-12 | 0 | 2.105E-11 |
| 0.096 | 1.312E-11 | 0.318 | 1.085E-12 | 0.04 | 1.862E-11 |
| 0.158 | 1.085E-11 | 0.310 | 1.126E-12 | 0.08 | 1.639E-11 |
| 0.264 | 6.460E-12 | 0.306 | 1.147E-12 | 0.12 | 1.434E-11 |
| 0.331 | 4.731E-12 | 0.305 | 1.176E-12 | 0.16 | 1.248E-11 |
| 0.53 | 1.679E-12 | 0.305 | 1.231E-12 | 0.2 | 1.078E-11 |
| 0.555 | 1.710E-12 | 0.298 | 1.37E-12 | 0.24 | 9.24E-12 |
| | | 0.301 | 1.723E-12 | 0.28 | 7.856E-12 |
| | | 0.296 | 2.072E-12 | 0.32 | 6.618E-12 |
| | | 0.291 | 2.414E-12 | 0.36 | 5.518E-12 |
| | | 0.281 | 2.658E-12 | 0.4 | 4.546E-12 |
| | | 0.272 | 3.043E-12 | 0.44 | 3.696E-12 |
| | | 0.234 | 3.839E-12 | 0.48 | 2.96E-12 |
| | | 0.219 | 4.673E-12 | 0.52 | 2.328E-12 |
| | | 0.204 | 5.528E-12 | 0.56 | 1.793E-12 |
| | | 0.187 | 6.402E-12 | 0.6 | 1.347E-12 |
| | | 0.174 | 7.133E-12 | 0.64 | 9.82E-13 |
| | | 0.156 | 7.834E-12 | 0.68 | 6.897E-13 |
| | | 0.140 | 8.531E-12 | 0.72 | 4.62E-13 |
| | | 0.127 | 9.207E-12 | 0.76 | 2.91E-13 |
| | | 0.108 | 9.931E-12 | 0.8 | 1.684E-13 |
| | | 0.092 | 1.073E-11 | 0.84 | 8.621E-14 |
| | | 0.092 | 1.159E-11 | 0.88 | 3.637E-14 |
| | | 0.077 | 1.226E-11 | 0.92 | 1.078E-14 |
| | | | | 0.96 | 1.347E-15 |
| | | | | 1 | 0 |

Table A.2 Experimental data for Fig. 2.7

| Gravimetric Analysis | | Neutron Imaging | | 3-order Exponential | |
|----------------------|-------------------|-----------------|-------------------|---------------------|-------------------|
| S | K, m ² | S | K, m ² | S | K, m ² |
| 0 | 8.097E-11 | 0.489 | 5.237E-12 | 0 | 8.097E-11 |
| 0.07 | 5.998E-11 | 0.456 | 5.42E-12 | 0.04 | 7.163E-11 |
| 0.195 | 4.928E-11 | 0.447 | 5.508E-12 | 0.08 | 6.305E-11 |
| 0.313 | 3.450E-11 | 0.472 | 5.617E-12 | 0.12 | 5.518E-11 |
| 0.379 | 2.398E-11 | 0.464 | 5.692E-12 | 0.16 | 4.799E-11 |
| 0.534 | 1.937E-11 | 0.455 | 5.711E-12 | 0.2 | 4.146E-11 |
| 0.674 | 1.103E-11 | 0.455 | 5.829E-12 | 0.24 | 3.554E-11 |
| | | 0.452 | 5.908E-12 | 0.28 | 3.022E-11 |
| | | 0.453 | 5.999E-12 | 0.32 | 2.546E-11 |
| | | 0.455 | 6.031E-12 | 0.36 | 2.123E-11 |
| | | 0.452 | 6.037E-12 | 0.4 | 1.749E-11 |
| | | 0.454 | 6.036E-12 | 0.44 | 1.422E-11 |
| | | 0.452 | 6.042E-12 | 0.48 | 1.138E-11 |
| | | 0.450 | 6.05E-12 | 0.52 | 8.954E-12 |
| | | 0.451 | 6.062E-12 | 0.56 | 6.897E-12 |
| | | 0.452 | 6.092E-12 | 0.6 | 5.182E-12 |
| | | 0.445 | 6.124E-12 | 0.64 | 3.778E-12 |
| | | 0.448 | 6.151E-12 | 0.68 | 2.653E-12 |
| | | 0.440 | 6.172E-12 | 0.72 | 1.777E-12 |
| | | 0.432 | 6.188E-12 | 0.76 | 1.119E-12 |
| | | 0.428 | 6.195E-12 | 0.8 | 6.477E-13 |
| | | 0.423 | 6.264E-12 | 0.84 | 3.316E-13 |
| | | 0.419 | 7.317E-12 | 0.88 | 1.399E-13 |
| | | 0.413 | 8.917E-12 | 0.92 | 4.146E-14 |
| | | 0.407 | 1.042E-11 | 0.96 | 5.182E-15 |
| | | 0.398 | 1.198E-11 | 1 | 0 |
| | | 0.387 | 1.38E-11 | | |
| | | 0.372 | 1.636E-11 | | |
| | | 0.358 | 1.84E-11 | | |
| | | 0.346 | 2.042E-11 | | |
| | | 0.339 | 2.197E-11 | | |
| | | 0.326 | 2.419E-11 | | |
| | | 0.314 | 2.613E-11 | | |

| | |
|-------|-----------|
| 0.299 | 2.842E-11 |
| 0.284 | 3.092E-11 |
| 0.267 | 3.321E-11 |
| 0.251 | 3.576E-11 |
| 0.236 | 3.802E-11 |
| 0.213 | 4.019E-11 |
| 0.203 | 4.228E-11 |
| 0.188 | 4.397E-11 |
| 0.173 | 4.582E-11 |
| 0.162 | 4.767E-11 |
| 0.151 | 4.952E-11 |
| 0.134 | 5.134E-11 |
| 0.119 | 5.333E-11 |
| 0.106 | 5.535E-11 |
| 0.091 | 5.734E-11 |
| 0.080 | 5.941E-11 |
| 0.065 | 6.163E-11 |

Table A.3 Experimental data for Fig. 2.9

| Neutron Imaging | | 3-order Exponential | |
|------------------------|-------------------|----------------------------|-------------------|
| S | K, m ² | S | K, m ² |
| 0.319 | 3.650E-12 | 0 | 0 |
| 0.375 | 3.865E-12 | 0.04 | 1.207E-15 |
| 0.379 | 3.870E-12 | 0.08 | 9.659E-15 |
| 0.447 | 5.688E-12 | 0.12 | 3.260E-14 |
| 0.447 | 5.585E-12 | 0.16 | 7.727E-14 |
| 1.000 | 1.887E-11 | 0.2 | 1.509E-13 |
| | | 0.24 | 2.608E-13 |
| | | 0.28 | 4.141E-13 |
| | | 0.32 | 6.182E-13 |
| | | 0.36 | 8.802E-13 |
| | | 0.4 | 1.207E-12 |
| | | 0.44 | 1.607E-12 |
| | | 0.48 | 2.086E-12 |
| | | 0.52 | 2.653E-12 |
| | | 0.56 | 3.313E-12 |
| | | 0.6 | 4.075E-12 |
| | | 0.64 | 4.945E-12 |
| | | 0.68 | 5.932E-12 |
| | | 0.72 | 7.041E-12 |
| | | 0.76 | 8.281E-12 |
| | | 0.8 | 9.659E-12 |
| | | 0.84 | 1.118E-11 |
| | | 0.88 | 1.286E-11 |
| | | 0.92 | 1.469E-11 |
| | | 0.96 | 1.669E-11 |
| | | 1 | 1.887E-11 |

Table A.4 Experimental data for Fig. 2.11

| Neutron Imaging | | 3-order Exponential | |
|------------------------|-------------------|----------------------------|-------------------|
| S | K, m ² | S | K, m ² |
| 0.583 | 3.022E-12 | 0 | 0 |
| 0.701 | 3.218E-12 | 0.04 | 8.725E-16 |
| 0.719 | 3.495E-12 | 0.08 | 6.98E-15 |
| 0.733 | 3.667E-12 | 0.12 | 2.356E-14 |
| 1.000 | 1.363E-11 | 0.16 | 5.584E-14 |
| | | 0.2 | 1.091E-13 |
| | | 0.24 | 1.885E-13 |
| | | 0.28 | 2.993E-13 |
| | | 0.32 | 4.467E-13 |
| | | 0.36 | 6.361E-13 |
| | | 0.4 | 8.725E-13 |
| | | 0.44 | 1.161E-12 |
| | | 0.48 | 1.508E-12 |
| | | 0.52 | 1.917E-12 |
| | | 0.56 | 2.394E-12 |
| | | 0.6 | 2.945E-12 |
| | | 0.64 | 3.574E-12 |
| | | 0.68 | 4.287E-12 |
| | | 0.72 | 5.088E-12 |
| | | 0.76 | 5.985E-12 |
| | | 0.8 | 6.98E-12 |
| | | 0.84 | 8.08E-12 |
| | | 0.88 | 9.29E-12 |
| | | 0.92 | 1.062E-11 |
| | | 0.96 | 1.206E-11 |
| | | 1 | 1.363E-11 |

| Table A.5 Experimental data for Fig. 3.4 | | | | | | | | | | |
|--------------------------------------------------------------------------------------------------------------------------------------------------|--------------|----------------|---------------|-----------------|-------------------|-------|-------------------|-------|---------------------|---------------|
| Current Density | Conventional | Interdigitated | Air Flow Rate | Total Flow Rate | k _{r,g} | s | k _{r,g} | s | Max dP in 1st 2 min | Last 2 min dP |
| (A/cm ²) | (V) | (V) | (ccm) | (ccm) | (m ²) | | (m ²) | | (Pa) | (Pa) |
| 0.148 | 0.746 | 0.749 | 15.79 | 22.82 | 8.495E-12 | 0.193 | 7.88E-12 | 0.211 | 1517.306 | 1408.239 |
| 0.296 | 0.691 | 0.718 | 31.59 | 45.64 | 8.105E-12 | 0.205 | 7.73E-12 | 0.216 | 3095.552 | 2952.125 |
| 0.444 | 0.656 | 0.686 | 47.38 | 68.46 | 8.971E-12 | 0.181 | 7.46E-12 | 0.225 | 4813.454 | 4000.881 |
| 0.592 | 0.609 | 0.674 | 63.17 | 91.29 | 9.328E-12 | 0.172 | 5.88E-12 | 0.286 | 8135.967 | 5130.168 |
| 0.740 | 0.587 | 0.662 | 78.96 | 114.11 | 8.705E-12 | 0.188 | 6.16E-12 | 0.274 | 9713.122 | 6871.289 |
| 0.888 | 0.553 | 0.638 | 94.76 | 136.93 | 9.756E-12 | 0.162 | 8.15E-12 | 0.203 | 8810.236 | 7357.799 |
| 1.036 | 0.525 | 0.604 | 110.55 | 159.75 | 8.503E-12 | 0.193 | 7.64E-12 | 0.219 | 10963.229 | 9849.042 |
| Electrode Area: 2.08*0.65=1.352 cm ² , k _{old} /k _{fuel cell} =1.849, the total flow rate includes the water vapor. | | | | | | | | | | |

| Table A.6 Experimental data for Fig. 3.6 | | | | | | | | | | |
|---------------------------------------------------------------------------------------------------------------------------------------------------|---------------------|-----------------------|---------------------------|-----------------------------|---------------------------------------|-------|----------------------------------------------------|-------|--------------------------------|--------------------------|
| Current Density (A/cm ²) | Conventional (V) | Interdigitated (V) | Air Flow Rate (ccm) | Total Flow Rate (ccm) | k _{r,g} (m ²) | s | k _{r,g} (peak dP) (m ²) | s | Max dP in 1st 2 min (Pa) | Last 2 min dP (Pa) |
| 0.148 | 0.687 | 0.709 | 15.791 | 22.819 | 4.954E-11 | 0.162 | 4.391E-11 | 0.205 | 1532.087 | 1358.009 |
| 0.296 | 0.580 | 0.636 | 31.582 | 45.638 | 4.513E-11 | 0.195 | 4.453E-11 | 0.199 | 3021.786 | 2981.221 |
| 0.444 | 0.536 | 0.603 | 47.372 | 68.457 | 4.554E-11 | 0.191 | 4.508E-11 | 0.195 | 4477.523 | 4431.570 |
| 0.592 | 0.492 | 0.574 | 63.163 | 91.276 | 4.676E-11 | 0.182 | 4.302E-11 | 0.212 | 6254.659 | 5755.272 |
| 0.740 | 0.450 | 0.551 | 78.954 | 114.095 | 4.817E-11 | 0.171 | 4.541E-11 | 0.192 | 7408.002 | 6982.655 |
| 0.888 | 0.433 | 0.533 | 94.745 | 136.914 | 4.782E-11 | 0.174 | 4.529E-11 | 0.193 | 8912.153 | 8442.103 |
| 1.036 | 0.386 | 0.503 | 110.535 | 159.733 | 5.006E-11 | 0.158 | 3.782E-11 | 0.260 | 12452.435 | 9407.384 |
| 1.183 | 0.325 | 0.461 | 126.326 | 182.552 | 4.924E-11 | 0.164 | 4.874E-11 | 0.167 | 11043.292 | 10929.790 |
| 1.331 | 0.184 | 0.438 | 142.117 | 205.371 | 5.113E-11 | 0.151 | 4.834E-11 | 0.170 | 12524.480 | 11841.440 |
| Electrode Area: 2.08*0.65=1.352 cm ² , k _{old} /k _{fuel cell} =14.734, the total flow rate includes the water vapor. | | | | | | | | | | |

| Table A.7 Experimental data for Fig. 3.8 | | | | | | | | | |
|--------------------------------------------------------------------------------------------------------------------------------------------------|------------------------------------|------------------------|--------------------------|---------------------------------------|-------|----------------------------------------------------|-------|------------------------------|------------------------|
| Current Density (A/cm ²) | Conventional Interdigitated (V) | Air Flow Rate (ccm) | Total Flow Rate (ccm) | k _{r,g} (m ²) | s | k _{r,g} (peak dP) (m ²) | s | Max dP in 1st 2 min Pa | Last 2 min dP Pa |
| 0.148 | 0.730 | 5.375 | 7.768 | 7.055E-12 | 0.239 | 3.498E-12 | 0.261 | 629.427 | 577.186 |
| 0.296 | 0.671 | 10.751 | 15.536 | 7.751E-12 | 0.216 | 3.793E-12 | 0.241 | 1161.144 | 1050.654 |
| 0.444 | 0.631 | 16.126 | 23.303 | 7.983E-12 | 0.208 | 3.772E-12 | 0.242 | 1751.455 | 1530.196 |
| 0.592 | 0.596 | 21.501 | 31.071 | 7.657E-12 | 0.219 | 4.097E-12 | 0.221 | 2149.644 | 2127.199 |
| 0.740 | 0.567 | 26.876 | 38.839 | 6.556E-12 | 0.258 | 1.661E-12 | 0.439 | 6629.192 | 3105.516 |
| 0.814 | 0.538 | 29.564 | 42.723 | 7.036E-12 | 0.240 | 3.662E-12 | 0.250 | 3306.905 | 3182.925 |
| 0.888 | 0.522 | 32.252 | 46.607 | 7.382E-12 | 0.228 | 3.882E-12 | 0.235 | 3403.039 | 3309.669 |
| 1.036 | 0.476 | 37.627 | 54.374 | 5.290E-12 | 0.313 | 2.757E-12 | 0.322 | 5590.735 | 5388.661 |
| Electrode Area: 2.08*0.65=1.352 cm ² , k _{old} /k _{fuel cell} =1.849, the total flow rate includes the water vapor. | | | | | | | | | |

Table A.8 Experimental data for Fig. 3.10

| Current Density (A/cm²) | Conventional (V) | Interdigitated (V) | Air Flow Rate (ccm) | Total Flow Rate (ccm) | k_{r,g} (m²) | s | k_{r,g} (peak dP) (m²) | s | Max dP in 1st 2 min Pa | Last 2 min dP Pa |
|--------------------------------------------------------------------------------------------------------------------------------------------------|-----------------------------------|-------------------------------------|--------------------------------------|----------------------------------------|--------------------------------------------------|----------|----------------------------------------------------------------------|----------|---------------------------------------------------|---------------------------------------------|
| 0.148 | 0.711 | 0.730 | 5.375 | 7.767 | 9.320E-12 | 0.172 | 7.588E-12 | 0.221 | 536.581 | 436.847 |
| 0.296 | 0.663 | 0.704 | 10.749 | 15.534 | 7.503E-12 | 0.224 | 7.048E-12 | 0.239 | 1155.289 | 1085.257 |
| 0.444 | 0.623 | 0.647 | 16.124 | 23.301 | 8.278E-12 | 0.200 | 7.578E-12 | 0.221 | 1611.793 | 1475.592 |
| 0.592 | 0.539 | 0.633 | 21.499 | 31.068 | 8.279E-12 | 0.200 | 8.275E-12 | 0.200 | 1968.001 | 1967.065 |
| 0.740 | 0.485 | 0.550 | 26.873 | 38.834 | 9.076E-12 | 0.178 | 8.735E-12 | 0.187 | 2330.454 | 2242.991 |
| 0.888 | 0.444 | 0.539 | 32.248 | 46.601 | 9.152E-12 | 0.176 | 8.737E-12 | 0.187 | 2796.171 | 2669.289 |
| 1.036 | 0.281 | 0.479 | 37.623 | 54.368 | 8.913E-12 | 0.182 | 8.904E-12 | 0.183 | 3200.910 | 3197.703 |
| Electrode Area: 2.08*0.65=1.352 cm ² , k _{old} /k _{fuel cell} =1.849, the total flow rate includes the water vapor. | | | | | | | | | | |